Weak Periodic Boundary Conditions: Effect on Principal Stress due to Axial Load under Varying Orientations

by

Erik Johannes Giesen Loo

to obtain the degree of Master of Science at the Delft University of Technology, to be defended publicly on Wednesday September 26, 2018 at 13:30.

Weak Periodic Boundary Conditions: Effect on Principal Stress due to Axial Load under Varying Orientations

by

Erik Johannes Giesen Loo

to obtain the degree of Master of Science at the Delft University of Technology, to be defended publicly on Wednesday September 26, 2018 at 13:30.

Student number:	4625064	
Project duration:	January 15, 2018 – September 4, 2018	
Thesis committee:	Dr. ir. F.P. van der Meer,	TU Delft, chair & mentor
	Prof. dr. ir. L.J. Sluys,	TU Delft, supervisor
	Dr. H. Hajibeygi,	TU Delft, supervisor

TU Delft

Abstract

Multiscale computational homogenization is an efficient method to upscale the microstructural behavior of micro-heterogeneous materials. In this method, a representative volume element (RVE) is assigned to a macroscale material point and the constitutive law for the macroscopic model at that point is obtained by solving a boundary value problem on the RVE. Among the conventional boundary conditions, the so-called strong periodic boundary conditions tend to converge faster towards the actual microstructural response. Nonetheless, applying strong periodic boundary conditions to a batch of 48 fiber-matrix RVEs under uniaxial load with varying orientations introduces a dependency between the average ultimate principal stress ($\bar{\sigma}_1$) and the orientation angle (θ).

This treatise investigates the effects on this dependency by applying so-called weak periodic boundary conditions instead. These boundary conditions soften the strong requirement of periodicity of displacements at the RVE boundary by coarsening the traction mesh and requiring periodicity to hold only in an average sense over this coarser mesh. Three main questions are asked: Do weak periodic boundary conditions alleviate the dependency between $\bar{\sigma}_1$ and θ? Is this dependency the result of RVEs prone to localization under shear? Do smaller coarsening factors widen the range of θ over which localization with a single shear band is permissible? Overall, it is concluded that only the weakest form of weak periodic boundary conditions reduces the dependency between $\bar{\sigma}_1$ and θ, which is indeed caused by RVEs that are prone to strain localization under shear, particularly towards $\theta = 45^o$. Increasing coarsening factors quickly introduce stricter periodicity requirements, thus limiting the possibility of strain localization with a single shear band at angles other than $\theta = 45^o$. Recommendations are provided to alleviate the dependency between $\bar{\sigma}_1$ and θ as well as how to more realistically model the behavior of RVEs used in this research.

Acknowledgements

I would like to acknowledge the following people:

Dr. ir. Frans van der Meer, for granting me the opportunity to work on such an interesting topic and for all his knowledge as well as the stability of structures course.

Prof.dr.ir. Bert Sluys, who supervised my research and whose finite element courses proved essential for the success of this treatise.

Dr. Hadi Hajibeygi, for supervising my research and constructive criticism.

My friends: Chanda Singoyi, Mustafa Abbas, Rahul Raj Dhakal and Samriddha Roy for indulging my rants.

Maximilian Edward Ororbia for sharing the burden of graduate life at Pennsylvania State University.

Tianqi, for her unwavering support and the good times amidst the struggles of the thesis life.

Finally, I would like to thank my friends in room 6.35 and my family, without whom none of this would have been possible.

Contents

List of Figures

List of Tables

Chapter 1

INTRODUCTION

1.1 Thesis Statement

The ultimate principal stress of equivalent representative volume elements due to axial load under varying orientations should, on average, remain constant. Notwithstanding, prescribing periodic boundary conditions introduces a dependency between the ultimate principal stress and the orientation angle. This dependency may be reduced by prescribing weak periodic boundary conditions.

1.2 Multiscale Computational Homogenization

The macroscale behavior of multiphase materials generally depends on the response of its underlying heterogeneous microstructure (Karamnejad, 2016, p. 1, Kouznetsova, Geers, and Brekelmans, 2010, p. 2). Modeling these heterogeneities directly at the macroscale may give accurate results but often requires enormous computational efforts (Karamnejad, 2016, p. 1). Instead, multiscale methods can be used to account for the underlying micro-heterogeneity in an approximate fashion (Kouznetsova et al., 2010, p. 4). This is achieved via so-called homogenization methods, which supplant the heterogeneous material at the subscale by an equivalent homogeneous material (Sluys, 2017, p. 12). Among these methods, computational homogenization is probably one of the most accurate techniques to upscale the nonlinear behavior of heterogeneous microstructures (Geers, Kouznetsova, and Brekelmans, 2010, p. 2175, Öhman, Runesson, and Larsson, 2015, p. 1). In this method, a representative volume element (RVE) is assigned to a macroscale material point and the constitutive law for the macroscopic model at that point is obtained by solving a boundary value problem (BVP) on the RVE (Karamnejad, 2016).

Computational homogenization can be applied to materials whose subscale properties are nonlinear, whereby it is necessary to solve a fully nested macroscale-subscale BVP. This is referred to as multiscale computational homogenization or FE^2 (Kouznetsova et al., 2010, p. 4, Öhman et al., 2015, p. 1). The basic

steps for multiscale computational homogenization are:

1. defining an appropriate size for each RVE,
2. formulating subscale boundary conditions, and
3. homogenizing the solution to the subscale BVP.

The first step requires choosing an appropriate scale (size). In general, an RVE should be small enough to satisfy the principle of separation of scales[1] but large enough to accurately represent the microstructure and its phenomena (Geers et al., 2010, Coenen, Kouznetsova, and Geers, 2012). Typical subscales comprise the mesoscale ($\sim 10^{-3}$m) and microscale ($\sim 10^{-6}$m); however, selecting appropriate RVE sizes falls beyond the scope of this treatise.

The second step entails transferring the macroscale deformation gradient onto the RVE via boundary conditions in exchange for a homogenized stress and tangent stiffness operator in the third step (Geers et al., 2010). Three classical options exist for defining boundary conditions (see Table 2.2). Among these, periodic boundary conditions converge faster (with increasing RVE size) towards the actual microstructural response (Svenning, Fagerström, and Larsson, 2017).

1.3 Study on Periodic Boundary Conditions

Although periodic boundary conditions are typically confined to deformation-driven procedures, the principal stress necessary to substantiate the thesis statement should ideally be derived by prescribing a uniaxial stress on the RVE.[2] Fortunately, strong periodic boundary conditions support the application of external forces on the RVE corners to represent stress (van der Meer, 2016). In unpublished work by Van der Meer, uniaxial stress was applied to a sample of 48 different fiber-matrix composite RVEs at 46 different angles between 0^o and 90^o with respect to the orientation of the RVE boundaries. The ultimate applied stress in simulations with elasto-plastic matrix was recorded to generate the ultimate principal stress (σ_1) vs. orientation angle (θ) curves in Fig. 1.1.

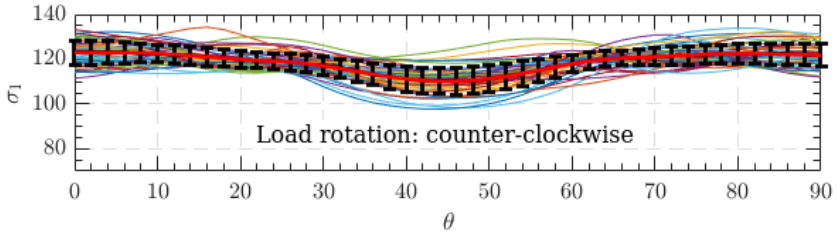

Figure 1.1: Ultimate principal stress vs. orientation angle, strong periodic boundary conditions

[1] The macroscale deformation gradient should essentially be constant over each RVE

[2] The correct uniaxial strain requires prior knowledge of the strain in the perpendicular direction, which is not readily available with nonlinear heterogeneous materials.

This experiment was performed for both a clockwise and counterclockwise rotation of the load, resulting in different individual σ_1–θ curves but the same curve of average ultimate principal stress ($\bar{\sigma}_1$) vs. θ. This ratifies the existence of a dependency between $\bar{\sigma}_1$ and θ. Hereinafter, it is demonstrated that this dependency is not derived from having a small sample size, but rather the result of choosing RVEs that are prone to strain localization under shear. The effect of the localized shear bands on σ_1 is discussed in detail in Chapter 6.

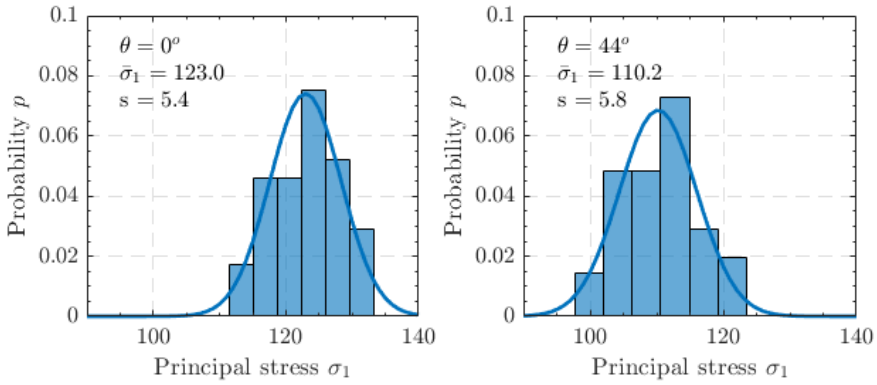

Figure 1.2: Histograms of the ultimate principal stresses

Null hypothesis significance testing is used to verify whether or not the RVEs tend to have – on average – a lower σ_1 when oriented at 44^o.[3] Let $\bar{Y}_1$ and $\bar{Y}_2$ be random variables representing $\bar{\sigma}_1$ at $\theta = 0^o$ and $\theta = 44^o$, respectively. Fig. 1.2 confirms that both variables can be well approximated by normal distributions:

$$\bar{Y}_1 \sim \mathrm{N}(\mu_1, \sigma_1^2/n_1),$$
$$\bar{Y}_2 \sim \mathrm{N}(\mu_2, \sigma_2^2/n_2).$$

Here, μ_i and σ_i are unknown population means and standard deviations and n_i is the sample size. The goal is to test whether changing θ from 0^o to 44^o altered the population mean. That is, do $\bar{Y}_1$ and $\bar{Y}_2$ stem from the same population? Can the difference in the sample means be attributed to the randomness of the sample? These two questions are rephrased as the null and alternate hypothesis:

$$\mathbf{H_0} : \mu_1 = \mu_2,$$
$$\mathbf{H_1} : \mu_1 \neq \mu_2.$$

The assumption of normality of $\bar{Y}_1$ and $\bar{Y}_2$ sanctions the use of Welch's t-test to verify $\mathbf{H}_0$ (Dekking, Kraaikamp, Lopuhaä, and Meester, 2005, p. 400). Using this test, $\mathbf{H}_0$ is rejected in favor of $\mathbf{H}_1$ at the $\alpha = 0.05$ significance level with a p-value of $7.9 \cdot 10^{-17}$. That is, the dependency between the $\bar{\sigma}_1$ and θ is most likely not random. The statistical calculations are presented in Appendix A.

[3] The orientation angle was varied by 2^o each time. Data is only available for 44^o and 46^o.

1.4 Research Purpose

As an alternative to strong periodic boundary conditions, Larsson, Runesson, Saroukhani, and Vafadari (2011) developed weak periodic boundary conditions, with offer more flexibility regarding the deformation of the RVE boundary. The objective of this treatise is to demonstrate whether enforcing weak periodic boundary conditions instead of strong periodic boundary conditions does ameliorate the dependency between $\bar{\sigma}_1$ and θ.

First, the formulation of the weak periodic boundary conditions in (Larsson et al., 2011) is extended to allow corner forces that represent macroscopic stress tensors (section 3.1). This extended model is implemented using the Jem and Jive C++ libraries (Dynaflow Research Group, n.d.) in Section 3.2. The model is validated via linear-elastic and materially-nonlinear examples in Chapter 4. The thesis statement is then tested per the methodology in Chapter 5. Finally, Chapter 6 discusses the results and the effects of localized shear bands on $\bar{\sigma}_1$.

1.5 Notation

Tensors and tensor products are used throughout this treatise. Scalars and scalar functions are denoted by lower-case italic letters such as a, b and n. Vectors, except for σ and ε, are denoted by lower-case bold letters such as $\mathbf{n}$. Matrices are denoted by upper-case bold letters such as $\mathbf{A}$, $\mathbf{B}$ and $\mathbf{\Sigma}$. The inner (dot) product (including matrix multiplication) is defined as the contraction over the last index of the first tensor and the first index of the last tensor, or

$$\mathbf{a} \cdot \mathbf{b} = \sum_i a_i b_i, \tag{1.1}$$

$$\mathbf{A} \cdot \mathbf{b} = \sum_j a_{ij} b_j, \tag{1.2}$$

$$\mathbf{AB} = \sum_j a_{ij} b_{jk}. \tag{1.3}$$

For brevity, the dot is omitted when the product occurs between two matrices. The double dot product is defined as the contraction over the two closest indices:

$$\mathbf{A} : \mathbf{B} = \sum_i \sum_j a_{ij} b_{ji}. \tag{1.4}$$

Finally, the outer product (also referred to as the dyadic product) is defined as

$$\mathbf{a} \otimes \mathbf{b} = a_i b_j. \tag{1.5}$$

All numerical examples in this treatise can be reproduced using a consistent set of units.[4] Herein, forces are implicitly given in Newtons and distances in mm.

[4] That is, derived units use the the units of their base units. E.g. stress is given in $\mathrm{N/mm^2}$.

Chapter 2

BACKGROUND

Materially nonlinear finite element analyses are characterized by changing tangent operators ($\mathbf{D}_t$) due to microstructural phenomena such as steel yielding and concrete cracking. $\mathbf{D}_t$ is evaluated numerically at so-called integration points (IP) either via macroscopic modeling or multiscale modeling (Runesson and Larsson, 2011; Sandström, Larsson, and Runesson, 2014, p. 2).

Table 2.1: FEM constitutive modeling. From (Runesson and Larsson, 2011)

Macroscopic modeling	**Multiscale modeling**
Microstructure response modeled implicitly via internal variables	Microstructure modeled explicitly using representative volume elements
Calibration from macroscale experiments or subscale modeling	Calibration from macroscale experiments or further subscale modeling

In macroscopic modeling, the effect of the microstructural behavior on $\mathbf{D}_t$ is represented implicitly via internal variables (Runesson and Larsson, 2011). In multiscale modeling, $\mathbf{D}_t$ is determined by upscaling the response of the deforming microstructure via computational homogenization (Kouznetsova et al., 2010, pp. 1-4; Sandström et al., 2014, p. 2). The microstructure around each IP is modeled explicitly using RVEs and a local BVP is solved on each RVE (Larsson et al., 2011, p. 12; Sandström et al., 2014, p. 2). The macroscale deformation gradient ($\mathbf{u} \otimes \nabla$) at each IP of the macroscale BVP is used to formulate boundary conditions on its corresponding RVE (Kouznetsova et al., 2010, p. 7; Geers et al., 2010, p. 2176; Coenen et al., 2012, p. 2). After solving the subscale BVP, standard averaging equations yield the macroscopic stress tensor ($\bar{\boldsymbol{\Sigma}}$) and a static condensation process yields $\mathbf{D}_t$ (Geers et al., 2010, p. 2176). This process is illustrated in Fig. 2.1.

Common boundary conditions include prescribed displacements (Dirichlet), prescribed boundary tractions (Neumann) and prescribed periodicity (strong periodic) (Larsson et al., 2011, p. 11; Coenen et al., 2012, p. 2). Dirichlet boundary conditions impose boundary displacements which conform strictly to $\mathbf{u} \otimes \nabla$,

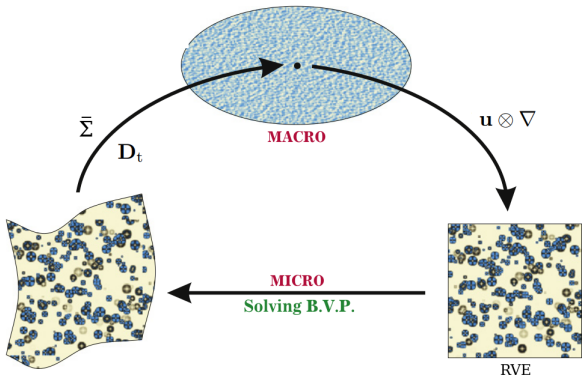

Figure 2.1: Computational homogenization. From (Geers, Kouznetsova, and Brekelmans, 2010, p. 2176)

resulting in an overstiff prediction of $\mathbf{D}_t$. Conversely, Neumann boundary conditions prescribe minimal kinematic boundary conditions, thus underestimating $\mathbf{D}_t$ (Coenen et al., 2012, p. 2). Strong periodic boundary conditions have shown to provide a better estimate of the stiffness for both periodic and random microstructures (Larsson et al., 2011, p. 11; Coenen et al., 2012, p. 2). Regardless, both Dirichlet and strong periodic boundary conditions constrain (to varying degrees) the strain percolation path (strain localization) at the boundary (Coenen et al., 2012, p. 2). Table 2.2 summarizes the classical boundary conditions for the subscale BVP.

Table 2.2: Classical boundary conditions. From (Coenen, Kouznetsova, and Geers, 2012, p. 4)

BC type	**Effective stiffness**	**Strain percolation path**
Dirichlet	Overestimation	Constrained at boundary
Strong periodic	Good estimate	Only those respecting periodicity
Neumann	Underestimation	Sensitive to spurious localization

As an alternative, the weak periodic boundary conditions developed by (Larsson et al., 2011) prescribe periodicity in a weak sense, thereby allowing some non-periodic localization and improving the effective stiffness estimate (Sandström et al., 2014, Svenning, Fagerström, and Larsson, 2016). Section 2.1 formulates the macroscopic problem and coupling of scales. Section 2.2 presents the subscale boundary value problem and the boundary conditions. Finally, Section 2.3 elaborates the Galerkin approximations for the FEM implementation.

2.1 Macroscale Boundary Value Problem

2.1.1 Quasistatic Stress Problem

The macroscale problem is described by point-wise equilibrium on the domain Ω, and corresponding Dirichlet and Neumann boundary conditions on $\partial\Omega \equiv \Gamma$:

$$-\boldsymbol{\Sigma} \cdot \nabla = \mathbf{f} \text{ in } \Omega, \tag{2.1}$$

$$\mathbf{u} = \mathbf{u}_\mathrm{p} \text{ on } \Gamma_\mathrm{D}, \tag{2.2}$$

$$\mathbf{t} \triangleq \boldsymbol{\Sigma} \cdot \hat{\mathbf{n}} = \mathbf{t}_\mathrm{p} \text{ on } \Gamma_\mathrm{N}. \tag{2.3}$$

$\boldsymbol{\Sigma}$ is the first Piola-Kirchhoff stress (i.e. the transpose of the nominal stress), ∇ is the spatial gradient with respect to coordinates $\mathbf{x}$ in the reference configuration, $\mathbf{f}$ is the vector of body forces (e.g., due to gravity) and $\hat{\mathbf{n}}$ is a normal unit vector describing Γ_N. The weak form of (2.1) is given by: Find $\mathbf{u} \in \mathbb{U}(\mathbf{u}_\mathrm{p})$ that solves

$$\begin{aligned} \int_\Omega \boldsymbol{\Sigma} : [\delta\mathbf{u} \otimes \nabla] \,\mathrm{d}\,\Omega = \int_\Omega \mathbf{f} \cdot \delta\mathbf{u} \,\mathrm{d}\,\Omega + \int_{\Gamma_\mathrm{N}} \mathbf{t}_\mathrm{p} \cdot \delta\mathbf{u} \,\mathrm{d}\,\Gamma, \; \forall \delta\mathbf{u} \in \mathbb{U}(\mathbf{0}), \\ \mathbb{U}(\mathbf{u}_\mathrm{p}) = \{\mathbf{u} \in [\mathbb{H}(\Omega)]^\mathrm{d}, \mathbf{u} = \mathbf{u}_\mathrm{p} \text{ on } \Gamma_\mathrm{D}\}. \end{aligned} \tag{2.4}$$

2.1.2 Macroscale-Subscale Transision

Separation of scales is now introduced. The local field around each IP is replaced by a homogenized RVE occupying the subscale region $\Omega_\square$ with boundary $\Gamma_\square$ (Larsson et al., 2011, p. 12). The scales are coupled via the following averaging expressions (Larsson et al., 2011, p. 12; Kouznetsova et al., 2010, p. 12):

$$\begin{aligned} \langle y \rangle_\square &\triangleq \frac{1}{|\Omega_\square|} \int_{\Omega_\square} y \,\mathrm{d}\,\Omega, \\ \langle\langle y \rangle\rangle_\square &\triangleq \frac{1}{|\Gamma_\square|} \int_{\Gamma_\square} y \,\mathrm{d}\,\Gamma. \end{aligned} \tag{2.5}$$

The integrands in (2.4) are homogenized at each RVE using (2.5), such that

$$\int_\Omega \langle \boldsymbol{\Sigma} : [\delta\mathbf{u} \otimes \nabla] \rangle_\square \,\mathrm{d}\,\Omega = \int_\Omega \langle \mathbf{f} \cdot \delta\mathbf{u} \rangle_\square \,\mathrm{d}\,\Omega + \int_{\Gamma_\mathrm{N}} \langle\langle \mathbf{t}_\mathrm{p} \cdot \delta\mathbf{u} \rangle\rangle_\square \,\mathrm{d}\,\Gamma. \tag{2.6}$$

The displacement field inside each RVE is given by (Larsson et al., 2011, p. 12):

$$\mathbf{u} = \mathbf{u}_\mathrm{M} + \mathbf{u}_\mathrm{s}, \tag{2.7}$$

where $\mathbf{u}_\mathrm{M}$ is the macroscale component and $\mathbf{u}_\mathrm{s}$ is the subscale fluctuation. First-order homogenization implies a linear variation of $\mathbf{u}_\mathrm{M}$ within each RVE:

$$\mathbf{u}_\mathrm{M} = \bar{\mathbf{u}} + (\bar{\mathbf{u}} \otimes \nabla) \cdot (\mathbf{x} - \bar{\mathbf{x}}). \tag{2.8}$$

The vector $\bar{\mathbf{u}} \triangleq \langle \mathbf{u} \rangle_\square$ is equivalent to the macroscale displacement at $\bar{\mathbf{x}} \triangleq \langle \mathbf{x} \rangle_\square$.[1] Assume $\mathbf{t}_\mathrm{p}$ and $\mathbf{f}$ are smooth enough over the RVE domain to be replaced by

[1] Each RVE is conveniently centered around its IP. That is, $\bar{\mathbf{x}}$ coincides with the IP location.

$\bar{\mathbf{t}}_{\mathrm{p}} \triangleq \langle\langle \mathbf{t}_{\mathrm{p}} \rangle\rangle_{\square}$ and $\bar{\mathbf{f}} \triangleq \langle \mathbf{f} \rangle_{\square}$.[2] Per the Hill-Mandel macro-homogeneity condition (Kouznetsova et al., 2010, p. 14), (2.6) is recast as: Find $\bar{\mathbf{u}} \in \bar{\mathbb{U}}(\bar{\mathbf{u}}_{\mathrm{p}})$ that solves

$$\begin{aligned} \int_{\Omega} \bar{\boldsymbol{\Sigma}} : [\delta\bar{\mathbf{u}} \otimes \nabla] \,\mathrm{d}\,\Omega = \int_{\Omega} \bar{\mathbf{f}} \cdot \delta\bar{\mathbf{u}} \,\mathrm{d}\,\Omega + \int_{\Gamma_{\mathrm{N}}} \bar{\mathbf{t}}_{\mathrm{p}} \cdot \delta\bar{\mathbf{u}} \,\mathrm{d}\,\Gamma, \; \forall \delta\bar{\mathbf{u}} \in \bar{\mathbb{U}}(\mathbf{0}), \\ \bar{\mathbb{U}}(\bar{\mathbf{u}}_{\mathrm{p}}) = \{\mathbf{u} \in [\mathbb{H}^1(\Omega)]^d, \mathbf{u} = \bar{\mathbf{u}}_{\mathrm{p}} \text{ on } \Gamma_{\mathrm{D}}\}, \end{aligned} \tag{2.9}$$

with the homogenized stress tensor expressed as $\bar{\boldsymbol{\Sigma}} \triangleq \langle \boldsymbol{\Sigma} \rangle_{\square}$ and $\bar{\mathbf{u}}_{\mathrm{p}} \triangleq \langle \mathbf{u}_{\mathrm{p}} \rangle_{\square}$. The reader is referred to (Kouznetsova et al., 2010) for a thorough explanation of multiscale homogenization and the coupling of scales.

2.2 Subscale Boundary Value Problem

2.2.1 Canonical Format of the RVE Problem

The subscale problem is also described by point-wise equilibrium, c.f. (2.1). However, both $\mathbf{u}$ and $\mathbf{t}$ are a priori unknowns (Larsson et al., 2011, p. 14). Ergo, the BVP on each RVE is stated as follows: Find $\mathbf{u}$ and $\mathbf{t}$ that solves

$$\int_{\Omega_{\square}} \boldsymbol{\Sigma} : [\delta\mathbf{u} \otimes \nabla] \,\mathrm{d}\,\Omega = \int_{\Omega_{\square}} \mathbf{f} \cdot \delta\mathbf{u} \,\mathrm{d}\,\Omega + \int_{\Gamma_{\square}} \mathbf{t} \cdot \delta\mathbf{u} \,\mathrm{d}\,\Gamma. \tag{2.10}$$

Recognizing that rigid-body-motion does not alter the stress resultant from the subscale BVP, the displacement is split into a constant and a varying component:

$$\mathbf{u} = \bar{\mathbf{u}} + \mathbf{u}' \text{ with } \bar{\mathbf{u}} \in \mathbb{R}^3, \, \mathbf{u}' \in \mathbb{U}_{\square} = \{\mathbf{u} \in [\mathbb{H}^1(\Omega_{\square})]^d, \, \mathbf{u}(\bar{\mathbf{x}}) = 0\}. \tag{2.11}$$

Equation (2.10) is not solvable without removing $\bar{\mathbf{u}}$ (Larsson et al., 2011, p. 14). Note that $\mathbf{u}' = (\bar{\mathbf{u}} \otimes \nabla) \cdot (\mathbf{x} - \bar{\mathbf{x}}) + \mathbf{u}_{\mathrm{s}}$. Setting $\mathbf{u}'(\bar{\mathbf{x}}) = 0$ implies $\mathbf{u}_{\mathrm{s}}(\bar{\mathbf{x}}) = 0$, which conveniently yields $\mathbf{u}(\bar{\mathbf{x}}) = \mathbf{u}_{\mathrm{M}}(\bar{\mathbf{x}}) = \bar{\mathbf{u}}$. The traction is similarly split:

$$\mathbf{t} = \bar{\mathbf{t}} + \mathbf{t}' \text{ with } \bar{\mathbf{t}} \in \mathbb{R}^3, \, \mathbf{t}' \in \mathbb{T}_{\square} = \{\mathbf{t} \in [\mathbb{L}_2(\Gamma_{\square})]^{d-1}, \; \langle\langle \mathbf{t} \rangle\rangle_{\square} = 0\}. \tag{2.12}$$

The $\langle\langle \mathbf{t} \rangle\rangle_{\square} = 0$ requirement implies self-equilibrating traction forces (Larsson et al., 2011, p. 14). Substituting $\mathbf{u} = \bar{\mathbf{u}} + \mathbf{u}'$ into (2.10) yields (2.13)[3] and (2.14):

$$\int_{\Omega_{\square}} \mathbf{f} \,\mathrm{d}\,\Omega \cdot \delta\bar{\mathbf{u}} + \int_{\Gamma_{\square}} \mathbf{t} \,\mathrm{d}\,\Gamma \cdot \delta\bar{\mathbf{u}} = 0, \tag{2.13}$$

$$\int_{\Omega_{\square}} \boldsymbol{\Sigma} : [\delta\mathbf{u}' \otimes \nabla] \,\mathrm{d}\,\Omega = \int_{\Omega_{\square}} \mathbf{f} \cdot \delta\mathbf{u}' \,\mathrm{d}\,\Omega + \int_{\Gamma_{\square}} \mathbf{t} \cdot \delta\mathbf{u}' \,\mathrm{d}\,\Gamma. \tag{2.14}$$

Expressing (2.13) as $\langle \mathbf{f} \rangle_{\square} \cdot \delta\bar{\mathbf{u}} + |\Gamma_{\square}| \,/\, |\Omega_{\square}| \, \langle\langle \mathbf{t} \rangle\rangle_{\square} \cdot \delta\bar{\mathbf{u}} = 0$ yields

$$\bar{\mathbf{t}} \triangleq \langle\langle \mathbf{t} \rangle\rangle_{\square} = -\frac{|\Omega_{\square}|}{|\Gamma_{\square}|} \langle \mathbf{f} \rangle_{\square} \,. \tag{2.15}$$

[2] This holds true if we restrict to the situation when $|\Omega_{\square}| \to 0$ and $|\Gamma_{\square}| \to 0$.

[3] The strain energy term vanishes because $\delta\bar{\mathbf{u}} \otimes \nabla = 0$.

Substituting $\mathbf{t} = \bar{\mathbf{t}} + \mathbf{t}'$, with $\bar{\mathbf{t}}$ defined in (2.15), into (2.14) yields

$$\int_{\Omega_\square} \boldsymbol{\Sigma} : [\delta\mathbf{u}' \otimes \nabla] \, \mathrm{d}\,\Omega = \int_{\Omega_\square} \mathbf{f} \cdot \delta\mathbf{u}' \, \mathrm{d}\,\Omega + \int_{\Gamma_\square} \mathbf{t}' \cdot \delta\mathbf{u}' \, \mathrm{d}\,\Gamma + \bar{\mathbf{t}} \cdot \int_{\Gamma_\square} \delta\mathbf{u}' \, \mathrm{d}\,\Gamma. \quad (2.16)$$

Similarly, $\mathbf{t} = \bar{\mathbf{t}} + \mathbf{t}'$ is substituted into (2.13) to derive the following expression:

$$\int_{\Omega_\square} \mathbf{f} \cdot \delta\mathbf{a} \, \mathrm{d}\,\Omega + \bar{\mathbf{t}} \cdot \int_{\Gamma_\square} \delta\mathbf{a} \, \mathrm{d}\,\Gamma = 0, \, \forall \delta\mathbf{a} \in \mathbb{R}^3. \quad (2.17)$$

By this token, (2.16) simplifies to: Find $\mathbf{u}' \in \mathbb{U}_\square$ and $\mathbf{t}' \in \mathbb{T}_\square$ that solves

$$\int_{\Omega_\square} \boldsymbol{\Sigma} : [\delta\mathbf{u}' \otimes \nabla] \, \mathrm{d}\,\Omega = \int_{\Gamma_\square} \mathbf{t}' \cdot \delta\mathbf{u}' \, \mathrm{d}\,\Gamma, \, \forall \delta\mathbf{u}' \in \mathbb{U}_\square. \quad (2.18)$$

2.2.2 Classical Boundary Conditions

Solving (2.18) requires the introduction of boundary conditions which respect the Hill-Mandel condition and the averaging assumptions used to derive (2.9). The boundary conditions introduced in Table 2.2 do indeed satisfy these conditions (see Kouznetsova et al., 2010, pp. 12-15).

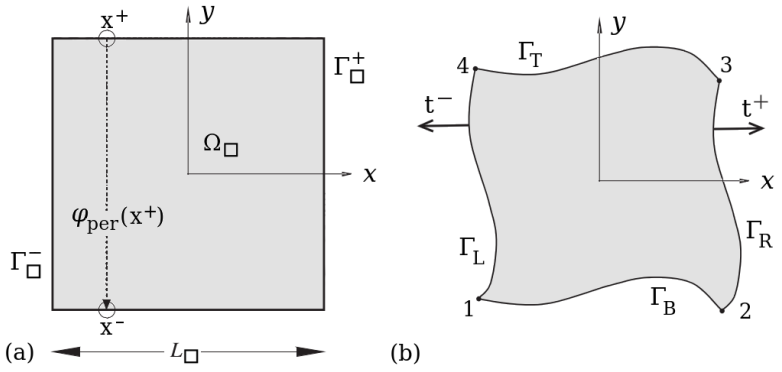

Figure 2.2: RVE: (a) undeformed; (b) periodic displacements

The Dirichlet boundary conditions impose displacements on the boundary of the RVE which conform strictly to the macroscopic displacement gradient:

$$\mathbf{u}' = (\bar{\mathbf{u}} \otimes \nabla) \cdot (\mathbf{x} - \bar{\mathbf{x}}), \, \forall \mathbf{x} \text{ on } \Gamma_\square. \quad (2.19)$$

The fluctuation term is not allowed to exist on the boundary: $\mathbf{u}_\mathrm{s} = \mathbf{0}$ on $\Gamma_\square$. In order to formulate strong periodic boundary conditions, $\Gamma_\square$ is split into an image boundary ($\Gamma^+_\square$) and a mirror boundary ($\Gamma^-_\square$), such that $\Gamma_\square = \Gamma^+_\square \cup \Gamma^-_\square$ (see Fig. 2.2). The mapping $\varphi_\mathrm{per} : \Gamma^+_\square \to \Gamma^-_\square$ mirrors any $\mathbf{x}^+ \in \Gamma^+_\square$ onto $\mathbf{x}^- \in \Gamma^-_\square$.

That is, $\mathbf{x}^- = \varphi_{\text{per}}(\mathbf{x}^+)$. Strong periodicity postulates a simultaneous variation of $\mathbf{u}'$ and $\mathbf{t}'$ which allows $\mathbf{u}_\text{s}$ to exist on $\Gamma_\square$ (Kouznetsova et al., 2010, p. 11):

$$[\![\mathbf{u}']\!]_\square = (\bar{\mathbf{u}} \otimes \nabla) \cdot [\![\mathbf{x} - \bar{\mathbf{x}}]\!]_\square, \, \forall \mathbf{x} \text{ on } \Gamma_\square^+, \tag{2.20}$$

$$\mathbf{t}'(\mathbf{x}) = -\mathbf{t}'(\varphi_{\text{per}}(\mathbf{x})), \, \forall \mathbf{x} \text{ on } \Gamma_\square^+, \tag{2.21}$$

where $[\![\mathbf{u}']\!]_\square \triangleq \mathbf{u}'(\mathbf{x}) - \mathbf{u}'(\varphi_{\text{per}}(\mathbf{x}))$. Equation (2.19) implies $[\![\mathbf{u}_\text{s}]\!]_\square = \mathbf{0}$ on $\Gamma_\square^+$. The macroscopic component, $(\bar{\mathbf{u}} \otimes \nabla) \cdot (\mathbf{x} - \bar{\mathbf{x}})$, is prescribed on $\Gamma_\square$ in an average sense due to the strong periodicity requirement of $\mathbf{u}_\text{s}$ on $\Gamma_\square$. Lastly, Neumann boundary conditions enforce constant tractions on the RVE boundary given by

$$\mathbf{t}' = \bar{\boldsymbol{\Sigma}} \cdot \hat{\mathbf{n}} \text{ on } \Gamma_\square. \tag{2.22}$$

Note that condition (2.22) is, in and of itself, insufficient to define and solve the BVP, as is shown in Section 2.3.4.

2.2.3 Weak Periodic Boundary Conditions

Essentially, weak periodic boundary conditions present a variational (weak) form of the periodicity constraint in (2.20) (Larsson et al., 2011, p. 15):

$$\int_{\Gamma_\square^+} \delta\mathbf{t}' \cdot [\![\mathbf{u}_\text{s}]\!]_\square \, \mathrm{d}\,\Gamma = 0, \, \forall \delta\mathbf{t}' \in \mathbb{T}_\square^+, \tag{2.23}$$

where $\mathbb{T}_\square^+$ is the trace of functions in $\mathbb{T}_\square$ on the image boundary $\Gamma_\square^+$.[4] Thence, all trial and test functions reside on $\Gamma_\square^+$. Using criterion (2.21), it follows that

$$\begin{aligned} \int_{\Gamma_\square} \mathbf{t}' \cdot \delta\mathbf{u}' \, \mathrm{d}\,\Gamma = \int_{\Gamma_\square^+} \mathbf{t}' \cdot \delta\mathbf{u}' \, \mathrm{d}\,\Gamma + \int_{\Gamma_\square^+} \mathbf{t}'(\varphi_{\text{per}}(\mathbf{x})) \cdot \delta\mathbf{u}'(\varphi_{\text{per}}(\mathbf{x})) \, \mathrm{d}\,\Gamma = \\ \int_{\Gamma_\square^+} \mathbf{t}' \cdot (\delta\mathbf{u}' - \delta\mathbf{u}'(\varphi_{\text{per}}(\mathbf{x}))) \, \mathrm{d}\,\Gamma = \int_{\Gamma_\square^+} \mathbf{t}' \cdot [\![\delta\mathbf{u}']\!]_\square \, \mathrm{d}\,\Gamma. \end{aligned} \tag{2.24}$$

Using (2.24), equation (2.18) is reformulated for weak micro-periodicity as: Find $\mathbf{u}' \in \mathbb{U}_\square$ and $\mathbf{t}' \in \mathbb{T}_\square$ for a given macroscopic strain $(\bar{\mathbf{u}} \otimes \nabla)$ that solves

$$\begin{aligned} \int_{\Omega_\square} \boldsymbol{\Sigma} : [\delta\mathbf{u}' \otimes \nabla] \, \mathrm{d}\,\Omega - \int_{\Gamma_\square^+} \mathbf{t}' \cdot [\![\delta\mathbf{u}']\!]_\square \, \mathrm{d}\,\Gamma = 0, \, \forall \delta\mathbf{u}' \in \mathbb{U}_\square, \\ - \int_{\Gamma_\square^+} \delta\mathbf{t}' \cdot [\![\mathbf{u}']\!]_\square \, \mathrm{d}\,\Gamma = - \int_{\Gamma_\square^+} \delta\mathbf{t}' \cdot (\bar{\mathbf{u}} \otimes \nabla) \cdot [\![\mathbf{x} - \bar{\mathbf{x}}]\!]_\square \, \mathrm{d}\,\Gamma, \, \forall \delta\mathbf{t}' \in \mathbb{T}_\square. \end{aligned} \tag{2.25}$$

Notice that $(2.25)_\text{b}$ is a reformulation of (2.23). Hereinafter, the following change in notation is adopted for the sake of brevity: $\mathbf{u}' \to \mathbf{u}$ and $\mathbf{t}' \to \mathbf{t}$.

[4] Hereinafter, $\mathbb{T}_\square^+$ is simply referred to as $\mathbb{T}_\square$.

2.3 Galerkin Approximations

Weak periodic boundary conditions serve as a transition between the strong periodic and Neumann boundary conditions. As shown next, Dirichlet and strong periodic boundary conditions possess the finest traction meshes ($\mathcal{T}^{\mathrm{h}}$) and most restricted displacement fields ($\mathbb{U}^{\mathrm{h}}$) whereas Neumann boundary conditions possess the coarsest $\mathcal{T}^{\mathrm{h}}$ and least restricted $\mathbb{U}^{\mathrm{h}}$ (Svenning et al., 2016, p. 6).

2.3.1 Weak Periodic Boundary Conditions

The Galerkin approximation for the BVP with weak micro-periodicity follows: Find $\mathbf{u}^{\mathrm{h}} \in \mathbb{U}^{\mathrm{h}}_{\square} \subset \mathbb{U}_{\square}$ and $\mathbf{t}^{\mathrm{h}} \in \mathbb{T}^{\mathrm{h}}_{\square} \subset \mathbb{T}_{\square}$ for a given strain $\bar{\mathbf{u}} \otimes \nabla$ that solves

$$\begin{aligned} \int_{\Omega_{\square}} \boldsymbol{\Sigma} : [\delta\mathbf{u}^{\mathrm{h}} \otimes \nabla] \,\mathrm{d}\,\Omega - \int_{\Gamma^{+}_{\square}} \mathbf{t}^{\mathrm{h}} \cdot [\![\delta\mathbf{u}^{\mathrm{h}}]\!]_{\square} \,\mathrm{d}\,\Gamma = 0, \; \forall \delta\mathbf{u}^{\mathrm{h}} \in \mathbb{U}^{\mathrm{h}}_{\square}, \\ - \int_{\Gamma^{+}_{\square}} \delta\mathbf{t}^{\mathrm{h}} \cdot [\![\mathbf{u}^{\mathrm{h}}]\!]_{\square} \,\mathrm{d}\,\Gamma = - \int_{\Gamma^{+}_{\square}} \delta\mathbf{t}^{\mathrm{h}} \cdot (\bar{\mathbf{u}} \otimes \nabla) \cdot [\![\mathbf{x} - \bar{\mathbf{x}}]\!]_{\square} \,\mathrm{d}\,\Gamma, \; \forall \delta\mathbf{t}^{\mathrm{h}} \in \mathbb{T}^{\mathrm{h}}_{\square}. \end{aligned} \tag{2.26}$$

A mixed format is used for weak micro-periodicity. Its main features follow:

- The traction mesh $\mathcal{T}^{\mathrm{h}}$ should be more coarsely discretized than $\mathcal{U}^{\mathrm{h}}$ on $\Gamma_{\square}$ without voiding the LBB-condition (Svenning et al., 2016, p. 8).
- The tractions have no special regularity requirements: constant, linear or higher-order basis functions can be chosen (Larsson et al., 2011, p. 17).
- Strictly periodic meshes – that is, nodal positions mirrored exactly from $\Gamma^{+}_{\square}$ to $\Gamma^{-}_{\square}$ – may be used but are not required (Larsson et al., 2011, p. 18).
- Condition (2.21) is imposed via (2.24): self-equilibrating tractions do not arise naturally if (2.20) is enforced weakly (Öhman et al., 2015, p. 8).

The last point is crucial: the system of equations that arises from discretizing (2.26) can only be assembled and solved if (2.24) is used to formulate $(2.26)_{\mathrm{a}}$. That is, anti-periodicity of tractions (2.21) is imposed a priori via identity (2.24).

Construction of the Traction Mesh

In this treatise, $\mathcal{T}^{\mathrm{h}}$ is constructed for piecewise linear and continuous tractions following the procedure in (Larsson et al., 2011, pp. 17–18). The standard traction mesh is created by projecting all nodes on $\Gamma^{-}_{\square}$ and $\Gamma^{+}_{\square}$ onto $\Gamma^{+}_{\square}$. Then, $\mathcal{T}^{\mathrm{h}}$ is coarsened by removing nodes that are closer than a given tolerance to other nodes until the desired dimension of $\mathbb{T}^{\mathrm{h}}_{\square}$ has been achieved (Fig. 2.3).

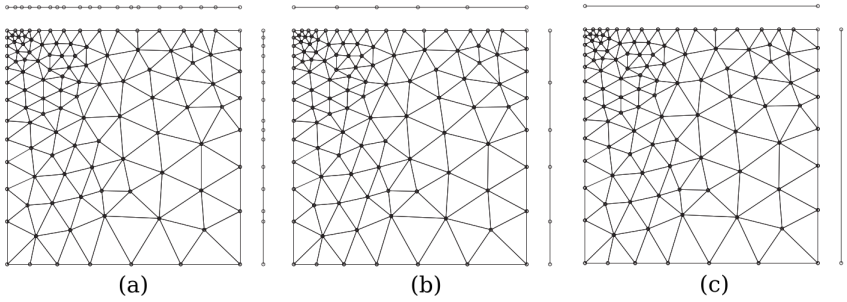

Figure 2.3: RVE: (a) standard traction mesh; (b) reduced traction mesh; (c) Neumann traction mesh. From (Larsson, Runesson, Saroukhani, and Vafadari, 2011, p. 18)

2.3.2 Dirichlet Boundary Conditions

The Galerkin discretization for the BVP with Dirichlet boundary conditions follows (Larsson et al., 2011, p. 17): Find $\mathbf{u}^{\mathrm{h}} \in \mathbb{U}^{\mathrm{D}}_{\square} \subset \mathbb{U}^{\mathrm{h}}_{\square}$ for a given $\bar{\mathbf{u}} \otimes \nabla$ that solves

$$\begin{gathered} \int_{\Omega_{\square}} \boldsymbol{\Sigma} : [\delta \mathbf{u}^{\mathrm{h}} \otimes \nabla] \, \mathrm{d}\, \Omega = 0, \; \forall \delta \mathbf{u}^{\mathrm{h}} \in \mathbb{U}^{\mathrm{D}}_{\square}(\mathbf{0}), \\ \mathbb{U}^{\mathrm{D}}_{\square}(\bar{\mathbf{u}} \otimes \nabla) = \{\mathbf{u} \in \mathbb{U}^{\mathrm{h}}_{\square}, \, \mathbf{u} = (\bar{\mathbf{u}} \otimes \nabla) \cdot (\mathbf{x} - \bar{\mathbf{x}}) \text{ on } \Gamma_{\square}\}. \end{gathered} \tag{2.27}$$

Note that the traction space $\mathbb{T}^{\mathrm{h}}_{\square}$ is left unrestricted. On the other hand, $\mathbb{U}^{\mathrm{D}}_{\square}$ restricts displacement of the boundary nodes to (Kouznetsova et al., 2010, p. 16)

$$\mathbf{u}_{\mathrm{p},i} = (\bar{\mathbf{u}} \otimes \nabla) \cdot (\mathbf{x}_{\mathrm{p},i} - \bar{\mathbf{x}}) \text{ for } i = 1, 2, \cdots, n_{\mathrm{p}}, \tag{2.28}$$

where p stands for prescribed and n_{p} is the total number of prescribed nodes. The nonlinear system of equations from (2.27) is assembled and partitioned:

$$\begin{bmatrix} \mathbf{K}_{\mathrm{ff}} & \mathbf{K}_{\mathrm{fp}} \\ \mathbf{K}_{\mathrm{pf}} & \mathbf{K}_{\mathrm{pp}} \end{bmatrix} \begin{Bmatrix} \mathbf{u}_{\mathrm{f}} \\ \mathbf{u}_{\mathrm{p}} \end{Bmatrix} = \begin{Bmatrix} 0 \\ -\mathbf{f}_{\mathrm{i}} \end{Bmatrix}, \tag{2.29}$$

where $\mathbf{f}_{\mathrm{i}}$ is the internal reaction force vector at the prescribed nodes. System (2.29) can be solved using, for instance, displacement control Newton-Raphson. Per (Kouznetsova et al., 2010, p. 19), the macroscopic stress tensor is given by

$$\bar{\boldsymbol{\Sigma}} = \frac{1}{|\Omega_{\square}|} \sum_{i=1}^{n_{\mathrm{p}}} \mathbf{f}_i \otimes (\mathbf{x}_i - \bar{\mathbf{x}}), \tag{2.30}$$

where $\mathbf{f}_i$ are the resulting external forces at the boundary nodes.

2.3.3 Strong Periodic Boundary Conditions

The Galerkin discretization for the BVP with strong periodic boundary conditions follows: Find $\mathbf{u}^{\mathrm{h}} \in \mathbb{U}^{\mathrm{S}}_{\square} \subset \mathbb{U}^{\mathrm{h}}_{\square}$ for a given $\bar{\mathbf{u}} \otimes \nabla$ that solves

$$\begin{aligned} \int_{\Omega_{\square}} \boldsymbol{\Sigma} : [\delta \mathbf{u}^{\mathrm{h}} \otimes \nabla] \, \mathrm{d}\, \Omega = 0, \; \forall \delta \mathbf{u}^{\mathrm{h}} \in \mathbb{U}^{\mathrm{S}}_{\square}(\mathbf{0}), \\ \mathbb{U}^{\mathrm{S}}_{\square}(\bar{\mathbf{u}} \otimes \nabla) = \{\mathbf{u} \in \mathbb{U}^{\mathrm{h}}_{\square}, [\![\mathbf{u}]\!]_{\square} = (\bar{\mathbf{u}} \otimes \nabla) \cdot [\![\mathbf{x} - \bar{\mathbf{x}}]\!]_{\square} \text{ on } \Gamma^{+}_{\square}\}. \end{aligned} \tag{2.31}$$

The traction space $\mathbb{T}^{\mathrm{h}}_{\square}$ is left unrestricted. Additionally, $\mathbb{T}^{\mathrm{h}}_{\square}$ equals the trace of $\mathbb{U}^{\mathrm{h}}_{\square}$ on $\Gamma^{-}_{\square}$ and $\Gamma^{+}_{\square}$,[5] which means $[\![\mathbf{u}^{\mathrm{h}}_{\mathrm{s}}]\!]_{\square} \in \mathbb{T}^{\mathrm{h}}_{\square}$. Thus, is is possible to choose $\delta \mathbf{t} = [\![\mathbf{u}^{\mathrm{h}}_{\mathrm{s}}]\!]_{\square} \in \mathbb{T}^{\mathrm{h}}_{\square}$. Then, the only solution to $(2.26)_{\mathrm{b}}$ is $[\![\mathbf{u}^{\mathrm{h}}_{\mathrm{s}}]\!]_{\square} = 0$ (Larsson et al., 2011, p. 18; Svenning et al., 2016, p. 6). Strong periodic boundary conditions are enforced on strictly periodic meshes by treating two degrees of freedom on opposing sides as a single degree of freedom, i.e. master-slave elimination (Sandström et al., 2014, p. 2). Consider the RVE in Fig. 2.2(b). Let nodes 1,2 and 4 abide by Eq. (2.28). For the remaining nodes, (2.20) is rewritten in a format more suitable for FEM (Kouznetsova et al., 2010, p. 17). For 2D, the RVE edges are renamed T, B, R and L (top, bottom, right and left) such that

$$\begin{aligned} \mathbf{u}_{\mathrm{T}} = \mathbf{u}_{\mathrm{B}} + (\bar{\mathbf{u}} \otimes \nabla) \cdot (\mathbf{x}_4 - \mathbf{x}_1) = \mathbf{u}_{\mathrm{B}} + \mathbf{u}_{\mathrm{p},4} - \mathbf{u}_{\mathrm{p},1}, \\ \mathbf{u}_{\mathrm{R}} = \mathbf{u}_{\mathrm{L}} + (\bar{\mathbf{u}} \otimes \nabla) \cdot (\mathbf{x}_2 - \mathbf{x}_1) = \mathbf{u}_{\mathrm{L}} + \mathbf{u}_{\mathrm{p},2} - \mathbf{u}_{\mathrm{p},1}, \\ \mathbf{u}_{\mathrm{p},i} = (\bar{\mathbf{u}} \otimes \nabla) \cdot (\mathbf{x}_i - \bar{\mathbf{x}}) \text{ for } i = 1, 2, 4. \end{aligned} \tag{2.32}$$

Let $\mathbf{u}_{\mathrm{i}}$ be the independent (master) degrees of freedom and $\mathbf{u}_{\mathrm{d}}$ be the dependent (slave) degrees of freedom.[6] Equations (2.31) and (2.32) are then recast as

$$\begin{bmatrix} \mathbf{C}_{\mathrm{i}} & \mathbf{C}_{\mathrm{d}} \end{bmatrix} \begin{Bmatrix} \mathbf{u}_{\mathrm{i}} \\ \mathbf{u}_{\mathrm{d}} \end{Bmatrix} = \mathbf{0} \xrightarrow{\text{yields}} \mathbf{u}_{\mathrm{d}} = -\mathbf{C}_{\mathrm{d}}^{-1} \mathbf{C}_{\mathrm{i}} \mathbf{u}_{\mathrm{i}} \tag{2.33}$$

Consider the system of equations with only the boundary degrees of freedom:

$$\begin{bmatrix} \mathbf{K}_{\mathrm{ii}} & \mathbf{K}_{\mathrm{id}} \\ \mathbf{K}_{\mathrm{di}} & \mathbf{K}_{\mathrm{dd}} \end{bmatrix} \begin{Bmatrix} \delta \mathbf{u}_{\mathrm{i}} \\ \delta \mathbf{u}_{\mathrm{d}} \end{Bmatrix} = \begin{Bmatrix} \delta \mathbf{r}_{\mathrm{i}} \\ \delta \mathbf{r}_{\mathrm{d}} \end{Bmatrix}. \tag{2.34}$$

Letting $\mathbf{C}_{\mathrm{di}} = -\mathbf{C}_{\mathrm{d}}^{-1} \mathbf{C}_{\mathrm{i}}$, (2.34) can be re-framed as

$$[\mathbf{K}_{\mathrm{ii}} + \mathbf{K}_{\mathrm{id}} \mathbf{C}_{\mathrm{di}} + \mathbf{C}_{\mathrm{di}}^{\top} \mathbf{K}_{\mathrm{di}} + \mathbf{C}_{\mathrm{di}}^{\top} \mathbf{K}_{\mathrm{dd}} \mathbf{C}_{\mathrm{di}}] \delta \mathbf{u}_{\mathrm{i}} = \{\delta \mathbf{r}_{\mathrm{i}} + \mathbf{C}_{\mathrm{di}}^{\top} \delta \mathbf{r}_{\mathrm{d}}\} \tag{2.35}$$

That is, the dependent nodes have been eliminated from the system of equations. Per (Kouznetsova et al., 2010, pp. 19–20), the anti-periodic tractions arise naturally from this formulation. Thus, the macroscopic stress tensor is simply

$$\bar{\boldsymbol{\Sigma}} = \frac{1}{|\Omega_{\square}|} \sum_{i=1,2,4} \mathbf{f}_i \otimes (\mathbf{x}_i - \bar{\mathbf{x}}), \tag{2.36}$$

where $\mathbf{f}_i$ are the reaction forces at the three prescribed corner nodes in Fig. 2.2. Instead of prescribing $(\bar{\mathbf{u}} \otimes \nabla)$, it is possible to apply $\mathbf{f}_i$ to represent $\bar{\boldsymbol{\Sigma}}$. In other words, periodic boundary conditions can be used in force-driven procedures.

[5] The standard traction mesh is applied to a strictly periodic mesh, thus $\mathbb{T}^{-}_{\square} = \mathbb{T}^{+}_{\square} = \mathbb{T}^{\mathrm{h}}_{\square}$.

[6] The choice of $\mathbf{u}_{\mathrm{i}}$ is arbitrary, but it must include $\mathbf{u}_{\mathrm{p}}$.

2.3.4 Neumann Boundary Conditions

The Galerkin discretization for the Neumann boundary conditions follows (Larsson et al., 2011, p. 17): Find $\mathbf{u}^{\mathrm{h}} \in \mathbb{U}^{\mathrm{h}}_{\square}$ and $\bar{\boldsymbol{\Sigma}} \in \mathbb{R}^{3\times 3}$ given $\bar{\mathbf{u}} \otimes \nabla$ that solves

$$\begin{aligned} \int_{\Omega_{\square}} \boldsymbol{\Sigma} : [\delta\mathbf{u}^{\mathrm{h}} \otimes \nabla] \,\mathrm{d}\,\Omega - \int_{\Gamma^{+}_{\square}} (\bar{\boldsymbol{\Sigma}} \cdot \hat{\mathbf{n}}) \cdot [\![\delta\mathbf{u}^{\mathrm{h}}]\!]_{\square} \,\mathrm{d}\,\Gamma = 0, \; \forall \delta\mathbf{u}^{\mathrm{h}} \in \mathbb{U}^{\mathrm{h}}_{\square}, \\ - \int_{\Gamma^{+}_{\square}} (\delta\bar{\boldsymbol{\Sigma}} \cdot \hat{\mathbf{n}}) \cdot [\![\mathbf{u}^{\mathrm{h}}]\!]_{\square} \,\mathrm{d}\,\Gamma = -\delta\bar{\boldsymbol{\Sigma}} : [\bar{\mathbf{u}} \otimes \nabla], \; \forall \delta\bar{\boldsymbol{\Sigma}} \in \mathbb{R}^{3\times 3}. \end{aligned} \tag{2.37}$$

Neumann boundary conditions constitute the weakest form of micro-periodicity: $\mathcal{T}^{\mathrm{h}}$ has a single element with constant traction in each RVE face (Fig 2.4(c)). That is, $\mathbb{T}^{\mathrm{N}}_{\square}$ is restricted to constant tractions given by $\bar{\boldsymbol{\Sigma}}\cdot\hat{\mathbf{n}}$ (Larsson et al., 2011, pp. 11–18; Svenning et al., 2016, p. 6). Also note that, opposite to the Dirichlet boundary conditions, the displacement space $\mathbb{U}^{\mathrm{h}}_{\square}$ is now left unrestricted.

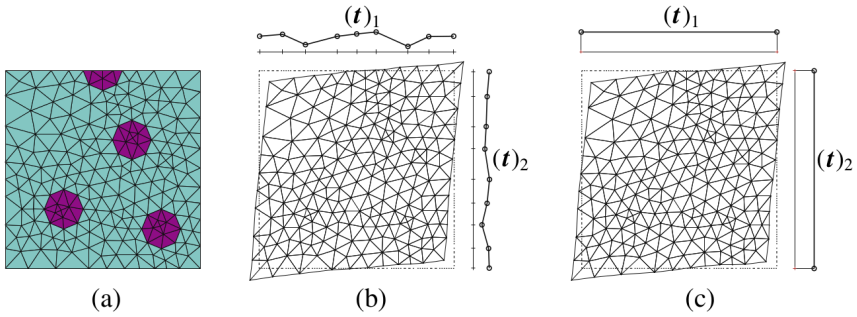

Figure 2.4: (a) Particle-matrix composite. Macroscale shear deformation: (b) weak periodic boundary conditions; (c) Neumann boundary conditions (Larsson, Runesson, Saroukhani, and Vafadari, 2011, p. 16)

Table 2.3 summarizes and compares the boundary conditions discussed herein. Overall, weak periodic boundary conditions present a more general formulation which fills the gap between strong periodic and Neumann boundary conditions.

Table 2.3: Comparison of classical and weak periodic boundary conditions

	Dirichlet	**Periodic**	**Weak Periodic**	**Neumann**
Traction Space $\mathbb{T}^{\mathrm{h}}$	unrestricted	unrestricted	partially restricted	restricted
Disp. Space $\mathbb{U}^{\mathrm{h}}$	restricted	partially restricted	weakly restricted	unrestricted
Traction Mesh $\mathcal{T}^{\mathrm{h}}$	projection $\mathbb{U}^{\mathrm{h}}$ onto $\Gamma_{\square}$	standard mesh	coarser mesh	coarsest mesh

Chapter 3

IMPLEMENTATION

The Galerkin approximation of the weak form of the BVP - described by (2.26) - is solved by discretizing the domain and boundary ($\Omega_\square$ and $\Gamma_\square$) into finite-sized elements with known test functions ($\delta\mathbf{u}^\mathrm{h}$ and $\delta\mathbf{t}^\mathrm{h}$). This involves the creation of a displacement mesh and a traction mesh ($\mathcal{U}^\mathrm{h}$ and $\mathcal{T}^\mathrm{h}$) with shape functions for each node. In Section 3.1, (2.26) is discretized using these functions. Subsections 3.1.1 and 3.1.2 linearize these equations so they can be solved iteratively, e.g. using Newton-Raphson methods. Subsequently, Section 3.2 describes the C++ implementation of these equations using the Jem and Jive libraries by (Dynaflow Research Group, n.d.).

3.1 FEM Discretization

First, the second order tensors in $(2.26)_\mathrm{a}$ are rewritten as vectors using Voigt notation:

$$\int_{\Omega_\square} \varepsilon(\delta\mathbf{u}^\mathrm{h}) \cdot \sigma(\mathbf{u}^\mathrm{h}) \,\mathrm{d}\,\Omega - \int_{\Gamma^+_\square} \mathbf{t}^\mathrm{h} \cdot [\![\delta\mathbf{u}^\mathrm{h}]\!]_\square \,\mathrm{d}\,\Gamma = 0,\ \forall\delta\mathbf{u}^\mathrm{h} \in \mathbb{U}^\mathrm{h}_\square, \tag{3.1}$$

where $\varepsilon(\delta\mathbf{u}^\mathrm{h}) \equiv \delta\mathbf{u}^\mathrm{h} \otimes \nabla$ and $\sigma(\mathbf{u}^\mathrm{h}) \equiv \boldsymbol{\Sigma}$. The finite-dimensional spaces of trial solutions $\mathbb{U}^\mathrm{h}_\square$ and $\mathbb{T}^\mathrm{h}_\square$ are constructed by limiting $\mathbf{u}^\mathrm{h}$ and $\mathbf{t}^\mathrm{h}$ to vary linearly over each element in $\mathcal{U}^\mathrm{h}$ and $\mathcal{T}^\mathrm{h}$. This is achieved by introducing linearly independent shape functions $n_i(\mathbf{x})$ and $h_j(\mathbf{x})$ for each node i in $\mathcal{U}^\mathrm{h}$ and j in $\mathcal{T}^\mathrm{h}$. The shape functions have a value of 1 at their corresponding node and 0 in all other nodes. $\mathbf{u}^\mathrm{h}$ and $\mathbf{t}^\mathrm{h}$ are then described by linear combinations of the shape functions times their corresponding discrete nodal values, or

$$\mathbf{u}^\mathrm{h} \triangleq \mathbf{N} \cdot \hat{\mathbf{u}}, \tag{3.2}$$

$$\mathbf{t}^\mathrm{h} \triangleq \mathbf{H} \cdot \hat{\mathbf{t}}, \tag{3.3}$$

where $\mathbf{N}$ and $\mathbf{H}$ are the matrices of shape functions associated with $\mathcal{U}^\mathrm{h}$ and $\mathcal{T}^\mathrm{h}$, and $\hat{\mathbf{u}}$ and $\hat{\mathbf{t}}$ are vectors of nodal displacements and nodal tractions, respectively.

The Bubnov-Galerkin approximation requires that the weight and trial functions originate from the same finite-dimensional space (Wells, 2009, p. 32), hence

$$\delta\mathbf{u}^{\mathrm{h}} \triangleq \mathbf{N}\cdot\delta\hat{\mathbf{u}}, \tag{3.4}$$

$$\delta\mathbf{t}^{\mathrm{h}} \triangleq \mathbf{H}\cdot\delta\hat{\mathbf{t}}. \tag{3.5}$$

The vector $\hat{\mathbf{u}}$ includes the boundary displacements $\hat{\mathbf{u}}^+$ and $\hat{\mathbf{u}}^-$ on $\Gamma^+_\square$ and $\Gamma^-_\square$. There are elements on the boundary of $\mathcal{U}^h$ with shape functions contained in $\mathbf{N}^+$ and $\mathbf{N}^-$ that map said boundary displacements onto $\mathbf{u}^{\mathrm{h}+}$ and $\mathbf{u}^{\mathrm{h}-}$, thus

$$\begin{aligned}\llbracket\mathbf{u}^{\mathrm{h}}\rrbracket_\square &= \mathbf{N}^+\cdot\hat{\mathbf{u}}^+ - \mathbf{N}^-\cdot\hat{\mathbf{u}}^-,\\ \llbracket\delta\mathbf{u}^{\mathrm{h}}\rrbracket_\square &= \mathbf{N}^+\cdot\delta\hat{\mathbf{u}}^+ - \mathbf{N}^-\cdot\delta\hat{\mathbf{u}}^-.\end{aligned} \tag{3.6}$$

Au contraire, $\hat{\mathbf{t}}$ comprises only the nodal boundary tractions on $\Gamma^+_\square$.[1] Now, the vector $\hat{\mathbf{u}}$ is mapped onto the strain vector ε via the so-called $\mathbf{B}$-matrix:

$$\varepsilon(\delta\mathbf{u}^{\mathrm{h}}) \triangleq \mathbf{B}\cdot\delta\hat{\mathbf{u}}. \tag{3.7}$$

Subsequently, the linear-elastic material stiffness matrix ($\mathbf{D}$) maps ε into σ, or

$$\sigma(\mathbf{u}^{\mathrm{h}}) \triangleq \mathbf{DB}\cdot\hat{\mathbf{u}}. \tag{3.8}$$

The system of equations needs to be linearized to include material nonlinearities in the form of tangent stiffness operators.[2] Substituting the preceding definitions into (3.1) yields the finite element discretization of the Galerkin approximation:

$$\int_{\Omega_\square}(\mathbf{B}\cdot\delta\hat{\mathbf{u}})\cdot(\mathbf{DB}\cdot\hat{\mathbf{u}})\,\mathrm{d}\,\Omega - \int_{\Gamma^+_\square}(\mathbf{N}^+\cdot\delta\hat{\mathbf{u}}^+ - \mathbf{N}^-\cdot\delta\hat{\mathbf{u}}^-)\cdot(\mathbf{H}\cdot\hat{\mathbf{t}})\,\mathrm{d}\,\Gamma = 0. \tag{3.9}$$

Equation (3.9) is rendered into a format suitable for computer implementation:

$$\delta\hat{\mathbf{u}}\cdot\mathbf{K}_{\mathrm{uu}}\cdot\hat{\mathbf{u}} - \delta\hat{\mathbf{u}}^+\cdot\mathbf{K}^+_{\mathrm{ut}}\cdot\hat{\mathbf{t}} + \delta\hat{\mathbf{u}}^-\cdot\mathbf{K}^-_{\mathrm{ut}}\cdot\hat{\mathbf{t}} = 0, \tag{3.10}$$

where

$$\begin{aligned}\mathbf{K}_{\mathrm{uu}} &= \left[\int_{\Omega_\square}\mathbf{B}^\top\mathbf{DB}\,\mathrm{d}\,\Omega\right],\\ \mathbf{K}^+_{\mathrm{ut}} &= \left[\int_{\Gamma^+_\square}\mathbf{N}^{+\top}\mathbf{H}\,\mathrm{d}\,\Gamma\right],\\ \mathbf{K}^-_{\mathrm{ut}} &= \left[\int_{\Gamma^+_\square}\mathbf{N}^{-\top}\mathbf{H}\,\mathrm{d}\,\Gamma\right].\end{aligned}$$

The global stiffness matrix $\mathbf{K}_{\mathrm{uu}}$ is evaluated as usual. The matrices $\mathbf{K}^+_{\mathrm{ut}}$ and $\mathbf{K}^-_{\mathrm{ut}}$ augment $\mathbf{K}_{\mathrm{uu}}$ to form a so-called bordered stiffness matrix, $\mathbf{K}_0$ (See subsection

[1] The condition of anti-periodicity of tractions in (2.21) stipulates that $\mathbf{t}^+ = -\mathbf{t}^-$.

[2] Hereinafter, the tangent stiffness operators are denoted by $\mathbf{D}$ and map $\dot{\varepsilon}$ onto $\dot{\sigma}$.

3.2.7). Equation (3.10) represents the discretized version of the equilibrium equation. Having added new degrees of freedom in the form of $\hat{\mathbf{t}}$, additional equations are required to keep the linearized problem well-posed. These additional equations follow from the weak micro-periodicity requirement in $(2.26)_{\mathrm{b}}$:

$$-\int_{\Gamma^+_\square} \delta\mathbf{t}^{\mathrm{h}} \cdot [\![\mathbf{u}^{\mathrm{h}}]\!]_\square \,\mathrm{d}\,\Gamma = -\int_{\Gamma^+_\square} \delta\mathbf{t}^{\mathrm{h}} \cdot (\bar{\mathbf{u}} \otimes \nabla) \cdot (\mathbf{x}^+ - \mathbf{x}^-) \,\mathrm{d}\,\Gamma,\ \forall \delta\mathbf{t}^{\mathrm{h}} \in \mathbb{T}^{\mathrm{h}}_\square. \quad (3.11)$$

Substituting the definitions (3.5) and (3.6) into (3.11), the Galerkin form of the weak micro-periodicity requirement is cast into the finite element discretization:

$$-\int_{\Gamma^+_\square} (\mathbf{H} \cdot \delta\hat{\mathbf{t}}) \cdot (\mathbf{N}^+ \cdot \hat{\mathbf{u}}^+ - \mathbf{N}^- \cdot \hat{\mathbf{u}}^-) \,\mathrm{d}\,\Gamma = -\int_{\Gamma^+_\square} (\mathbf{H} \cdot \delta\hat{\mathbf{t}}) \cdot (\bar{\mathbf{u}} \otimes \nabla) \cdot (\mathbf{x}^+ - \mathbf{x}^-) \,\mathrm{d}\,\Gamma. \quad (3.12)$$

Equation (3.12) is rendered into a format suitable for computer implementation:

$$-\mathbf{K}^+_{\mathrm{tu}} \cdot \hat{\mathbf{u}}^+ + \mathbf{K}^-_{\mathrm{tu}} \cdot \hat{\mathbf{u}}^- = \mathbf{f}^{\mathrm{t}}_{\mathrm{ext}}, \quad (3.13)$$

where

$$\mathbf{K}^+_{\mathrm{tu}} = \left[\int_{\Gamma^+_\square} \mathbf{H}^\top \mathbf{N}^+ \,\mathrm{d}\,\Gamma\right] = {\mathbf{K}^+_{\mathrm{ut}}}^\top,$$

$$\mathbf{K}^-_{\mathrm{tu}} = \left[\int_{\Gamma^+_\square} \mathbf{H}^\top \mathbf{N}^- \,\mathrm{d}\,\Gamma\right] = {\mathbf{K}^-_{\mathrm{ut}}}^\top,$$

$$\mathbf{f}^{\mathrm{t}}_{\mathrm{ext}} = -\int_{\Gamma^+_\square} \mathbf{H}^\top \cdot ((\bar{\mathbf{u}} \otimes \nabla) \cdot (\mathbf{x}^+ - \mathbf{x}^-)) \,\mathrm{d}\,\Gamma.$$

The transpose of matrices $\mathbf{K}^+_{\mathrm{ut}}$ and $\mathbf{K}^-_{\mathrm{ut}}$ also augment $\mathbf{K}_{\mathrm{uu}}$ to form $\mathbf{K}_0$.

3.1.1 Nonlinear Solution With Prescribed Strain

For an iterative solution, equations (3.1) and (3.11) must be expressed as follows:

$$\mathbf{K}_0 \begin{Bmatrix} \Delta\hat{\mathbf{u}} \\ \Delta\hat{\mathbf{t}} \end{Bmatrix} = \mathbf{f}^{t+\Delta t}_{\mathrm{ext}} - \mathbf{f}_{\mathrm{int}}(\hat{\mathbf{u}}^t, \hat{\mathbf{t}}^t), \quad (3.14)$$

where $\mathbf{K}_0$ is the bordered tangent stiffness matrix, $\mathbf{f}^{t+\Delta t}_{\mathrm{ext}}$ is the vector of externally applied forces at time $t + \Delta t$ and $\mathbf{f}_{\mathrm{int}}(\hat{\mathbf{u}}^t, \hat{\mathbf{t}}^t)$ is the vector of internal (reaction) forces due to displacements and tractions evaluated at time t. The solution increment vector is given by $\Delta\hat{\mathbf{t}} = \hat{\mathbf{t}}^{t+\Delta t} - \hat{\mathbf{t}}^t$ and $\Delta\hat{\mathbf{u}} = \hat{\mathbf{u}}^{t+\Delta t} - \hat{\mathbf{u}}^t$. (3.14) is obtained by letting $\mathbf{t}^{\mathrm{h}} \to \mathbf{t}^{\mathrm{h}} + \Delta\mathbf{t}^{\mathrm{h}}$ and $\mathbf{u}^{\mathrm{h}} \to \mathbf{u}^{\mathrm{h}} + \Delta\mathbf{t}^{\mathrm{h}}$. Consider (3.1):

$$\left\{\int_{\Omega_\square} \varepsilon(\delta\mathbf{u}^{\mathrm{h}}) \cdot \sigma(\Delta\mathbf{u}^{\mathrm{h}}) \,\mathrm{d}\,\Omega - \int_{\Gamma^+_\square} \Delta\mathbf{t}^{\mathrm{h}} \cdot [\![\delta\mathbf{u}^{\mathrm{h}}]\!]_\square \,\mathrm{d}\,\Gamma\right\} = -\left\{\int_{\Omega_\square} \varepsilon(\delta\mathbf{u}^{\mathrm{h}}) \cdot \sigma(\mathbf{u}^{\mathrm{h}}) \,\mathrm{d}\,\Omega - \int_{\Gamma^+_\square} \mathbf{t}^{\mathrm{h}} \cdot [\![\delta\mathbf{u}^{\mathrm{h}}]\!]_\square \,\mathrm{d}\,\Gamma\right\},\ \forall \delta\mathbf{u}^{\mathrm{h}} \in \mathbb{U}^{\mathrm{h}}_\square. \quad (3.15)$$

Substituting definitions (3.4) through (3.8), the system (3.15) is rendered into the finite element discretization suitable for computer implementation:

$$\Big\{\delta\hat{\mathbf{u}}\cdot\mathbf{K}_{\mathrm{uu}}\cdot\Delta\hat{\mathbf{u}}-\delta\hat{\mathbf{u}}^{+}\cdot\mathbf{K}_{\mathrm{ut}}^{+}\cdot\Delta\hat{\mathbf{t}}+\delta\hat{\mathbf{u}}^{-}\cdot\mathbf{K}_{\mathrm{ut}}^{-}\cdot\Delta\hat{\mathbf{t}}\Big\}= \\ -\Big\{\delta\hat{\mathbf{u}}\cdot\int_{\Omega_{\square}}\mathbf{B}^{\top}\sigma(\hat{\mathbf{u}})\,\mathrm{d}\,\Omega-\delta\hat{\mathbf{u}}^{+}\cdot\mathbf{K}_{\mathrm{ut}}^{+}\cdot\hat{\mathbf{t}}+\delta\hat{\mathbf{u}}^{-}\cdot\mathbf{K}_{\mathrm{ut}}^{-}\cdot\hat{\mathbf{t}}\Big\}. \quad (3.16)$$

The matrices $\mathbf{K}_{\mathrm{ut}}^{+}$ and $\mathbf{K}_{\mathrm{ut}}^{-}$ – given by (3.10) – augment $\mathbf{K}_{\mathrm{uu}}$ to form $\mathbf{K}_0$. Likewise, the vectors -$\mathbf{K}_{\mathrm{ut}}^{+}\cdot\hat{\mathbf{t}}$ and $\mathbf{K}_{\mathrm{ut}}^{-}\cdot\hat{\mathbf{t}}$ are added to $\mathbf{f}_{\mathrm{int}}$. Now, consider (3.11):

$$\Big\{-\int_{\Gamma_{\square}^{+}}\delta\mathbf{t}^{\mathrm{h}}\cdot[\![\Delta\mathbf{u}^{\mathrm{h}}]\!]_{\square}\,\mathrm{d}\,\Gamma\Big\}=-\int_{\Gamma_{\square}^{+}}\delta\mathbf{t}^{\mathrm{h}}\cdot(\bar{\mathbf{u}}\otimes\nabla)\cdot(\mathbf{x}^{+}-\mathbf{x}^{-})\,\mathrm{d}\,\Gamma \\ -\Big\{-\int_{\Gamma_{\square}^{+}}\delta\mathbf{t}^{\mathrm{h}}\cdot[\![\mathbf{u}^{\mathrm{h}}]\!]_{\square}\,\mathrm{d}\,\Gamma\Big\},\ \forall\delta\mathbf{t}^{\mathrm{h}}\in\mathbb{T}_{\square}^{\mathrm{h}}. \quad (3.17)$$

Substituting definitions (3.5) and (3.6), the system (3.17) is rendered into the appropriate finite element discretization suitable for computer implementation:

$$\Big\{-\mathbf{K}_{\mathrm{tu}}^{+}\cdot\Delta\hat{\mathbf{u}}^{+}+\mathbf{K}_{\mathrm{tu}}^{-}\cdot\Delta\hat{\mathbf{u}}^{-}\Big\}=\mathbf{f}_{\mathrm{ext}}^{\mathrm{t}}-\Big\{-\mathbf{K}_{\mathrm{tu}}^{+}\cdot\hat{\mathbf{u}}^{+}+\mathbf{K}_{\mathrm{tu}}^{-}\cdot\hat{\mathbf{u}}^{-}\Big\}. \quad (3.18)$$

The matrices $\mathbf{K}_{\mathrm{tu}}^{+}$ and $\mathbf{K}_{\mathrm{tu}}^{-}$ and the vector $\mathbf{f}_{\mathrm{ext}}^{\mathrm{t}}$ are given by (3.13).

3.1.2 Nonlinear Solution with Prescribed Force

One goal of this treatise is to present a formulation in which it is possible to prescribe forces at the corner nodes instead of a macroscopic strain tensor. Assuming $(\bar{\mathbf{u}}\otimes\nabla)$ is imposed on the corner nodes as in (2.32), $\mathbf{f}_{\mathrm{ext}}^{\mathrm{t}}$ reduces to

$$\mathbf{f}_{\mathrm{ext}}^{\mathrm{t}}=-\int_{\Gamma_{\square}^{+}}\mathbf{H}^{\top}\cdot(\hat{\mathbf{u}}_{\mathrm{cor}}^{+}-\hat{\mathbf{u}}_{\mathrm{cor}}^{-})\,\mathrm{d}\,\Gamma. \quad (3.19)$$

$\hat{\mathbf{u}}_{\mathrm{cor}}^{+}$ is the displacement of a corner $\mathbf{x}_{\mathrm{cor}}^{+}$ on $\Gamma_{\square}^{+}$ and $\hat{\mathbf{u}}_{\mathrm{cor}}^{-}=\mathbf{u}(\varphi_{\mathrm{per}}(\mathbf{x}_{\mathrm{cor}}^{+}))$ on $\Gamma_{\square}^{-}$. The micro-periodicity requirement in (3.11) is modified per (3.19) such that

$$-\int_{\Gamma_{\square}^{+}}\delta\mathbf{t}^{\mathrm{h}}\cdot[\![\mathbf{u}^{\mathrm{h}}]\!]_{\square}\,\mathrm{d}\,\Gamma+\int_{\Gamma_{\square}^{+}}\delta\mathbf{t}^{\mathrm{h}}\cdot(\hat{\mathbf{u}}_{\mathrm{cor}}^{+}-\hat{\mathbf{u}}_{\mathrm{cor}}^{-})\,\mathrm{d}\,\Gamma=0. \quad (3.20)$$

The assumption that $(\bar{\mathbf{u}}\otimes\nabla)$ is prescribed and enforced on $\hat{\mathbf{u}}_{\mathrm{cor}}^{\pm}$ gives rise to reaction forces at the corners which adhere to (2.36) by enforcing (2.21). That is, they are representative of the macroscopic stress. Instead of doing this, it is possible to apply the reaction forces at the corners and solve for $\hat{\mathbf{u}}_{\mathrm{cor}}^{\pm}$ iteratively.

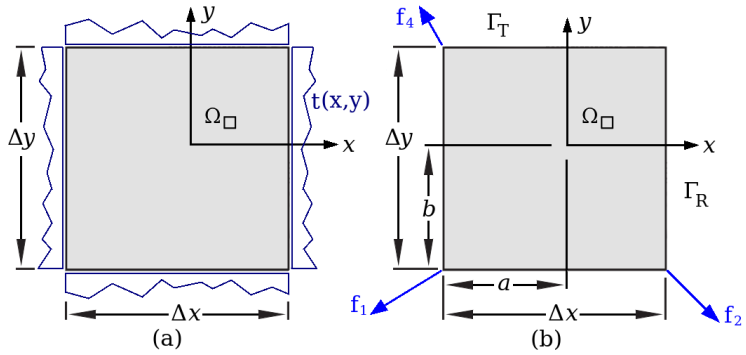

Figure 3.1: RVE: (a) anti-periodic tractions; (b) corner forces

Consider forces $\mathbf{f}_2$ and $\mathbf{f}_4$ on nodes 2 and 4 in Fig. 3.1. It is first proven that

$$\int_{\Gamma_R} \mathbf{t}\,\mathrm{d}\,\Gamma = \mathbf{f}_2 \text{ and } \int_{\Gamma_T} \mathbf{t}\,\mathrm{d}\,\Gamma = \mathbf{f}_4. \tag{3.21}$$

Per (Kouznetsova et al., 2010, p. 13), the macroscopic stress tensor is given by

$$\bar{\boldsymbol{\Sigma}} = \frac{1}{|\Omega_\square|}\int_{\Gamma_\square} \mathbf{t}\otimes(\mathbf{x}-\bar{\mathbf{x}})\,\mathrm{d}\,\Gamma = \frac{1}{|\Omega_\square|}\begin{bmatrix}\Delta x\int_{\Gamma_R} t_x\,\mathrm{d}\,y & \Delta y\int_{\Gamma_T} t_x\,\mathrm{d}\,x\\ \Delta x\int_{\Gamma_R} t_y\,\mathrm{d}\,y & \Delta y\int_{\Gamma_T} t_y\,\mathrm{d}\,x\end{bmatrix}. \tag{3.22}$$

The macroscopic stress tensor also equals to (Kouznetsova et al., 2010, p. 21):

$$\bar{\boldsymbol{\Sigma}} = \frac{1}{|\Omega_\square|}\sum_{i=1,2,4}\mathbf{f}_i\otimes(\mathbf{x}_i-\bar{\mathbf{x}}) = \frac{1}{|\Omega_\square|}\begin{bmatrix}\Delta x f_{x2} & \Delta y f_{x4}\\ \Delta x f_{y2} & \Delta y f_{y4}\end{bmatrix}. \tag{3.23}$$

Noting that $\Delta x \neq 0$ and $\Delta y \neq 0$ and equating (3.22) to (3.23) results in

$$\begin{aligned}\int_{\Gamma_R} t_x\,\mathrm{d}\,\Gamma &= f_{x2}, & \int_{\Gamma_R} t_y\,\mathrm{d}\,\Gamma &= f_{y2},\\ \int_{\Gamma_T} t_x\,\mathrm{d}\,\Gamma &= f_{x4}, & \int_{\Gamma_T} t_y\,\mathrm{d}\,\Gamma &= f_{y4}.\end{aligned} \tag{3.24}$$

(3.24) is simplified to (3.21), thereby completing the proof.[3] For brevity, $\mathbf{f}_2$ and $\mathbf{f}_4$ are now denoted $\mathbf{f}^+_{\mathrm{cor}}$ (which represents the sum of all corner forces on $\Gamma^+_\square$):

$$\int_{\Gamma^+_\square} \mathbf{t}\,\mathrm{d}\,\Gamma = \mathbf{f}^+_{\mathrm{cor}}. \tag{3.25}$$

Equation (3.25) makes reference to only the forces on $\Gamma^+_\square$. The reason is that $\hat{\mathbf{u}}^-_{\mathrm{cor}}$ is set to zero. Therefore, prescribing a force on that corner becomes redundant.

[3]The complete derivations required for the proof are relegated to Appendix B.

All terms that need to be solved for are incorporated into the potential energy:

$$\Pi(\mathbf{u}^{\mathrm{h}}, \mathbf{t}^{\mathrm{h}}) = \int_{\Omega_\square} \varepsilon \cdot \sigma \,\mathrm{d}\,\Omega - \int_{\Gamma^+_\square} \mathbf{t}^{\mathrm{h}} \cdot [\![\mathbf{u}^{\mathrm{h}}]\!]_\square \,\mathrm{d}\,\Gamma + \left(\int_{\Gamma^+_\square} \mathbf{t}^{\mathrm{h}} \,\mathrm{d}\,\Gamma - \mathbf{f}^+_{\mathrm{cor}} \right) \cdot (\hat{\mathbf{u}}^+_{\mathrm{cor}} - \hat{\mathbf{u}}^-_{\mathrm{cor}}). \quad (3.26)$$

The potential energy is minimized to derive the governing equations. This is achieved by finding the variation of Π and setting it equal to zero:

$$\begin{aligned}\delta\Pi(\mathbf{u}^{\mathrm{h}}, \mathbf{t}^{\mathrm{h}}, \delta\mathbf{u}^{\mathrm{h}}, \delta\mathbf{t}^{\mathrm{h}}) = {} & \int_{\Omega_\square} \delta\varepsilon \cdot \sigma \,\mathrm{d}\,\Omega - \int_{\Gamma^+_\square} \mathbf{t}^{\mathrm{h}} \cdot [\![\delta\mathbf{u}^{\mathrm{h}}]\!]_\square \,\mathrm{d}\,\Gamma + \left(\int_{\Gamma^+_\square} \mathbf{t}^{\mathrm{h}} \,\mathrm{d}\,\Gamma - \mathbf{f}^+_{\mathrm{cor}} \right) \cdot (\delta\hat{\mathbf{u}}^+_{\mathrm{cor}} - \delta\hat{\mathbf{u}}^-_{\mathrm{cor}}) \\ & - \int_{\Gamma^+_\square} \delta\mathbf{t}^{\mathrm{h}} \cdot [\![\mathbf{u}^{\mathrm{h}}]\!]_\square \,\mathrm{d}\,\Gamma + \int_{\Gamma^+_\square} \delta\mathbf{t}^{\mathrm{h}} \,\mathrm{d}\,\Gamma \cdot (\hat{\mathbf{u}}^+_{\mathrm{cor}} - \hat{\mathbf{u}}^-_{\mathrm{cor}}) = 0. \quad (3.27)\end{aligned}$$

Equation (3.27) is written in a format suitable for computer implementation:

$$\begin{aligned}\delta\hat{\mathbf{u}} \cdot \mathbf{K}_{\mathrm{uu}} \cdot \hat{\mathbf{u}} \mp \delta\hat{\mathbf{u}}^{\pm} \cdot \mathbf{K}^{\pm}_{\mathrm{ut}} \cdot \hat{\mathbf{t}} \pm \delta\hat{\mathbf{u}}^{\pm}_{\mathrm{cor}} \cdot \int_{\Gamma^+_\square} \mathbf{H} \,\mathrm{d}\,\Gamma \cdot \hat{\mathbf{t}} \mp \delta\hat{\mathbf{u}}^{\pm}_{\mathrm{cor}} \cdot \mathbf{f}^+_{\mathrm{cor}} \\ + \delta\hat{\mathbf{t}} \cdot \left\{ \mp \mathbf{K}^{\pm}_{\mathrm{tu}} \cdot \hat{\mathbf{u}}^{\pm} \pm \int_{\Gamma^+_\square} \mathbf{H}^\top \,\mathrm{d}\,\Gamma \cdot \hat{\mathbf{u}}^{\pm}_{\mathrm{cor}} \right\} = 0 \quad (3.28)\end{aligned}$$

Since (3.28) must hold for all $\delta\hat{\mathbf{u}} \in \mathbb{U}^{\mathrm{h}}_\square$ and $\delta\hat{\mathbf{t}} \in \mathbb{T}^{\mathrm{h}}_\square$, then it can be split into

$$\begin{aligned}\delta\hat{\mathbf{u}} \cdot \mathbf{K}_{\mathrm{uu}} \cdot \hat{\mathbf{u}} \mp \delta\hat{\mathbf{u}}^{\pm} \cdot \mathbf{K}^{\pm}_{\mathrm{ut}} \cdot \hat{\mathbf{t}} \pm \delta\hat{\mathbf{u}}^{\pm}_{\mathrm{cor}} \cdot \int_{\Gamma^+_\square} \mathbf{H} \,\mathrm{d}\,\Gamma \cdot \hat{\mathbf{t}} \mp \delta\hat{\mathbf{u}}^{+}_{\mathrm{cor}} \cdot \mathbf{f}^{\pm}_{\mathrm{cor}} = 0, \\ \mp \mathbf{K}^{\pm}_{\mathrm{tu}} \cdot \hat{\mathbf{u}}^{\pm} \pm \int_{\Gamma^+_\square} \mathbf{H}^\top \,\mathrm{d}\,\Gamma \cdot \hat{\mathbf{u}}^{\pm}_{\mathrm{cor}} = \mathbf{0}. \quad (3.29)\end{aligned}$$

When prescribing a force, $\hat{\mathbf{u}}_{\mathrm{cor}}$ must be solved for iteratively. Therefore, (3.29) is linearized by letting $\hat{\mathbf{u}} = \mathbf{u} + \Delta\mathbf{u}$, $\mathbf{t} = \mathbf{t} + \Delta\mathbf{t}$ and $\hat{\mathbf{u}}^{\pm}_{\mathrm{cor}} = \hat{\mathbf{u}}^{\pm}_{\mathrm{cor}} + \Delta\hat{\mathbf{u}}^{\pm}_{\mathrm{cor}}$:

$$\begin{aligned}\left\{ \delta\hat{\mathbf{u}} \cdot \mathbf{K}_{\mathrm{uu}} \cdot \Delta\hat{\mathbf{u}} \mp \delta\hat{\mathbf{u}}^{\pm} \cdot \mathbf{K}^{\pm}_{\mathrm{ut}} \cdot \Delta\hat{\mathbf{t}} \pm \delta\hat{\mathbf{u}}^{\pm}_{\mathrm{cor}} \cdot \int_{\Gamma^+_\square} \mathbf{H} \,\mathrm{d}\,\Gamma \cdot \Delta\hat{\mathbf{t}} \right\} = \pm\delta\hat{\mathbf{u}}^{\pm}_{\mathrm{cor}} \cdot \mathbf{f}^+_{\mathrm{cor}} \\ - \left\{ \delta\hat{\mathbf{u}} \cdot \int_{\Omega_\square} \mathbf{B}^\top \sigma(\hat{\mathbf{u}}) \,\mathrm{d}\,\Omega \mp \delta\hat{\mathbf{u}}^{\pm} \cdot \mathbf{K}^{\pm}_{\mathrm{ut}} \cdot \hat{\mathbf{t}} \pm \delta\hat{\mathbf{u}}^{\pm}_{\mathrm{cor}} \cdot \int_{\Gamma^+_\square} \mathbf{H} \,\mathrm{d}\,\Gamma \cdot \hat{\mathbf{t}} \right\}. \quad (3.30)\end{aligned}$$

and

$$\left\{ \mp \mathbf{K}^{\pm}_{\mathrm{tu}} \cdot \Delta\hat{\mathbf{u}}^{\pm} \pm \int_{\Gamma^+_\square} \mathbf{H}^\top \,\mathrm{d}\,\Gamma \cdot \Delta\hat{\mathbf{u}}^{\pm}_{\mathrm{cor}} \right\} = -\left\{ \mp \mathbf{K}^{\pm}_{\mathrm{tu}} \cdot \hat{\mathbf{u}}^{\pm} \pm \int_{\Gamma^+_\square} \mathbf{H}^\top \,\mathrm{d}\,\Gamma \cdot \hat{\mathbf{u}}^{\pm}_{\mathrm{cor}} \right\}. \quad (3.31)$$

The matrices $\mathbf{K}^{\pm}_{\mathrm{ut}}$ and $\mathbf{K}^{\pm}_{\mathrm{tu}}$ are defined in (3.10) and (3.13), respectively. Note that $\mathbf{f}^{\mathrm{t}}_{\mathrm{ext}}$ – given by (3.19) – is now included in $\mathbf{f}_{\mathrm{int}}$ because it is a function of the displacements at the corner nodes if the strain $(\bar{\mathbf{u}} \otimes \nabla)$ is not prescribed.

3.2 Jem-Jive Implementation

3.2.1 General Remarks

The nomenclature is adapted for computer implementation. To start with, corners 1, 2 and 4 are re-branded as *corner*-0, *corner*-x and *corner*-y. Similarly, the coordinate axes and boundary faces are re-numbered according to Fig. 3.2.

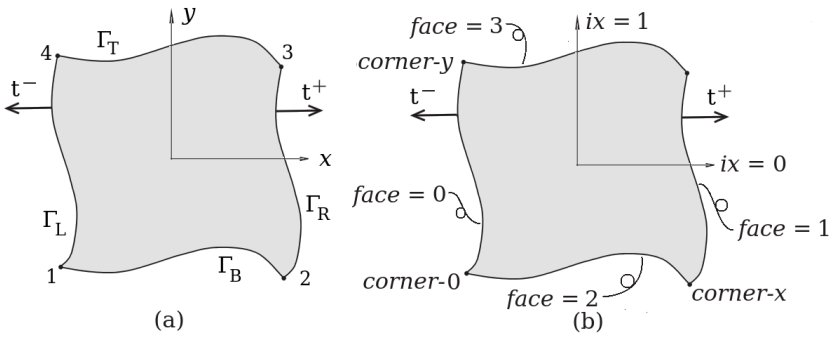

Figure 3.2: RVE: (a) mathematical notation; (b) FEM notation

The $\mathcal{U}^{\mathrm{h}}$ mesh is generated using gmsh 3.0 (Geuzaine and Remacle, 2018) with well defined boundary nodes. However, the center node $\bar{\mathbf{x}}$ may not have been specified. Thus, the current implementation has the following characteristics:

1. The RVE is centered around *corner*-0 instead of $\bar{\mathbf{x}}$. I.e., $\mathbf{u}'(\textit{corner}\text{-}0) = 0$.
2. Consequently, $\mathbf{u}_{\mathrm{M}} = \bar{\mathbf{u}} + (\bar{\mathbf{u}} \otimes \nabla) \cdot (\mathbf{x} - \textit{corner}\text{-}0)$, and thus $\mathbf{u}_{\mathrm{s}}(\textit{corner}\text{-}0) = 0$.
3. There is one vector per `face` containing the $\mathcal{U}^{\mathrm{h}}$ boundary node indices of that `face` in ascending order of x- or y-coordinates.
4. Each vector of $\mathcal{U}^{\mathrm{h}}$ node indices is stored in order of ascending `face` in a vector array called `bndNodes_`.
5. There is one vector per `ix` containing the $\mathcal{T}^{\mathrm{h}}$ node indices on the face perpendicular to `ix` (also in ascending order of x- or y-coordinates).
6. Each vector of $\mathcal{T}^{\mathrm{h}}$ node indices is stored in order of ascending `ix` in a vector array called `trNodes_`.

The first two points entail a different removal of rigid body motion, which does not alter the resulting stress distribution. On the other hand, fixing $\mathbf{u}(\textit{corner}\text{-}0)$ requires that the forcing vector prescribed by (3.19) become

$$\mathbf{f}^{\mathrm{t}}_{\mathrm{ext}} = -\begin{cases} \int_{\Gamma_{\mathrm{R}}} \mathbf{H}^{\top} \mathbf{u}(\textit{corner}\text{-}x)\, \mathrm{d}\,\Gamma \text{ on } \texttt{face} = 1 \\ \int_{\Gamma_{\mathrm{T}}} \mathbf{H}^{\top} \mathbf{u}(\textit{corner}\text{-}y)\, \mathrm{d}\,\Gamma \text{ on } \texttt{face} = 3 \end{cases}. \tag{3.32}$$

3.2.2 Program Structure

The weak micro-periodicity requirement is implemented using the Jem and Jive C++ libraries (Dynaflow Research Group, n.d.). Jem and Jive form a numerical toolkit for solving partial differential equations. Jive, in particular, provides many useful classes for building FEM-applications (such as classes for handling node sets, element sets, degrees of freedom and constraints). Besides these classes, Jive also provides an environment which divides programs into models and modules. Models are classes that implement a given aspect of an application (for example, defining loads, creating stiffness matrices or assigning constraints). Modules are classes that implement the solution algorithms: they read inputs and issue commands to the models in order to run the program. Decoupling programs into models and modules which must conform to abstract model and module classes facilitates the implementation and re-use of models and modules.

Module Class Definition

A module is an instance of a class derived from an abstract module class. This template prescribes three public methods: `init`, `run` and `shutdown`. The first two methods return an `enum` called `Status` with values: `OK`, `DONE` or `EXIT`.

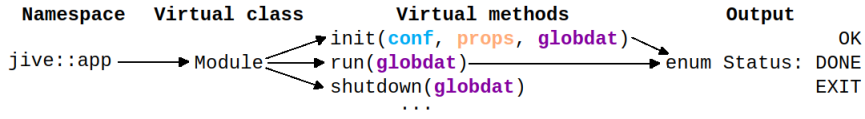

Figure 3.3: Jive module class definition

Typical Jive-based FEM applications require a properties file containing the parameters pertinent to the current analysis and the names of any other input files required by the program (e.g. mesh, load and constraints). This input file is first parsed by a Properties object called `props`. The modules can then be initialized using `props`. Each module contains a name used to find its runtime parameters in `props`. Modules read data from and write data to a previously initialized Properties object named `globdat`, which contains global data such as the model tree and the solution vector. Some typical Jive modules are:

- the InputModule, which constructs the mesh and stores it in `globdat`;
- the InitModule, which constructs a model tree and stores it in `globdat`;
- the LinsolveModule, which asks the model tree to assemble $\mathbf{K}_0$ and $\mathbf{f}_{\text{int}}$, runs a (specified) solver and stores the solution vector in `globdat`; and
- the OutputModule, which reads the solution vector and writes it to a file.

Another layer of abstraction is added by grouping a program's modules in a ChainModule, which is essentially a module that contains all necessary modules as children in the necessary order of execution. The modules are executed by

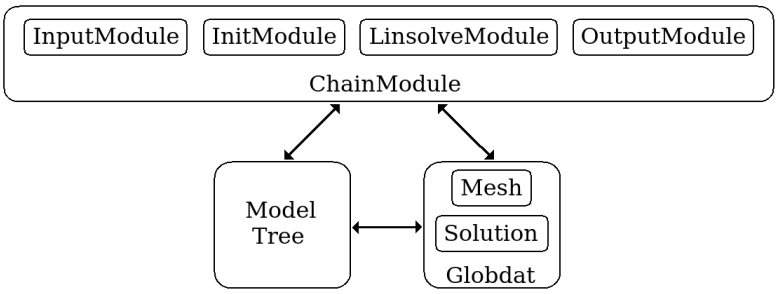

Figure 3.4: Example module chain

Jive's `Application::exec` function, which calls the `init`, `run` and `shutdown` methods of the ChainModule for as many times as needed to complete an analysis. In turn, the ChainModule calls the same methods from its children, discarding those which are `DONE`. `Application::exec` also handles output streams,

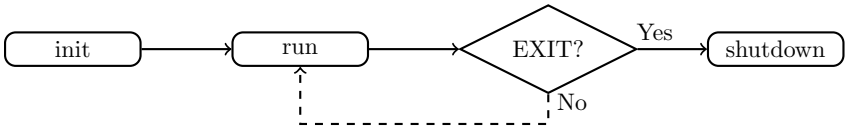

Figure 3.5: `Application::exec` flowchart

memory errors and any other exceptions thrown during execution. The modules issue commands to the models by calling a `takeAction` method implemented in every model. The modules pass a string specifying the action and a Properties object called `params` with the necessary parameters. Jive defines a collection of standard actions used by the built-in Jive modules (Fig 3.6). Weak microperiodicity is integrated into a program that performs these same actions.

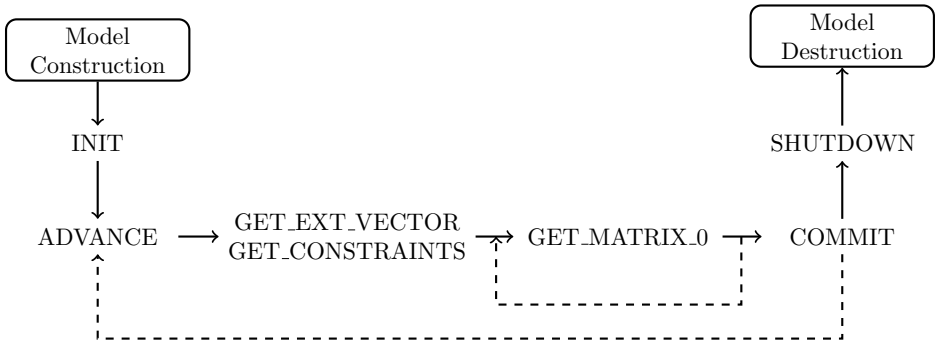

Figure 3.6: Standard actions flowchart

Model Class Definition

A model is an instance of a class derived from an abstract model class. Of the following four public methods: constructor, `configure`, `getConfig` and `takeAction`; at least the constructor and `takeAction` need to be implemented.

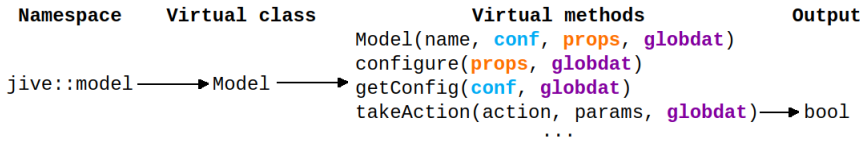

Figure 3.7: Jive model class definition

Models implement algorithms for computing the external and internal force vectors ($\mathbf{f}_{\text{ext}}$ and $\mathbf{f}_{\text{int}}$), the stiffness matrix ($\mathbf{K}_0$), and the constraints. When a module calls a models' `takeAction` method, the model executes the task and updates the parameters ($\mathbf{f}_{\text{ext}}$, $\mathbf{f}_{\text{int}}$, ...). If successful, `takeAction` returns `True`.

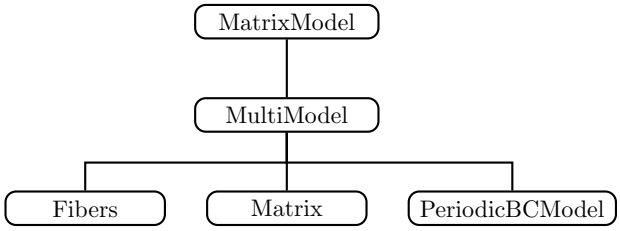

Figure 3.8: Example model tree

A single model need not perform all tasks. Instead, multiple models are usually combined into a model tree. Consider, for example, the subscale model with fibrous material surrounded by a matrix in Fig. 2.4(a). Its model tree comprises:

- the MatrixModel located at the root, which acts as a node with a single child and manages the MatrixBuilder object used to assemble $\mathbf{K}_0$;
- the MultiModel, which acts as a node with several child models – its `takeAction` method simply passing any commands onto its children;
- the Fibers and Matrix models, which return an updated $\mathbf{K}_0$ and $\mathbf{f}_{\text{int}}$ upon receiving the GET_MATRIX_0 command from the MultiModel; and
- the PeriodicBCModel, which returns an updated Constraints object upon receiving the GET_CONSTRAINTS command from the MultiModel.

This list (and thus Fig 3.8) is not comprehensive. Additional models may be required for applying external forces ($\mathbf{f}_{\text{ext}}$) or using solvers such as arc-length. In fact, corner forces are applied to the RVE in Fig. 4.5 using the DispArclenModel.

3.2.3 Weak Periodic Boundary Conditions Model

The weak periodic boundary conditions model (WeakPBCModel) is largely based on the strong periodic boundary conditions model (PeriodicBCModel) implemented by van der Meer (2016). Thus, the WeakPBCModel is implemented as a child of the PeriodicBCModel in order to access its member variables and private methods. It implements the following two public methods:

- The constructor of the WeakPBCModel calls the PeriodicBCModel constructor and instantiates the member variables in subsection 3.2.4.
- `takeAction` specifies which private methods are called based on the action issued by the ChainModule (and passed on by the parent model).

The following PeriodicBCModel private methods are called by `takeAction`:

- `advance_` scales the `imposedStrain_` when ADVANCE is issued.
- `fixCorner_` fixes *corner*-0 when GET_CONSTRAINTS is issued.
- `applyStrain_` imposes displacements on *corner*-x and *corner*-y (due to `imposedStrain_`) when GET_CONSTRAINTS is issued.
- `checkCommit_` checks and updates the solution when COMMIT is issued.

Additionally, the WeakPBCModel implements the following private methods:

- `init_` initializes all variables in subsection 3.3.4 when INIT is issued. It calls the following functions to initialize `bndNodes_`, `dx0_` and `trNodes_`:
  - `sortBndNodes_` sorts all vectors in `bndNodes_` by calling
    - `sortBndFace_` to sort each vector of node indices in `bndNodes_` in order of ascending x- or y-coordinates;
  - `findSmallestElement_` loops through all vectors in `bndNodes_` and assigns the smallest $\mathrm{d}\,x$ and $\mathrm{d}\,y$ between each pair of nodes to `dx0_`;
  - `createTractionMesh_` maps all nodes in `bndNodes_` onto $\Gamma^{+}_{\square}$, stores their indices in `trNodes_`, sorts them and coarsens them by calling
    - `sortBndFace_` to sort each vector in `trNodes_`, and
    - `coarsenMesh_` to delete nodes from each vector in `trNodes_`.
- `augmentMatrix_` performs the assembly procedure outlined in subsection 3.2.7 when GET_MATRIX_0 or GET_INT_VECTOR is issued and calls
  - `getTractionMeshNodes_` to obtain the pair of nodes in `trNodes_` that corresponds to (encapsulates) the current IP on the boundary of $\mathcal{U}^{\mathrm{h}}$.

3.2.4 Initialization

The model tree is constructed by the InitModule, which calls the constructor of the model type specified in `props`.[4] It then issues the INIT command to finish initializing the (instance) member variables of each model in the tree. For the PeriodicBCModel, these include:

- `rank_`: number of dimensions of the global topology
- `nodes_`: NodeSet for retrieving nodal coordinates
- `dofs_`: reference to the DofSpace object (table of degrees of freedom)
- `cons_`: reference to the Constraints object (table of constraints)
- `dofTypes_`: vector for retrieving dof indices from `dofs_`
- `bndNodes_`: array of vectors of $\mathcal{U}^{\mathrm{h}}$ boundary node indices
- `masters_`: vector of corner node indices (*corner*-x and *corner*-y)
- `ifixed_`: index of *corner*-0
- `imposedStrain_`: vector of applied strain rate
- `dx_`: vector of RVE dimensions

The WeakPBCModel adds the following member variables to this list:

- `nodes_`: XNodeSet to create the traction mesh nodes[5]
- `bshape_`: reference to BoundaryShape for calculating shape functions
- `nIP_`: number of integration points associated with `bshape_`
- `nnod_`: number of nodes associated with `bshape_`
- `ndof_`: number of dofs associated with `bshape_`
- `localrank_`: number of dimensions of the local topology of `bshape_`
- `trNodes_`: array of vectors of $\mathcal{T}^{\mathrm{h}}$ node indices
- `box_`: vector of specimen coordinates
- `dx0_`: vector of smallest element size along each axis
- `cf_`: coarsening factor

Most of these members are initialized by a private method called `init_` implemented in the WeakPBCModel, which calls subroutines for sorting the boundary nodes (`sortBndNodes_`), finding the smallest element (`findSmallestElement_`) and creating the traction mesh (`createTractionMesh_`).

[4] Each node of the model tree calls the constructor of its corresponding children.

[5] Extends the NodeSet `nodes_` into a XNodeSet to enable the creation of new nodes.

3.2.5 Sorting Boundary Nodes

The boundary nodes are sorted by `sortBndNodes_` and `sortBndFace_`. The first one passes on each vector in `bndNodes_` – together with an `index` – to the latter. In turn, `sortBndFace_` uses bubble sort to re-arrange the given vector of node indices in order of ascending x- or y-coordinates based on the given `index`.[6]

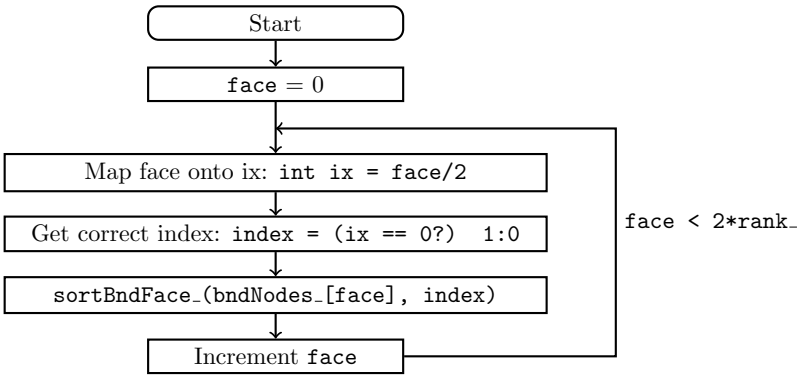

Figure 3.9: `sortBndNodes_()`

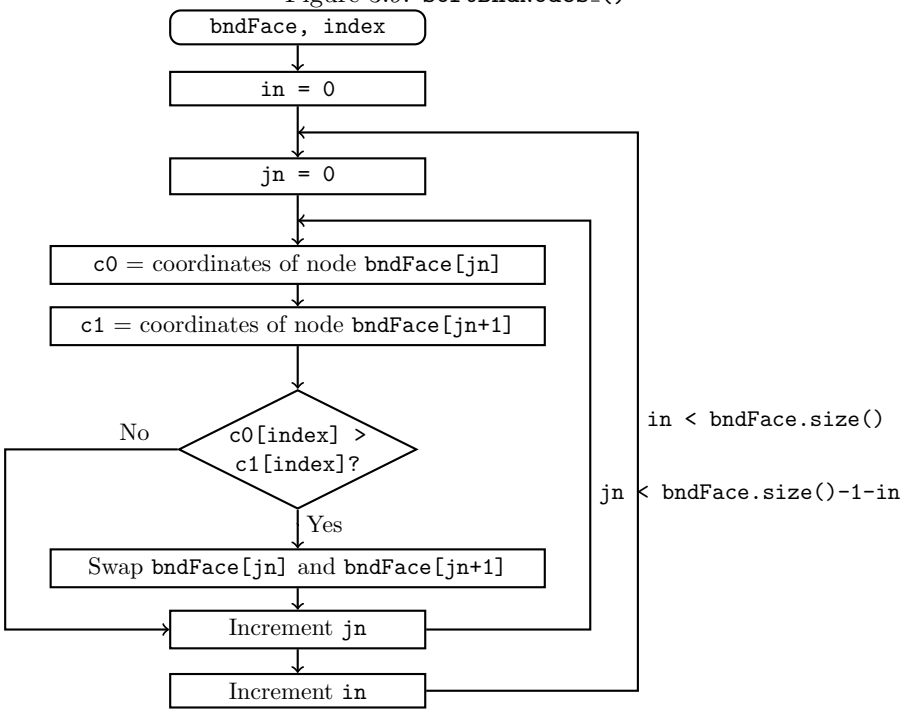

Figure 3.10: `sortBndFace_(bndFace, index)`

[6] `index` = 0 for x-coordinates and 1 for y-coordinates.

3.2.6 Traction Mesh Creation

The traction mesh is constructed per the procedure outlined in (Larsson et al., 2011, pp. 17–18). This procedure has the following steps:

1. `findSmallestElement_` loops through all vectors in `bndNodes_` and assigns the smallest (non-zero) $\mathrm{d}\,x$ and $\mathrm{d}\,y$ between each pair of nodes to `dx0_`.

2. `createTractionMesh_` projects all nodes from `bndNodes_` onto $\Gamma^{+}_{\square}$ and stores the indices of the new nodes in the corresponding vector in `trNodes_`.

3. It then sorts and coarsens (erases indices from) each vector in `trNodes_` by calling `sortBndFace_` (Fig. 3.10) and `coarsenMesh_` (Fig. 3.13).

The first two steps are illustrated in Fig. 3.11 and Fig. 3.12. The last step can be appreciated in Fig. 3.10 and Fig. 3.13.

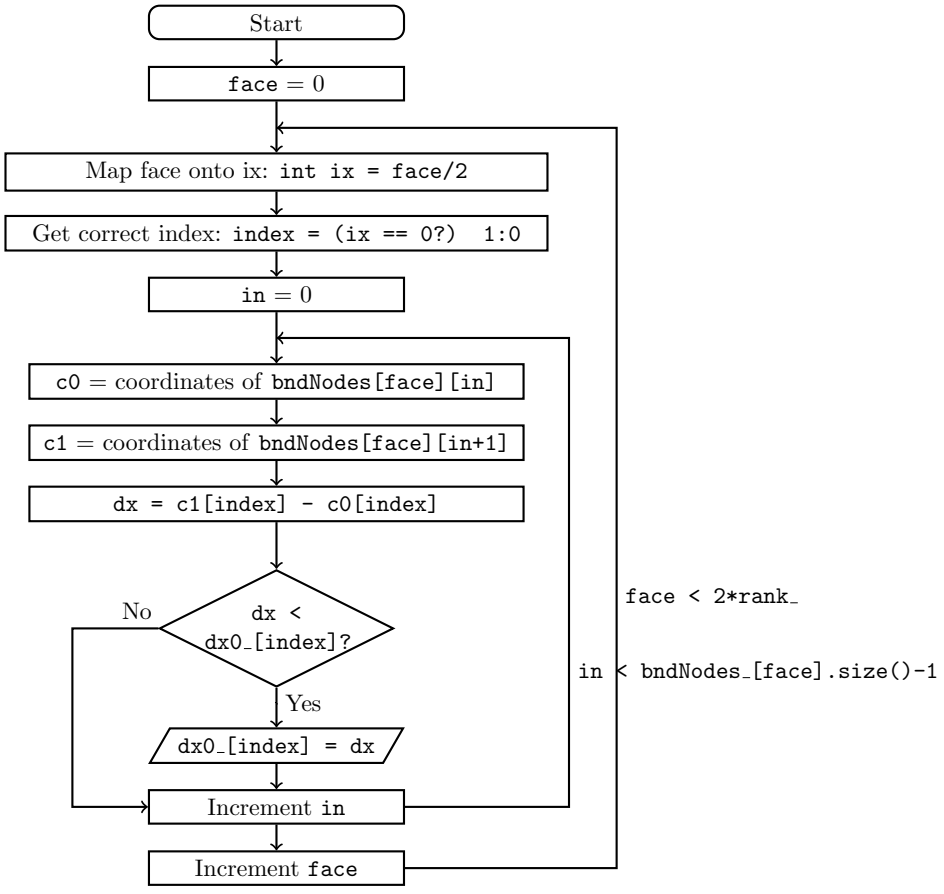

Figure 3.11: `findSmallestElement_()`

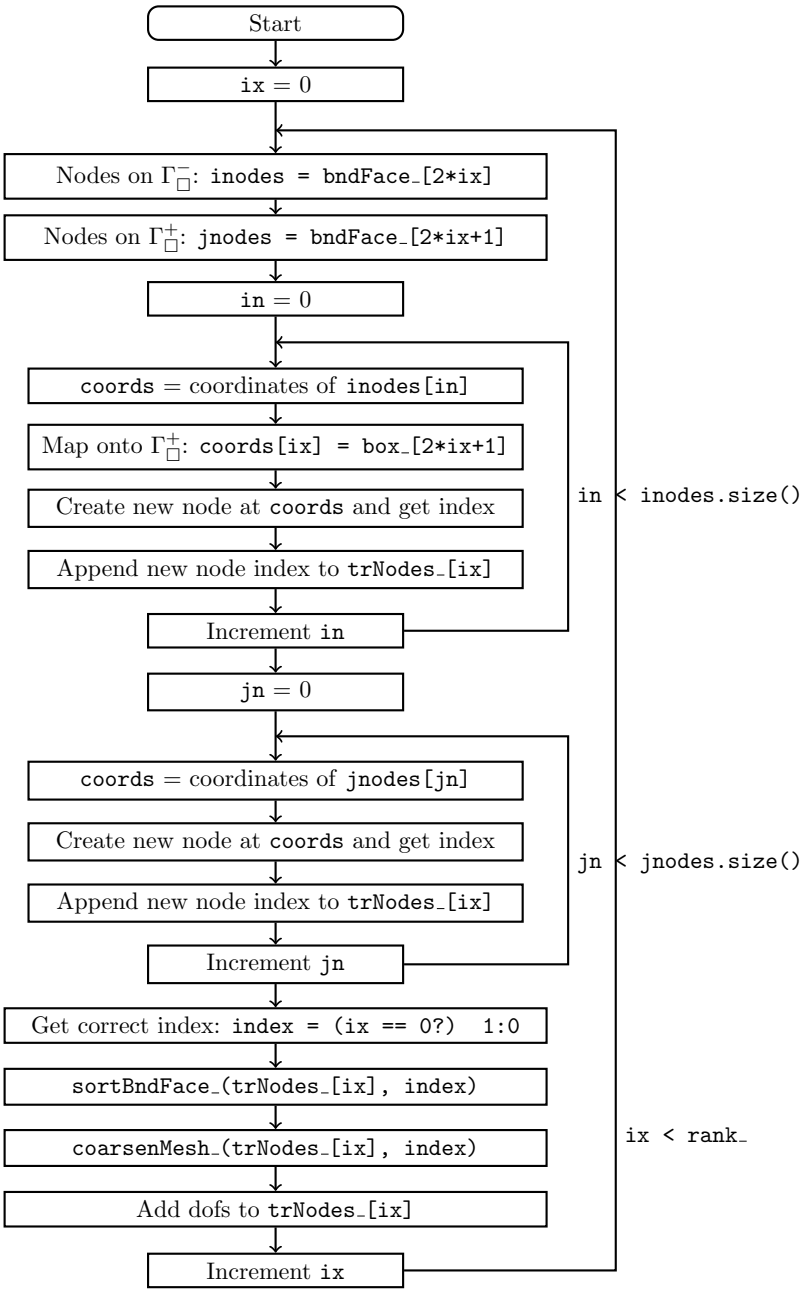

Figure 3.12: `createTractionMesh_()`

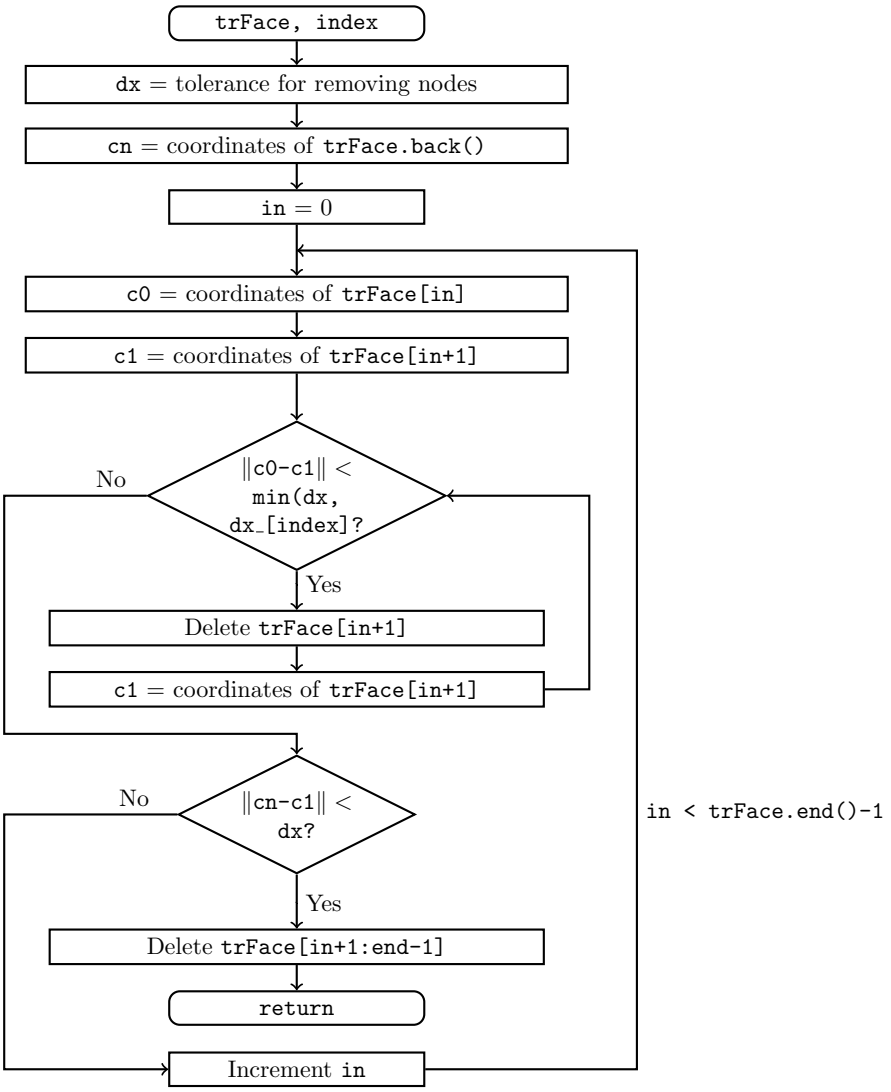

Figure 3.13: `coarsenMesh_(trFace, index)`

In Fig. 3.13, `dx` is set to `(dx0_[0] + dx0_[1])/2/cf_`.[7] Additionally, note that the while loop not only checks whether ‖`c0-c1`‖ is less than `dx` but also whether it is less than `dx_[index]` in case `dx` exceeds the RVE dimensions (`dx_`). The latter if-statement checks if the distance between `c1` and `cn` is less than `dx`. If it is, the leftover nodes except the last one are deleted and the function ends.[8]

[7] Instead of an average, it is possible to set `dx` to `dx0_[index]/cf_`, but this is less robust.
[8] Deleting the nodes is not necessary. It suffices to simply remove the indices from `trFace`.

3.2.7 Assembly Procedure

Lagrange multipliers are used to enforce the weak micro-periodicity constraint (3.31) on the finite element discretization of the equilibrium equation, such that $\Delta\mathbf{u}^{\mathrm{h}}$ and $\Delta\mathbf{t}^{\mathrm{h}}$ can be solved for simultaneously. The vectors $\hat{\mathbf{t}}$ and $\mathbf{f}^{\mathrm{t}}_{\mathrm{int}}$ are vertically appended to the solution vector $\hat{\mathbf{u}}$ and the internal force vector $\mathbf{f}_{\mathrm{int}}$ by a process called adjunction. Similarly, the matrices $\mathbf{K}^{\pm}_{\mathrm{ut}}$ and $\mathbf{K}^{\pm}_{\mathrm{tu}}$ are augmented to $\mathbf{K}_{\mathrm{uu}}$ to create $\mathbf{K}_0$. This assembly procedure is illustrated in equation (3.33):

$$\begin{bmatrix} \begin{bmatrix} & & \\ & \mathbf{K}_{\mathrm{uu}} & \\ & & \end{bmatrix} & \begin{bmatrix} \mathbf{0} \\ \mp\mathbf{K}^{\pm}_{\mathrm{ut}} \\ \pm\int_{\Gamma^{+}_{\square}} \mathbf{H}\,\mathrm{d}\,\Gamma \end{bmatrix} \\ \begin{bmatrix} \mathbf{0} & \mp\mathbf{K}^{\pm}_{\mathrm{tu}} & \pm\int_{\Gamma^{+}_{\square}} \mathbf{H}^{\top}\,\mathrm{d}\,\Gamma \end{bmatrix} & \begin{bmatrix} \mathbf{0} \end{bmatrix} \end{bmatrix} \begin{Bmatrix} \Delta\hat{\mathbf{u}}^{\mathrm{int}} \\ \Delta\hat{\mathbf{u}}^{\pm} \\ \Delta\hat{\mathbf{u}}^{\pm}_{\mathrm{cor}} \\ \Delta\hat{\mathbf{t}} \end{Bmatrix} = -\begin{Bmatrix} \left\{ \int_{\Omega_{\square}} \mathbf{B}^{\top}\sigma\,\mathrm{d}\,\Omega \right\} + \begin{Bmatrix} \mathbf{0} \\ \mp\mathbf{K}^{\pm}_{\mathrm{ut}}\hat{\mathbf{t}} \\ \pm\int_{\Gamma^{+}_{\square}} \mathbf{H}\,\mathrm{d}\,\Gamma\hat{\mathbf{t}} \end{Bmatrix} \\ \left\{ \mp\mathbf{K}^{+}_{\mathrm{tu}}\hat{\mathbf{u}}^{\pm} \pm\int_{\Gamma^{+}_{\square}} \mathbf{H}^{\top}\,\mathrm{d}\,\Gamma\hat{\mathbf{u}}^{\pm}_{\mathrm{cor}} \right\} \end{Bmatrix} \tag{3.33}$$

$\mathbf{K}_{\mathrm{uu}}$ is assembled as usual by one or more SolidModels representing each of the RVE materials (c.f. Fibers and Matrix in Fig. 3.8). For non-periodic meshes, elements on $\mathcal{T}^{\mathrm{h}}$ may not fully overlap the elements on the boundary of $\mathcal{U}^{\mathrm{h}}$:

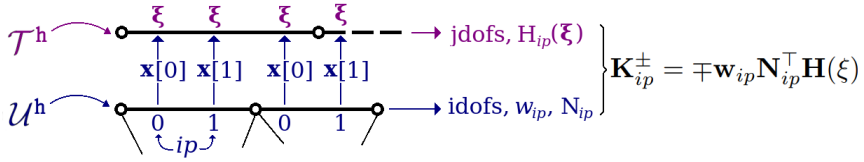

Figure 3.14: Contribution of each IP towards $\mathbf{K}^{\pm}_{\mathrm{ut}}$

Therefore, the contributions to $\mathbf{K}^{\pm}_{\mathrm{ut}}$ (3.10) and ${\mathbf{K}^{\pm}_{\mathrm{ut}}}^{\top}$ (3.13) are evaluated and added to $\mathbf{K}_0$ at each IP (instead of element) on the boundary of $\mathcal{U}^{\mathrm{h}}$ per [9]

$$\begin{aligned} \mathbf{K}_0[\mathtt{idofs},\mathtt{jdofs}] &= \mathbf{K}_0[\mathtt{idofs},\mathtt{jdofs}] + \mathbf{K}^{\pm}_{ip}, \\ \mathbf{K}_0[\mathtt{jdofs},\mathtt{idofs}] &= \mathbf{K}_0[\mathtt{jdofs},\mathtt{idofs}] + {\mathbf{K}^{\pm}_{ip}}^{\top}, \end{aligned} \tag{3.34}$$

where the contribution from each IP towards $\mathbf{K}^{\pm}_{\mathrm{ut}}$ is given by

$$\mathbf{K}^{\pm}_{ip} = \mp\mathbf{w}_{ip}\mathbf{N}^{\top}_{ip}\mathbf{H}(\xi). \tag{3.35}$$

$\mathbf{K}^{+}_{ip}$ corresponds to $\Gamma^{+}_{\square}$ (faces 1 and 3) and $\mathbf{K}^{-}_{ip}$, to $\Gamma^{-}_{\square}$ (faces 0 and 2). `idofs` and `jdofs` are the vectors of degrees of freedom associated with the current elements in $\mathcal{U}^{\mathrm{h}}$ and $\mathcal{T}^{\mathrm{h}}$, respectively. In turn, $\mathbf{N}_{ip}$ and $\mathbf{H}(\xi)$ are the matrices

[9] The integration is done over the boundary of $\mathcal{U}^{\mathrm{h}}$ because it has a finer mesh than $\mathcal{T}^{\mathrm{h}}$.

of shape functions evaluated at each IP on the boundary of $\mathcal{U}^\mathrm{h}$ and the local coordinate ξ of the corresponding element in $\mathcal{T}^\mathrm{h}$. $\mathbf{w}_{ip}$ is the Gaussian weight times the jacobian at the same IP. The contributions to $\mathbf{f}_\mathrm{int}$ are added similarly:

$$\begin{aligned}\mathbf{f}_\mathrm{int}[\texttt{idofs}] &= \mathbf{f}_\mathrm{int}[\texttt{idofs}] + \mathbf{K}_{ip}^{\pm} \cdot \hat{\mathbf{t}}[\texttt{jdofs}],\\ \mathbf{f}_\mathrm{int}[\texttt{jdofs}] &= \mathbf{f}_\mathrm{int}[\texttt{jdofs}] + \mathbf{K}_{ip}^{\pm\,\top} \cdot \hat{\mathbf{u}}[\texttt{idofs}].\end{aligned} \tag{3.36}$$

Thereafter, the contributions to $\int_{\Gamma_\square^+} \mathbf{H}\,\mathrm{d}\,\Gamma$ and $\int_{\Gamma_\square^+} \mathbf{H}^\top\,\mathrm{d}\,\Gamma$ are added to $\mathbf{K}_0$ per

$$\begin{aligned}\mathbf{K}_0[\texttt{idofs},\texttt{jdofs}] &= \mathbf{K}_0[\texttt{idofs},\texttt{jdofs}] + \mathbf{w}_{ip}\mathbf{H}_{ip}.\\ \mathbf{K}_0[\texttt{jdofs},\texttt{idofs}] &= \mathbf{K}_0[\texttt{jdofs},\texttt{idofs}] + \mathbf{w}_{ip}\mathbf{H}_{ip}^\top,\\ \mathbf{K}_0[\texttt{kdofs},\texttt{jdofs}] &= \mathbf{K}_0[\texttt{kdofs},\texttt{jdofs}] - \mathbf{w}_{ip}\mathbf{H}_{ip},\\ \mathbf{K}_0[\texttt{jdofs},\texttt{kdofs}] &= \mathbf{K}_0[\texttt{jdofs},\texttt{kdofs}] - \mathbf{w}_{ip}\mathbf{H}_{ip}^\top.\end{aligned} \tag{3.37}$$

The integration is done over $\mathcal{T}^\mathrm{h}$ because the integrand stems entirely from $\mathbb{T}^\mathrm{h}$. Here, $\mathbf{H}_{ip}$ is the matrix of shape functions at each IP of $\mathcal{T}^\mathrm{h}$ and $\mathbf{w}_{ip}$ is its corresponding integration weight. `jdofs` is the vectors of degrees of freedom associated with the current element on $\mathcal{T}^\mathrm{h}$ while `idofs` and `kdofs` correspond to the corners of $\mathcal{U}^\mathrm{h}$. The contributions to $\mathbf{f}_\mathrm{int}$ are added in a similar manner:

$$\begin{aligned}\mathbf{f}_\mathrm{int}[\texttt{idofs}] &= \mathbf{f}_\mathrm{int}[\texttt{idofs}] + \mathbf{w}_{ip}\mathbf{H}_{ip} \cdot \hat{\mathbf{t}}[\texttt{jdofs}],\\ \mathbf{f}_\mathrm{int}[\texttt{kdofs}] &= \mathbf{f}_\mathrm{int}[\texttt{kdofs}] - \mathbf{w}_{ip}\mathbf{H}_{ip} \cdot \hat{\mathbf{t}}[\texttt{jdofs}],\\ \mathbf{f}_\mathrm{int}[\texttt{jdofs}] &= \mathbf{f}_\mathrm{int}[\texttt{jdofs}] \pm \mathbf{w}_{ip}\mathbf{H}_{ip}^\top \cdot \hat{\mathbf{u}}_\texttt{cor}^{\pm},\end{aligned} \tag{3.38}$$

where $\hat{\mathbf{u}}_\mathrm{cor}^{+} = \hat{\mathbf{u}}[\texttt{idofs}]$ and $\hat{\mathbf{u}}_\mathrm{cor}^{-} = \hat{\mathbf{u}}[\texttt{kdofs}]$. The last two equations from (3.37) may be omitted when $\hat{\mathbf{u}}_\mathrm{cor}^{-} = \Delta\hat{\mathbf{u}}_\mathrm{cor}^{-} = 0$; however, it is sensible to keep all terms from (3.37) and (3.38) to ensure consistency (correctness) between $\mathbf{f}_\mathrm{int}$ and $\mathbf{K}_0$.

Chapter 4

MODEL VALIDATION

The validity of the WeakPBCModel is corroborated by means of linear-elastic and materially nonlinear analyses. Of these, the linear-elastic tests are executed on an elastic material and a fiber-matrix composite, both in plane strain condition with unit thickness. The nonlinear tests are also executed on the fiber-matrix composite with elastic fibers but an elasto-plastic matrix instead.

4.1 Linear-Elastic Analyses

4.1.1 Linear-Elastic Material in Plane Strain Condition

The linear-elastic material is tested under axial and shear loading by means of (a) prescribed strain and (b) applied load on the south-east corner of the mesh (*corner-x*). The axial test results are compared to the expected analytical results. Consider the compliance matrix in 4.1:

$$\begin{Bmatrix} \varepsilon_{\mathrm{xx}} \\ \varepsilon_{\mathrm{yy}} \\ \varepsilon_{\mathrm{zz}} \end{Bmatrix} = \frac{1}{E} \begin{bmatrix} 1 & -\nu & -\nu \\ -\nu & 1 & -\nu \\ -\nu & -\nu & 1 \end{bmatrix} \begin{Bmatrix} \sigma_{\mathrm{xx}} \\ \sigma_{\mathrm{yy}} \\ \sigma_{\mathrm{zz}} \end{Bmatrix}. \tag{4.1}$$

Letting $\varepsilon_{\mathrm{zz}} = \sigma_{\mathrm{yy}} = 0$, the following three equations are derived:

$$\varepsilon_{\mathrm{xx}} = \frac{\sigma_{\mathrm{xx}}}{E} - \frac{\nu\sigma_{\mathrm{zz}}}{E}, \tag{4.2}$$

$$\varepsilon_{\mathrm{yy}} = -\frac{\nu\sigma_{\mathrm{xx}}}{E} - \frac{\nu\sigma_{\mathrm{zz}}}{E}, \tag{4.3}$$

$$0 = -\frac{\nu\sigma_{\mathrm{xx}}}{E} + \frac{\sigma_{\mathrm{zz}}}{E} \xrightarrow{\text{yields}} \sigma_{\mathrm{zz}} = \nu\sigma_{\mathrm{xx}}. \tag{4.4}$$

In turn, substituting (4.4) into (4.3) and (4.2) yields the following two results:

$$sigma_{\mathrm{xx}} = \frac{E}{1-\nu^2}\varepsilon_{\mathrm{xx}} \xrightarrow{\text{yields}} \frac{\sigma_{\mathrm{xx}}}{\varepsilon_{\mathrm{xx}}} = \frac{E}{1-\nu^2}, \tag{4.5}$$

$$\varepsilon_{\mathrm{yy}} = \frac{-\nu-\nu^2}{E}\sigma_{\mathrm{xx}} \xrightarrow{\text{yields}} \frac{\varepsilon_{\mathrm{yy}}}{\varepsilon_{\mathrm{xx}}} = \frac{-\nu-\nu^2}{1-\nu^2}. \tag{4.6}$$

Now, consider the RVE shown in Fig. 4.1. The width and height are the same ($\Delta x = \Delta y$). The Young's modulus is 910 and the Poisson's ratio is 0.3. An

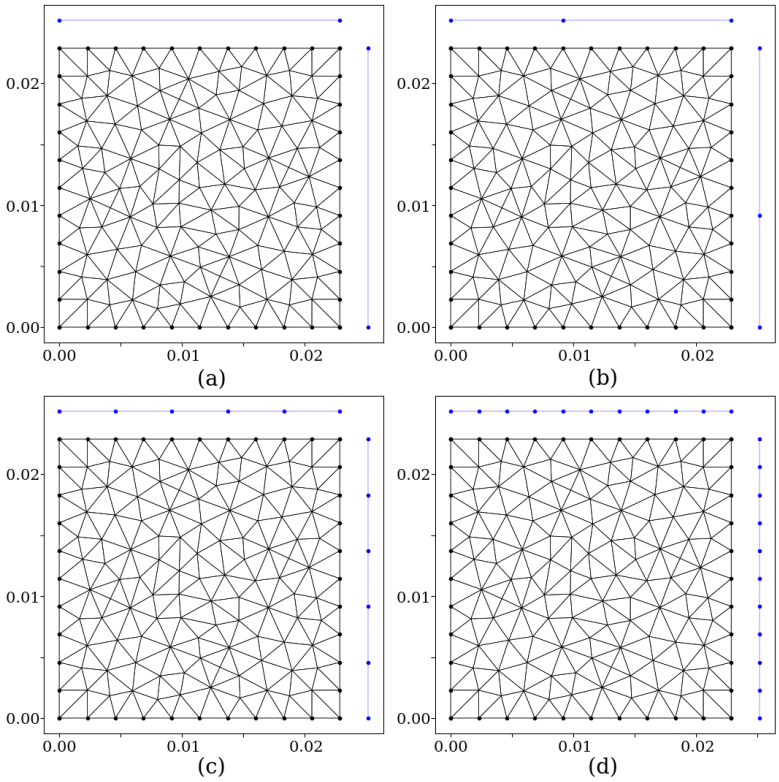

Figure 4.1: Linear-elastic material. Traction mesh with `cf_` = (a) 0.1; (b) 0.3; (c) 0.6; (d) 1.0

axial test under plane strain condition yields the following effective stiffness:

$$(EA)_{\text{plane}} = \frac{f}{u} = \frac{\sigma_{\text{xx}} t \Delta y}{\varepsilon_{\text{xx}} \Delta x} = \frac{Et}{1-\nu^2} = 1000. \tag{4.7}$$

The WeakPBCModel results are compared against the PeriodicBCModel results via plots of stiffness vs. coarsening factors (`cf_`). The axial stiffness is estimated as the horizontal force-to-displacement ratio at *corner-x*, in accordance to (4.7). The shear stiffness is estimated as the vertical force at *corner-x* divided by the total distance traversed by *corner-x* and *corner-y*. In turn, `cf_` sets the minimum element size for the traction mesh $\mathcal{T}^{\text{h}}$. Fig. 4.2 shows good agreement between the PeriodicBCModel and WeakPBCModel under prescribed axial strain[1] and applied horizontal force on *corner-x*. Fig. 4.3 shows acceptable agreement for prescribed shear strain and applied vertical force.

[1]Note that ε_{yy} is prescribed per (4.6) to ensure $\sigma_{\text{yy}} = 0$

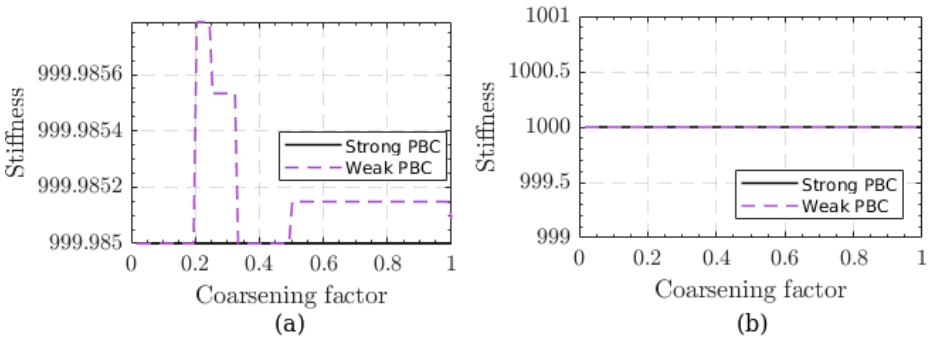

Figure 4.2: Linear-elastic: (a) axial strain = $\langle 0.1, -0.04286, 0.0 \rangle$; (b) horizontal force on *corner-x*

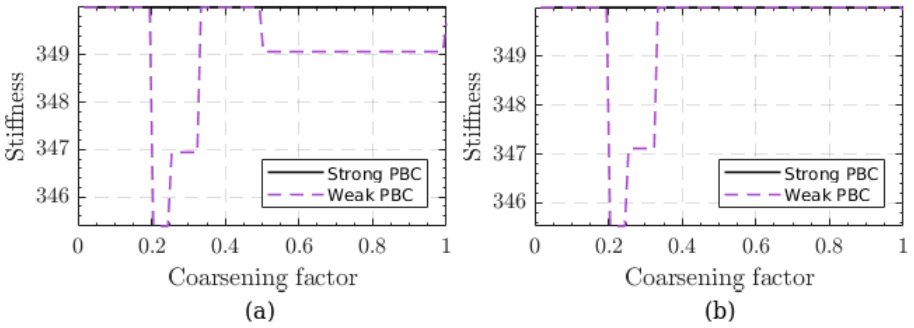

Figure 4.3: Linear-elastic: (a) shear strain = $\langle 0.0, 0.0, 0.1 \rangle$; (b) vertical force on *corner-x*

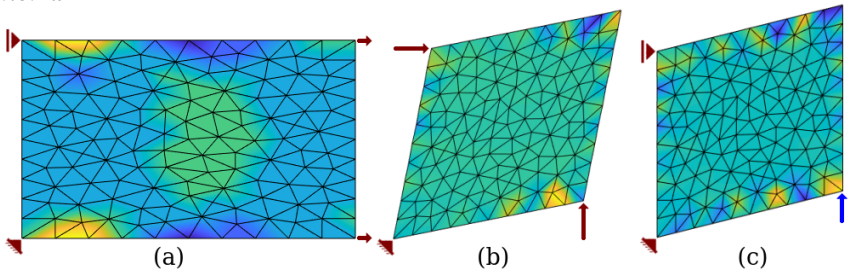

Figure 4.4: Deformation: (a) axial strain; (b) shear strain; (c) vertical force

Overall, there is satisfactory agreement between the WeakPBCModel and the PeriodicBCModel under axial deformation (Fig. 4.2) and shear deformation (Fig. 4.3). Some values of `cf_` give rise to small discrepancies between both models, but in general the stiffness remains fairly constant. This is reflected in the lack of strain localization in the deformed geometry (Fig. 4.4).

4.1.2 Fiber-Matrix Composite

The fiber-matrix composite in Fig. 4.5 is also tested under axial and shear loading by means of (a) prescribed strain and (b) applied load on *corner-x*. The

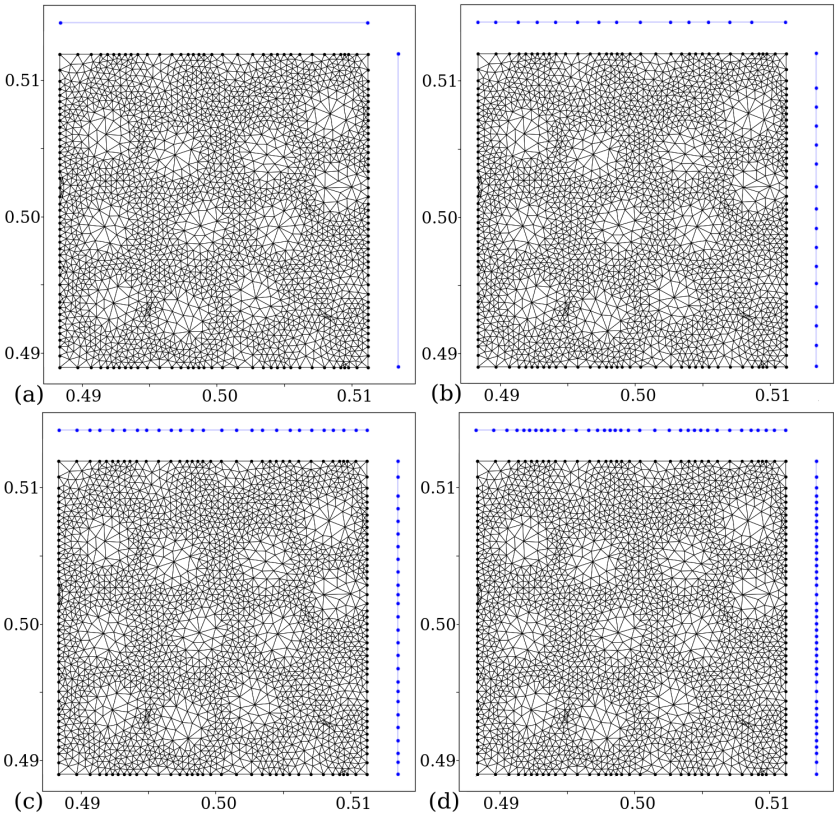

Figure 4.5: Fiber-matrix composite. Traction mesh with `cf_` = (a) 0.01592; (b) 0.3; (c) 0.6; (d) 1.0

matrix material has a Young's modulus of 3760 and a Poisson's ratio of 0.3. The fibers have a Young's modulus of 74000 and a Poisson's ratio of 0.2. Fig. 4.6 shows good agreement between the WeakPBCModel and the PeriodicBCModel under prescribed axial strain and applied horizontal force on *corner-x*. Likewise, Fig. 4.7 shows good agreement between the models under prescribed shear strain and applied vertical force on *corner-x*. As expected, the Neumann traction mesh (`cf_` = 0.01592) produced the softest result. The results become stiffer with finer traction meshes until `cf_` = 0.3 is surpassed. The deformed geometries are presented for these two coarsening factors: 0.01592 and 0.3. Non-periodic deformation is barely visible with finer traction meshes, which supports the close agreement between the WeakPBCModel and the PeriodicBCModel.

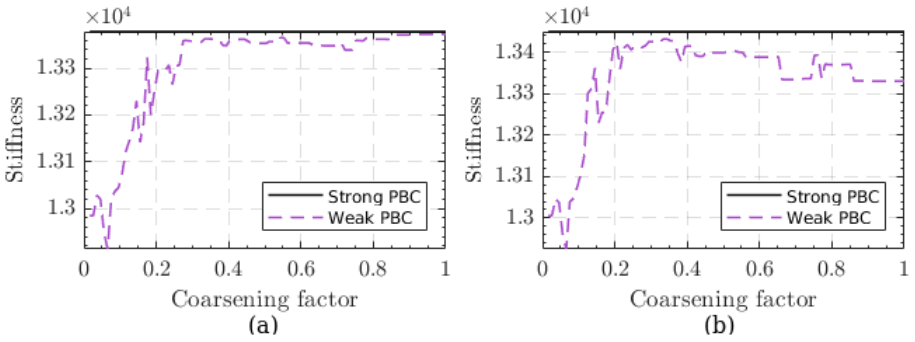

Figure 4.6: Fiber-matrix: (a) axial strain = $\langle 0.1, -0.03404, 0.0 \rangle$; (b) horizontal force on *corner-x*

Here, the ε_{yy} component for the prescribed axial strain is not known a-priori as with the linear-elastic material in plane strain condition. Instead, a horizontal force was first applied on *corner-x* using the PeriodicBCModel. The vertical deflection at *corner-y* was then used to derive the value needed for ε_{yy}.

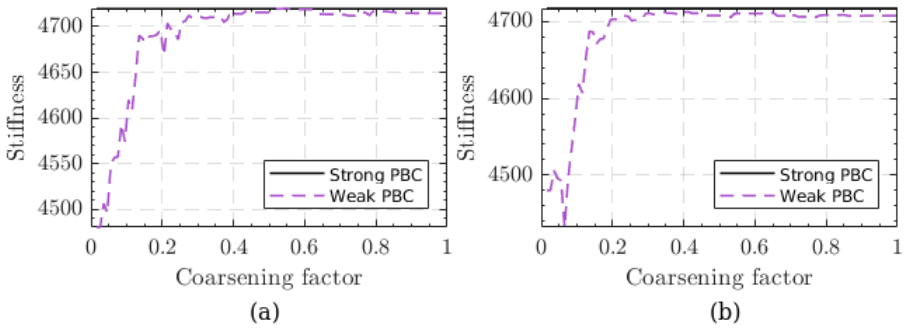

Figure 4.7: Fiber-matrix: (a) shear strain = $\langle 0, 0, 0.1 \rangle$; (b) vertical force on *corner-x*

These results show good agreement between the WeakPBCModel and PeriodicBCModel under axial deformation (Fig. 4.6) and shear deformation (Fig. 4.7). It is noted that the stiffness increases steeply at low coarsening factors but remains fairly constant after `cf_` = 0.3. Fig. 4.1 and Fig. 4.5 show that – at any given `cf_` – coarser $\mathcal{U}^{\mathrm{h}}$ yield less number of elements per face of $\mathcal{T}^{\mathrm{h}}$. Less elements in $\mathcal{T}^{\mathrm{h}}$ results in a weaker periodicity constraint and a lower stiffness. Thus, a coarser $\mathcal{U}^{\mathrm{h}}$ should produce a more gradual increase in the stiffness.

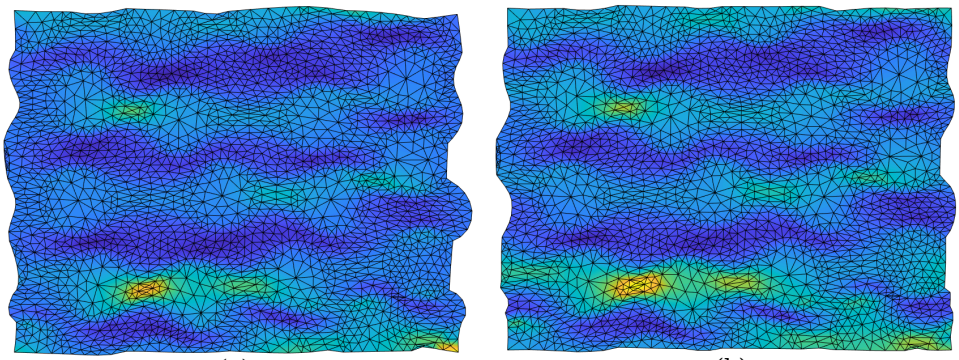

Figure 4.8: Deformation due to axial strain: (a) `cf_` = 0.01592; (b) `cf_` = 0.3

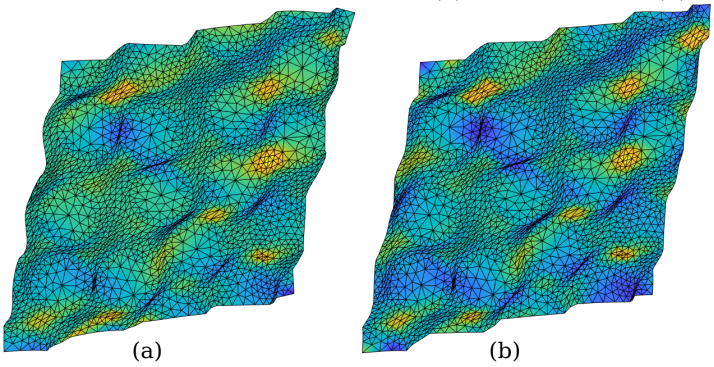

Figure 4.9: Deformation due to shear strain: (a) `cf_` = 0.01592; (b) `cf_` = 0.3

The low stiffnesses towards `cf_` = 0.01592 agree with the non-periodic deformation in Fig. 4.6 and Fig. 4.7. Au contraire, the deformed geometry seems to abide periodicity of displacements for coarsening factors higher than 0.3.

4.2 Materially Nonlinear Analyses

Consider the fiber-matrix composite in Fig. 4.5. The matrix is now modeled as an elastic-perfectly plastic material with non-associative flow rule based on (Melro et. al, 2013). Its Young's modulus and Poisson's ratio remain 3760 and 0.3. The plastic Poisson's ratio and yield stress are 0.39 and 80. Setting the same yield stress for tension and compression, the Von Mises yield surface is recovered.

4.2.1 Prescribed Strain

Instead of stiffness-coarsening plots, force-displacement curves are presented to compare coarsening factors in the materially nonlinear analyses. The next results were obtained using an AdaptiveStepModule and SkylineLU solver with precision $= 1 \cdot 10^{-4}$ and up to 20 iterations per step (maxIter = 20).

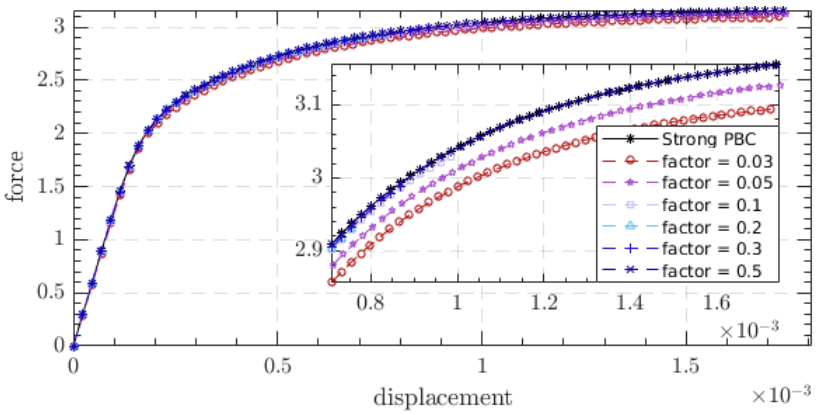

Figure 4.10: Fiber-matrix composite with strain rate $= \langle 0.001, -0.000429, 0.0 \rangle$

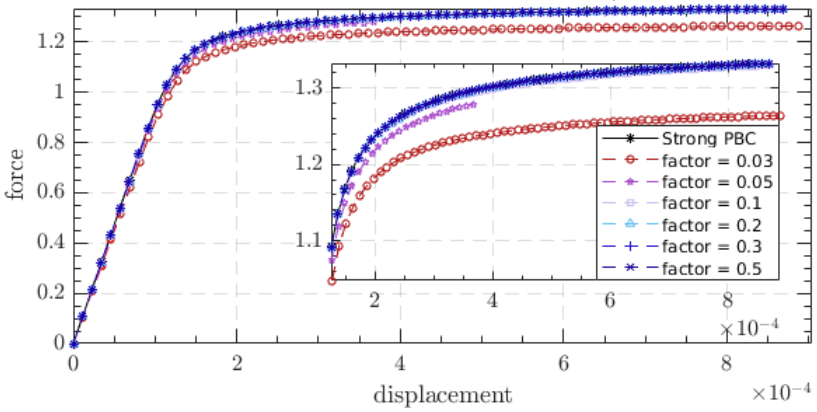

Figure 4.11: Fiber-matrix composite with strain rate $= \langle 0.0, 0.0, 0.001 \rangle$

These results show good agreement between the models under prescribed axial strain (Fig. 4.10) and prescribed shear strain (Fig. 4.11). As expected, the coarser traction meshes produce the softest results. These become stiffer until `cf_` $= 0.3$ is surpassed, at which point there is very little difference between the results from the WeakPBCModel and the PeriodicBCModel.

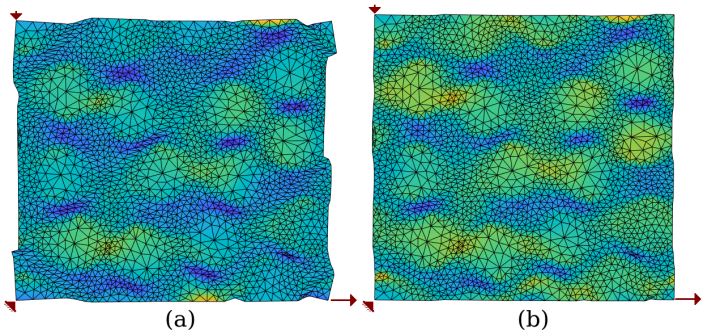

Figure 4.12: Deformation due to axial strain: (a) `cf_` = 0.01582; (b) `cf_` = 0.3

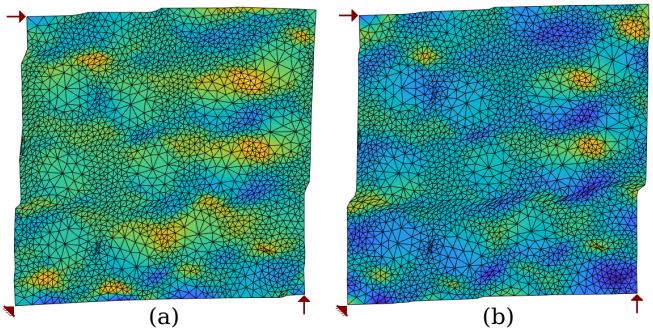

Figure 4.13: Deformation due to shear strain: (a) `cf_` = 0.01582; (b) `cf_` = 0.3

The soft results for the Neumann traction mesh are in agreement with the non-periodic strain localization in Fig. 4.12(a) and Fig. 4.13(a). On the other hand, the deformed geometry seems to abide periodicity of displacements for values of `cf_` higher than 0.3, which substantiates the close agreement between the WeakPBCModel and the PeriodicBCModel in the force-displacement plots.

4.2.2 Prescribed Force

Here, 300 steps of size 0.1 were used in tandem with the FlexArclenModule and SkylineLU solver (precision = $1 \cdot 10^{-4}$ and maxIter = 10). The results not only resemble the prescribed strain results, but also agree with the PeriodicBCModel. Again, the WeakPBCModel results become stiffer until `cf_` = 0.3 is surpassed, whereon they are almost indistinguishable from the PeriodicBCModel results.

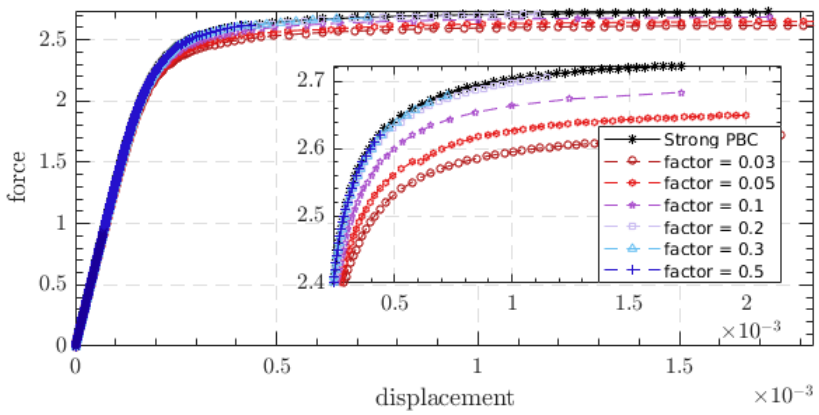

Figure 4.14: Fiber-matrix composite with horizontal force on *corner-x*

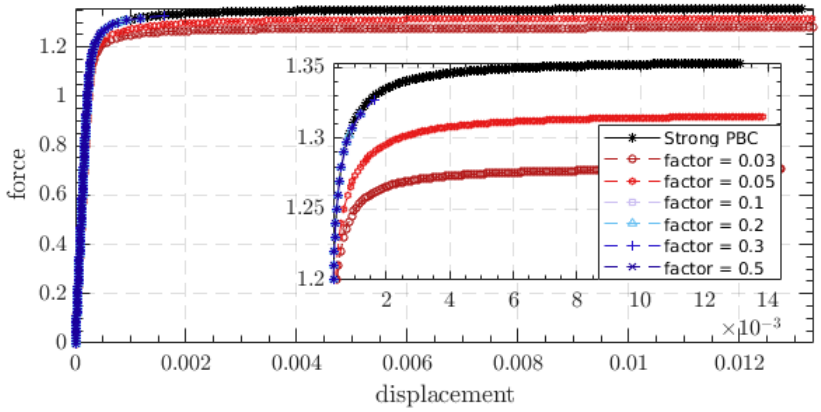

Figure 4.15: Fiber-matrix composite with vertical force on *corner-x*

The deformed geometries show non-periodic strain localization for a coarsening factor of 0.01592 and almost purely periodic strain localization for coarsening factors higher than 0.3. Again, this agrees with the force-displacement plots.

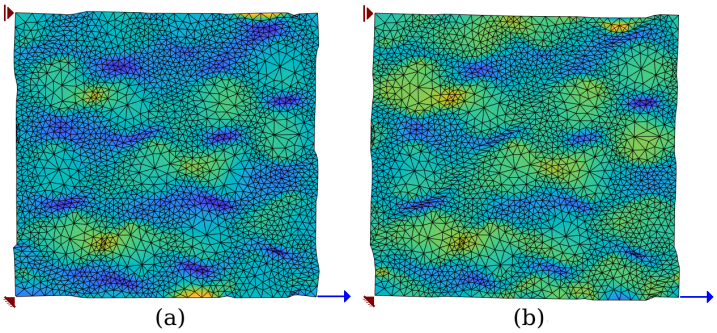

Figure 4.16: Deformation due to horizontal force. (a) `cf_` = 0.01582; (b) `cf_` = 0.3

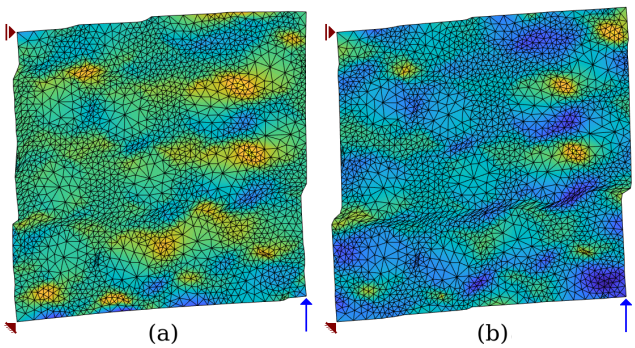

Figure 4.17: Deformation due to vertical force. (a) `cf_` = 0.01582; (b) `cf_` = 0.3

Chapter 5

METHODOLOGY

The thesis statement is tested on a batch of fiber-matrix composite RVEs.[1] Uniaxial load is applied to each RVE at 46 different angles between 0^o and 90^o to generate a curve of ultimate principal stress (σ_1) vs. orientation angle (θ). The ultimate stresses are averaged to produce one characteristic $\bar{\sigma}_1$–θ curve. This process is executed with 10 coarsening factors (`cf_`) and 3 load steps ($|\mathbf{f}|$), which culminates in a total of 30 $\bar{\sigma}_1$–θ curves. Fig 5.1 summarizes this procedure.

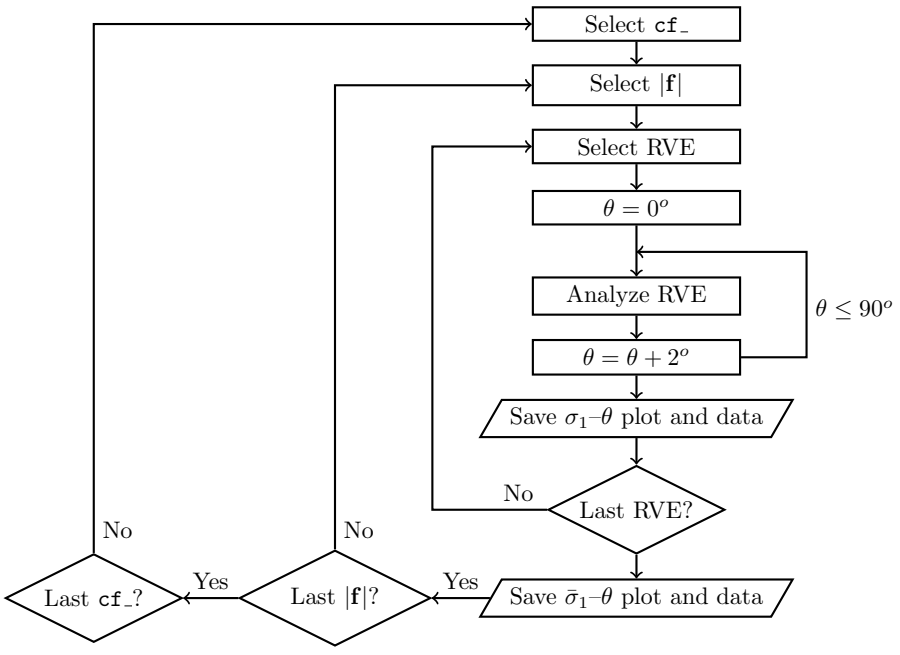

Figure 5.1: Methodology

[1] Multiple RVEs are required to overcome bias from each individual geometry.

5.1 Principal Stress vs. Orientation Angle

Unlike periodic boundary conditions, the weak periodic boundary conditions formulated in (Larsson et al., 2011) can only be used in deformation-driven procedures. Yet, to corroborate the thesis statement, one should prescribe a uniaxial stress on each RVE.[2] The setup introduced in subsection 3.1.2 grants the application of external forces on the RVE corners to represent stress. Hereinafter, the process by which the load is rotated and the resulting principal stresses are retrieved is delineated. The uniaxial load is applied along the x'-axis and transformed into the RVE coordinates. The x'-axis rotates counter-clockwise.

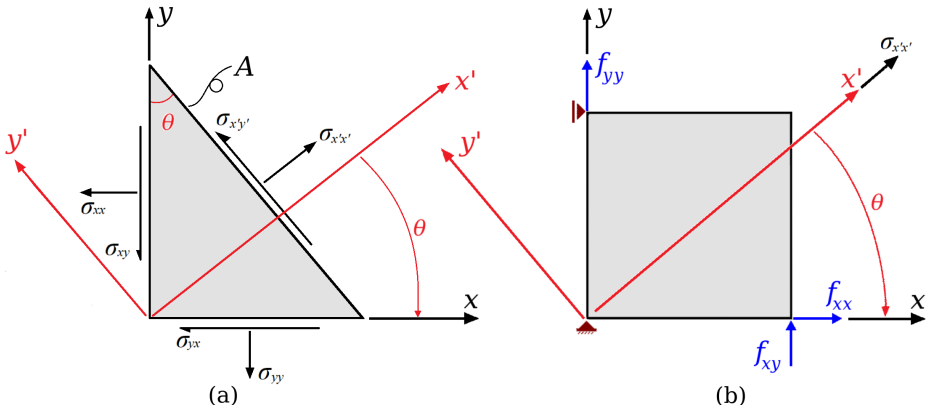

Figure 5.2: (a) Stress transformation; (b) corner forces

Consider the stress transformation in Fig. 5.2. The second order stress tensor $\boldsymbol{\Sigma}'$ is transformed from local to global coordinates via $\boldsymbol{\Sigma} = \boldsymbol{\Gamma}^\top \boldsymbol{\Sigma}' \boldsymbol{\Gamma}$ or [3]

$$\begin{bmatrix} \sigma_{\mathrm{xx}} & \sigma_{\mathrm{xy}} \\ \sigma_{\mathrm{yx}} & \sigma_{\mathrm{yy}} \end{bmatrix} = \begin{bmatrix} \cos(\theta) & -\sin(\theta) \\ \sin(\theta) & \cos(\theta) \end{bmatrix} \begin{bmatrix} \sigma_{\mathrm{x'x'}} & \sigma_{\mathrm{x'y'}} \\ \sigma_{\mathrm{y'x'}} & \sigma_{\mathrm{y'y'}} \end{bmatrix} \begin{bmatrix} \cos(\theta) & \sin(\theta) \\ -\sin(\theta) & \cos(\theta) \end{bmatrix}. \tag{5.1}$$

Letting $c = \cos(\theta)$ and $s = \sin(\theta)$, the local stress tensor $\boldsymbol{\Sigma}$ is expressed as

$$\boldsymbol{\Sigma} = \begin{bmatrix} \sigma_{\mathrm{x'x'}} c^2 + \sigma_{\mathrm{y'y'}} s^2 - 2\sigma_{\mathrm{x'y'}} cs & \sigma_{\mathrm{x'x'}} cs - \sigma_{\mathrm{y'y'}} cs + \sigma_{\mathrm{x'y'}} (c^2 - s^2) \\ \sigma_{\mathrm{x'x'}} cs - \sigma_{\mathrm{y'y'}} cs + \sigma_{\mathrm{x'y'}} (c^2 - s^2) & \sigma_{\mathrm{x'x'}} s^2 + \sigma_{\mathrm{y'y'}} c^2 + 2\sigma_{\mathrm{x'y'}} cs \end{bmatrix}. \tag{5.2}$$

Rewriting the stress tensors in Voigt notation, the relation $\sigma = \mathbf{T}_\sigma^{-1} \sigma'$ ensues:

$$\begin{Bmatrix} \sigma_{\mathrm{xx}} \\ \sigma_{\mathrm{yy}} \\ \sigma_{\mathrm{xy}} \end{Bmatrix} = \begin{bmatrix} \cos^2(\theta) & \sin^2(\theta) & -2\cos(\theta)\sin(\theta) \\ \sin^2(\theta) & \cos^2(\theta) & 2\cos(\theta)\sin(\theta) \\ \cos(\theta)\sin(\theta) & -\cos(\theta)\sin(\theta) & \cos^2(\theta) - \sin^2(\theta) \end{bmatrix} \begin{Bmatrix} \sigma_{\mathrm{x'x'}} \\ \sigma_{\mathrm{y'y'}} \\ \sigma_{\mathrm{x'y'}} \end{Bmatrix}. \tag{5.3}$$

[2] The ratio between strain components does not remain constant for nonlinear materials.
[3] (5.1) is easily derived by taking equilibrium along the global x and y axes of Fig. 5.2.

The inverse transformation is obtained by substituting negative θ into (5.3):

$$\begin{Bmatrix} \sigma_{x'x'} \\ \sigma_{y'y'} \\ \sigma_{x'y'} \end{Bmatrix} = \begin{bmatrix} \cos^2(\theta) & \sin^2(\theta) & 2\cos(\theta)\sin(\theta) \\ \sin^2(\theta) & \cos^2(\theta) & -2\cos(\theta)\sin(\theta) \\ -\cos(\theta)\sin(\theta) & \cos(\theta)\sin(\theta) & \cos^2(\theta) - \sin^2(\theta) \end{bmatrix} \begin{Bmatrix} \sigma_{xx} \\ \sigma_{yy} \\ \sigma_{xy} \end{Bmatrix}. \quad (5.4)$$

Uniaxial stress is obtained by substituting $\sigma_{y'y'} = \sigma_{x'y'} = 0$ into (5.3) such that

$$\begin{aligned} \sigma_{xx} &= \sigma_{x'x'}\cos^2(\theta) = \frac{\sigma_{x'x'}}{2} + \frac{\sigma_{x'x'}}{2}\cos(2\theta), \\ \sigma_{yy} &= \sigma_{x'x'}\sin^2(\theta) = \frac{\sigma_{x'x'}}{2} - \frac{\sigma_{x'x'}}{2}\cos(2\theta), \\ \sigma_{xy} &= -\sigma_{x'x'}\cos(\theta)\sin(\theta) = -\sqrt{\sigma_{xx}\sigma_{yy}}. \end{aligned} \quad (5.5)$$

The macroscopic stress tensor is related to the corner forces via (3.23), or

$$\begin{bmatrix} \sigma_{xx} & \sigma_{xy} \\ \sigma_{yx} & \sigma_{yy} \end{bmatrix} = \frac{1}{|\Omega_\square|}\begin{bmatrix} \Delta x f_{xx} & \Delta x f_{xy} \\ \Delta y f_{yx} & \Delta y f_{yy} \end{bmatrix}, \quad (5.6)$$

where f_{yx} is the reaction force at *corner-y* due to the fixity along the x-axis. At each angle θ, the uniaxial stress $\sigma_{x'x'}$ is transformed into the corner forces. The BVP is solved and the ultimate stresses are transformed back into σ_1.

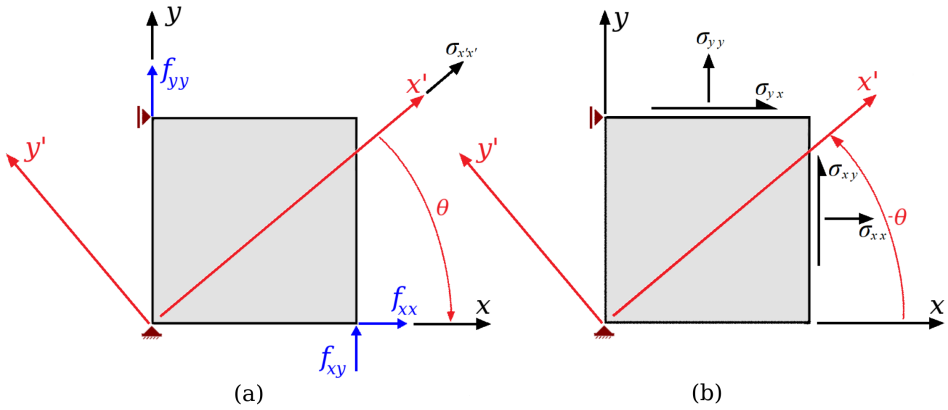

Figure 5.3: RVE: (a) corner forces; (b) resulting stresses

Letting $|\Omega_\square| = \Delta x \Delta y$ and $\Delta x = \Delta y$ yields the equations through which the uniaxial stress $\sigma_{x'x'}$ is turned into the RVE corner forces:

$$\begin{aligned} f_{xx} &= \sigma_{x'x'}\cos^2(\theta)\Delta y = \left(\frac{\sigma_{x'x'}}{2} + \frac{\sigma_{x'x'}}{2}\cos(2\theta)\right)\Delta y, \\ f_{yy} &= \sigma_{x'x'}\sin^2(\theta)\Delta x = \left(\frac{\sigma_{x'x'}}{2} - \frac{\sigma_{x'x'}}{2}\cos(2\theta)\right)\Delta x, \\ f_{xy} &= \sigma_{x'x'}\cos(\theta)\sin(\theta)\Delta y = \sqrt{f_{xx}f_{yy}}. \end{aligned} \quad (5.7)$$

The principal stress σ_1 is retrieved by transforming the corner forces back into stresses in global coordinates via (5.6) and into local coordinates via (5.4), or

$$\sigma_1 = \frac{f_{\text{xx}}}{\Delta y}\cos^2(\theta) + \frac{f_{\text{yy}}}{\Delta x}\sin^2(\theta) + 2\frac{f_{\text{xy}}}{\Delta y}\cos(\theta)\sin(\theta). \tag{5.8}$$

5.2 Localization Angle

A hypothesis was formulated in the introductory Chapter that the dependency between σ_1 and θ is not due to having a small sample size, but rather the result of choosing RVEs that are prone to strain localization under shear. To test this hypothesis, a method for estimating localization angles (ϕ_{loc}) is presented, where ϕ_{loc} is the smallest angle between a shear band and the x or y-axis.[4]

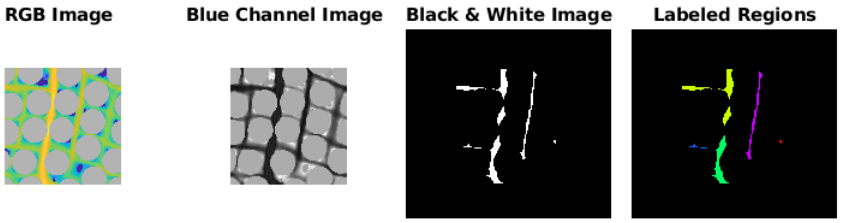

Figure 5.4: Method for obtaining the localization angle tested on rve35, $\theta = 30^o$

The orientation angles of blobs in a processed image of an RVE are used as ad-hoc estimates of the localization angles of shear bands. Using MATLAB's Image Processing Toolbox$^{\text{TM}}$, a gray-scale image is derived by extracting the blue channel of an RGB image with yellow plastic zones. A threshold value of 70 produces a binary (black and white) image whose blobs accurately portray the location of shear bands. 6 pixel long vertical and horizontal line structuring elements erode the image in an attempt to segment touching blobs. The blobs are labeled with various colors for verification. Blob orientations are given by the first eigenvector of the inertia matrix of enclosing ellipses. The blobs' orientation angles ($\phi_{\text{or}} \in (-90^o, 90^o)$) are transformed into localization angles via

$$\phi_{\text{loc},i} = \begin{cases} |\phi_{\text{or},i}|\text{, if } |\phi_{\text{or},i}| < 45^o \\ 90^o - |\phi_{\text{or},i}|\text{, otherwise.} \end{cases} \tag{5.9}$$

ϕ is estimated using a weighted average of the blobs' localization angles:

$$\phi = \frac{\sum_i A_i \phi_{\text{loc},i}}{\sum_i A_i}, \tag{5.10}$$

where A_i and $\phi_{\text{loc},i}$ are the area and localization angle of each blob, respectively.

[4] ϕ lies between 0^o (vertical or horizontal localization) and 45^o (diagonal localization).

Chapter 6

RESULTS

The coarsening factors (`cf_`) were selected based on two criteria: (1) account for the variation in results between the `cf_` = 0.01592 and `cf_` = 0.3, and (2) obtain different average number of elements on each face of $\mathcal{T}^{\mathrm{h}}$. The first criterion is satisfied by choosing factors that lay equidistant on a logarithmic scale. This ensures a greater number of coarsening factors towards `cf_` = 0.016. The second criterion is satisfied by choosing only 10 factors. The resulting number of elements on each face of $\mathcal{T}^{\mathrm{h}}$ is varied enough to provide substantially different results between one coarsening factor and the next. Fig. 6.1 shows the average number of elements per `cf_`. The double logarithmic scale preserves the quasi-linear relation between `cf_` and the average number of elements.

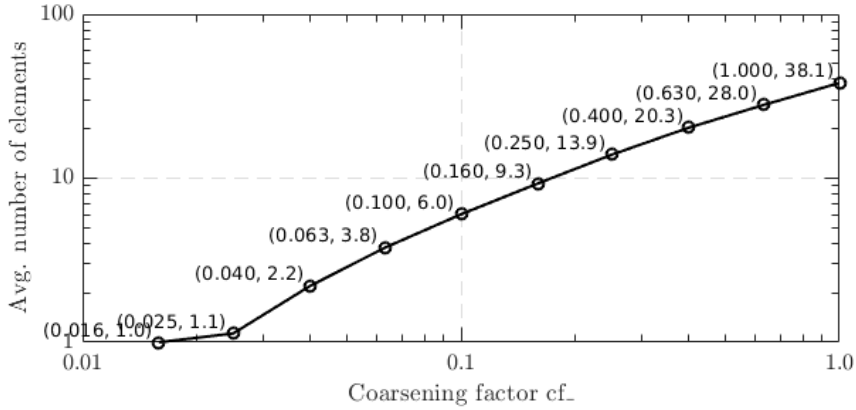

Figure 6.1: Average number of elements vs. coarsening factors

Three load step sizes were chosen based on trial: $|\mathbf{f}| = 1$, $|\mathbf{f}| = 0.5$ and $|\mathbf{f}| = 0.2$. These step sizes are larger than the one used in subsection 4.2.2: $|\mathbf{f}| = 0.1$ – abandoned herein due to its high computational requirements. During the validation of the WeakPBCModel, a rough guideline for choosing the maximum

number of steps was developed (Table 6.1). The number of steps from Section 1.3 (400) was kept because it exceeds these recommended values. Additionally, a DispArclenModel constrains *corner-y* along the x-axis and stops analyses if the displacement exceeds 0.006, thereby limiting the step count to less than 400.

Table 6.1: Recommended number of steps per load step size

load step size $\|\mathbf{f}\|$	0.1	0.2	0.5	1.0
number of steps	300	140	80	40

The thesis statement is tested on 38 out of the 48 RVEs used in Section 1.3[1]. These RVEs possess the same properties as the fiber-matrix composite from Section 4.2. Table 6.2 summarizes relevant parameters from the properties file.

Table 6.2: Summary of model properties and module parameters

Fibers (SolidModel)	Thickness	1
	Material	Hooke
	State	Plane strain
	Young's modulus	74000
	Poisson's ratio	0.2
	Shape	Triangle3
	Integration scheme	Gauss1
Matrix (SolidModel)	Thickness	1
	Material	Melro
	State	Plane strain
	Young's modulus	3760
	Poisson's ratio	0.3
	Plastic Poisson's ratio	0.39
	Yield stress	80
	Shape	Triangle3
	Integration scheme	Gauss1
Arclen (DispArclenModel)	Initial displacement	0.0
	Maximum displacement	0.006
	Constraints	cornery (dx)
	Load table	load.data
Periodic (WeakPBCModel)	Coarsening factor	See Fig. 6.1
	Strain rate	None
Stepper (FlexArclenModule)	Solver	SkylineLU
	Precision	$1 \cdot 10^{-3}$
	Number of iterations	20

The applied macroscale uniaxial stress is scaled via $\sigma_{xx}\Delta y = |\mathbf{f}|$ and transformed into corner forces per the procedure in Section 5.1. The forces are written to

[1] 12 rves were removed because they diverged before reaching the ultimate principal stress.

load.data, which is used as input for the DispArclenModel. On the other hand, each coarsening factor from Fig. 6.1 is explicitly specified in the properties file.

6.1 Principal Stress vs. Orientation Angle

The results of the procedure outlined in Fig. 5.1 are presented herein. Uniaxial load was applied to each RVE at 46 different angles between 0^o and 90^o to generate curves of ultimate principal stress (σ_1) vs. orientation angle (θ). Fig. 6.2 shows how σ_1 and ϕ are retrieved. At each angle θ, uniaxial stress is transformed into corner forces. The ultimate principal stress σ_1 is the maximum principal stress obtained from solving the BVP on the RVE. The localization angle ϕ is estimated using an image of the RVE without deformation at the last load step.

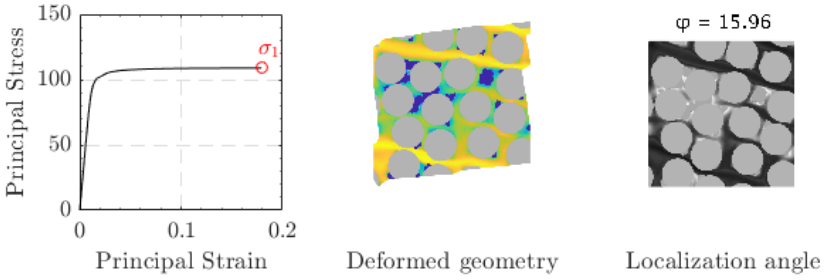

Figure 6.2: Principal stress and localization angle of rve1, $\theta = 24^o$

The ultimate principal stresses[2] of each RVE were recorded to generate σ_1-θ curves as in Fig. 6.3. Then, the curves from all 38 RVEs were averaged to produce a single characteristic $\bar{\sigma}_1$-θ curve. This process was executed with the 10 chosen coarsening factors and 3 load steps, yielding a total of 30 $\bar{\sigma}_1$-θ curves.

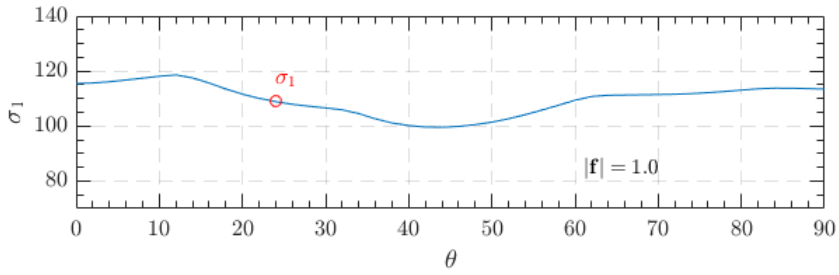

Figure 6.3: Principal stress vs. orientation angle of rve1 ($\texttt{cf\_} = 0.016$)

Here, the results for the following coarsening factors are presented: 0.016 and 0.063. Fig. 6.4 shows the σ_1-θ curves of all RVEs with $\texttt{cf\_} = 0.016$. For

[2]Hereinafter, the ultimate principal stress is simply called principal stress or σ_1.

each load step, the average principal stress ($\bar{\sigma}_1$) is shown in red with error bars representing the standard deviation (s_{σ_1}). Fig. 6.5 compares these $\bar{\sigma}_1$-θ curves: μ is the average of $\bar{\sigma}_1$ and σ is the average of s_{σ_1} along each curve. Manifestly, results are insensitive to $|\mathbf{f}|$.

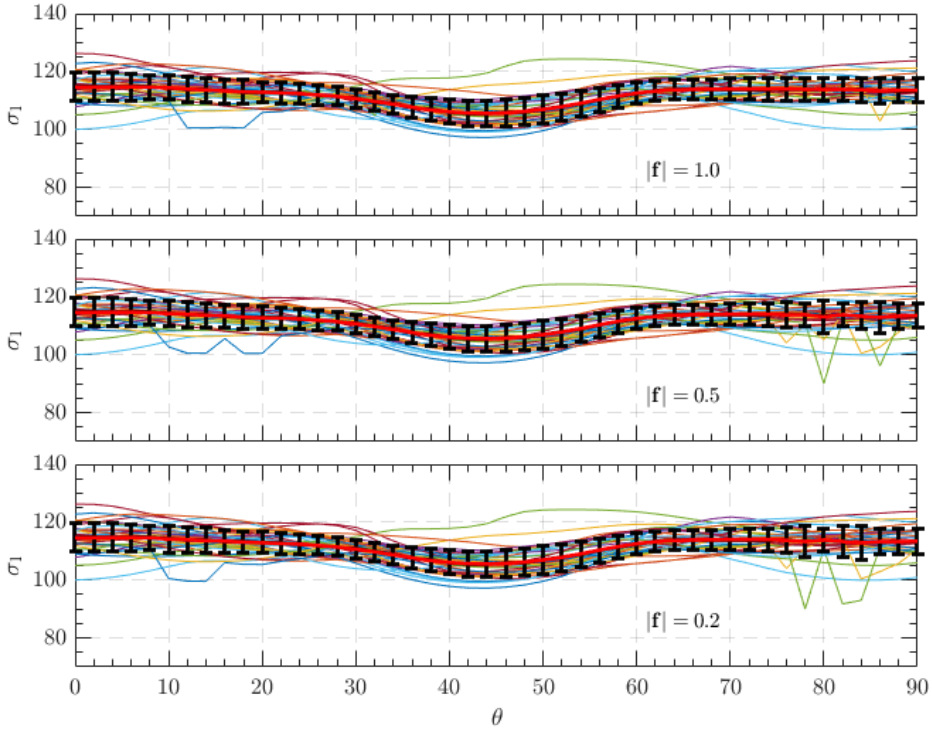

Figure 6.4: Principal stress vs. orientation angle ($\texttt{cf}_{-} = 0.016$)

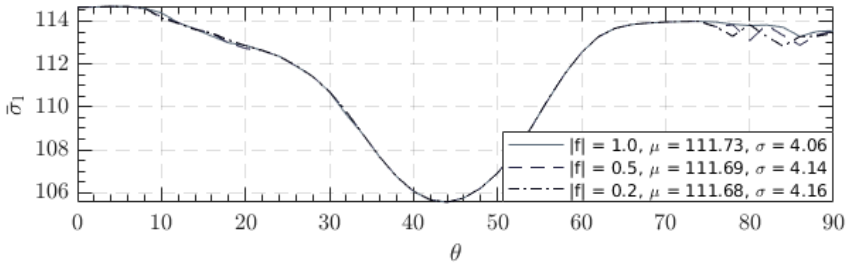

Figure 6.5: Average principal stress vs. orientation angle ($\texttt{cf}_{-} = 0.016$)

Fig. 6.6 shows the σ_1-θ curves of all RVEs with $\texttt{cf}_{-} = 0.063$ and Fig. 6.7 shows the $\bar{\sigma}_1$-θ curves per load step. Here, decreasing $|\mathbf{f}|$ displays a slight improvement in convergence. This is evidenced by the increasing values of μ and decreasing

values of σ. Most coarsening factors exhibit a similar trend (c.f. Table C.1).

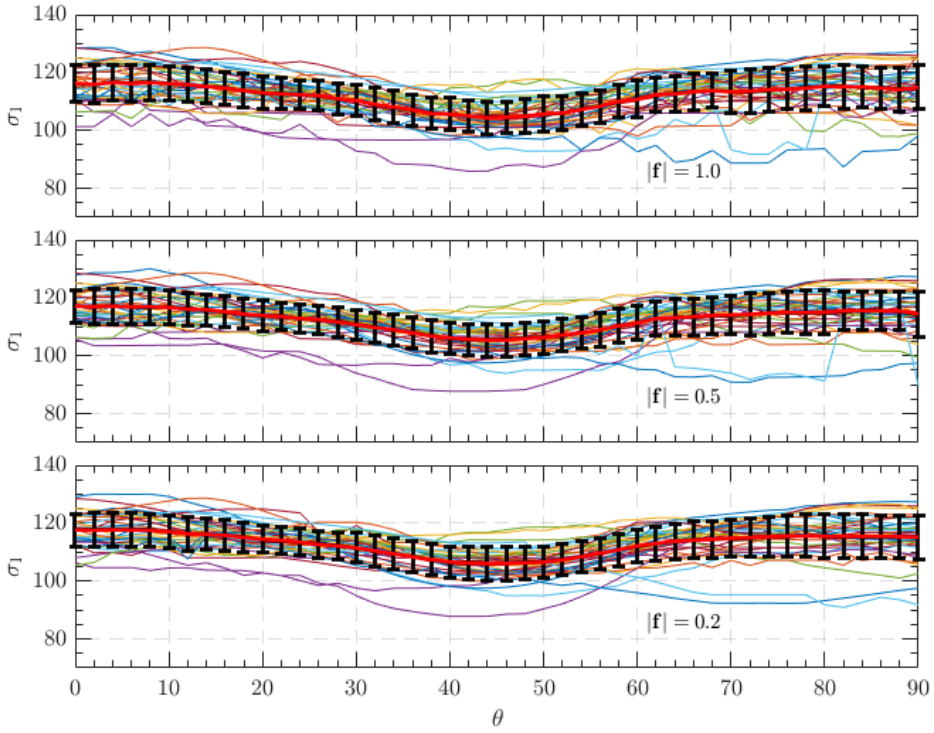

Figure 6.6: Principal stress vs. orientation angle ($\texttt{cf\_} = 0.063$)

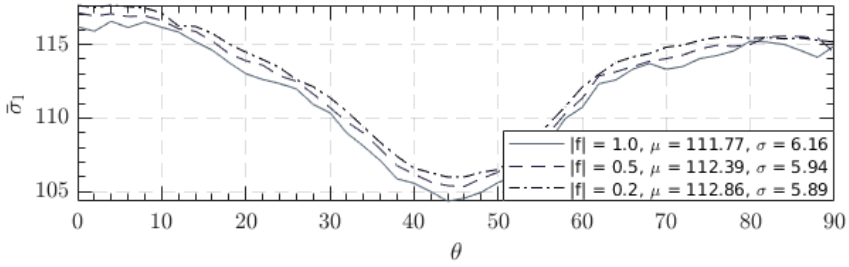

Figure 6.7: Average principal stress vs. orientation angle ($\texttt{cf\_} = 0.063$)

The results for all remaining coarsening factors can be found in Appendix C, with all values of μ and σ epitomized in Table C.1. Generally, reducing $|\mathbf{f}|$ and increasing $\texttt{cf\_}$ elevate the values of $\bar{\sigma}_1$ by lowering the standard deviations and by imposing stricter periodicity conditions. However, the increase due to the former may not be substantial enough (compared to the increase due to $\texttt{cf\_}$) to justify the additional computational effort. Henceforth, only the results of

analyses performed with $|\mathbf{f}| = 1$ are shown. Fig. 6.8 compares the $\bar{\sigma}_1$-θ curves per coarsening factor. In essence, it delivers the data in a condensed form.

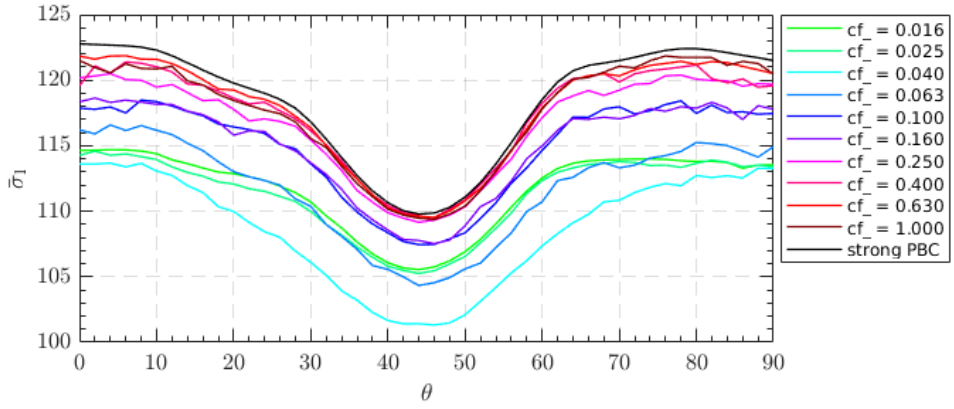

Figure 6.8: Average principal stress vs. orientation angle ($|\mathbf{f}| = 1.0$)

Table 6.3 presents the maximum and minimum values of the average principal stresses $\bar{\sigma}_1$. The PeriodicBC results are re-evaluated with only 38 RVEs for a proper comparison. It is highlighted that decreasing `cf_` reduces the difference between the maximum and minimum values of $\bar{\sigma}_1$, thereby showing that weakening the periodicity constraint reduces the dependency between $\bar{\sigma}_1$ and θ.

Table 6.3: Average principal stress and standard deviation per coarsening factor

Coarsening factor (cf_)	**Average stress μ**	**Average std. dev. σ**	$\max \bar{\sigma}_1$	$\min \bar{\sigma}_1$	$\max(\bar{\sigma}_1) - \min(\bar{\sigma}_1)$
0.016	111.73	4.06	114.69	105.55	9.14
0.025	111.35	4.92	114.58	105.26	9.32
0.040	108.68	7.17	113.67	101.31	12.36
0.063	111.77	6.16	116.58	104.33	12.25
0.100	114.85	5.46	118.48	107.45	11.03
0.160	114.98	5.97	118.64	107.53	11.11
0.250	116.72	5.54	120.50	109.16	11.34
0.400	117.42	5.25	121.39	109.52	11.87
0.630	117.76	5.00	121.86	109.52	12.34
1.000	117.57	5.54	121.85	109.38	12.47
PeriodicBC	118.44	4.53	122.78	109.79	12.99

6.1.1 Statistical Analysis

The thesis statement is tested by analyzing the results per the procedure in Appendix A. If the results with the lowest coarsening factor (Fig. 6.9) gainsay it, then tests with finer meshes are guaranteed the same negative outcome.

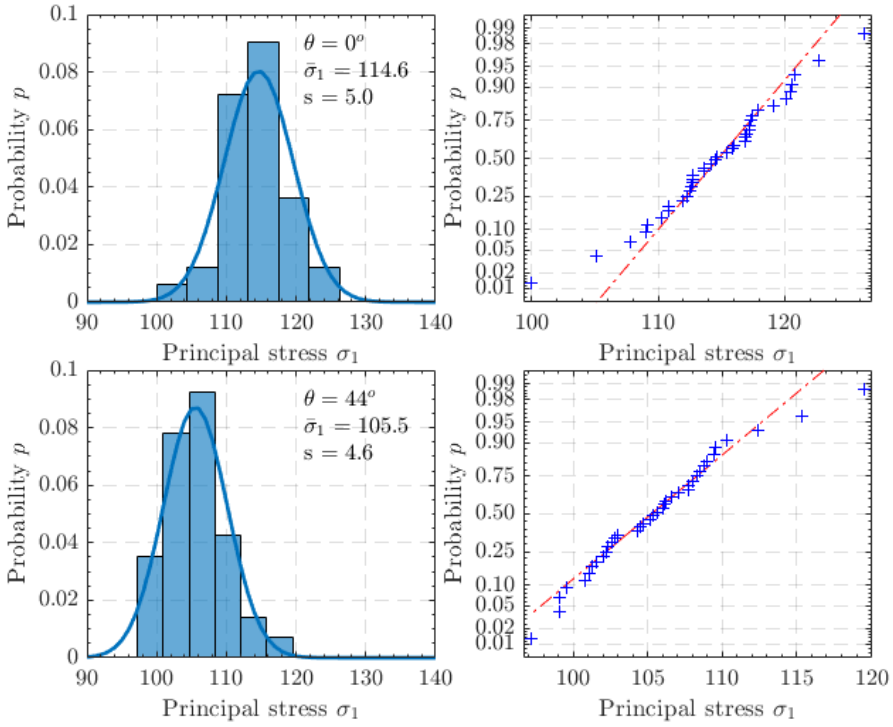

Figure 6.9: Histograms and normal probability plots for `cf_` = 0.016

Indeed, Welch's t-test rejects the null hypothesis with $p = 3.7 \cdot 10^{-10}$. That is, weak periodic boundary conditions do not alleviate the dependency between $\bar{\sigma}_1$ and θ – not even in their weakest form. The following conclusions are drawn:

- It suffices to glance at the data to invalidate the thesis statement. This is backed up by the statistic analysis, where the null hypothesis – that is, $\mu_{\sigma_1}(\theta = 0^o) = \mu_{\sigma_1}(\theta = 44^o)$ – is rejected with $p = 3.7 \cdot 10^{-10}$.
- Decreasing `cf_` reduces the difference of the maximum and minimum values of the average ultimate principal stress $\bar{\sigma}_1$ (See Table. C.1).
- Increasing `cf_` elevates the values of $\bar{\sigma}_1$ throughout the range of θ, but more so towards $\theta = 0^o$, by imposing more exacting periodicity conditions.
- The WeakPBCModel is not as robust as the PeriodicBCModel, as evidenced by increased standard deviations towards `cf_` = 1.0.

6.2 Principal Stress vs. Localization Angle

In this section, it is verified whether the lower value of $\bar{\sigma}_1$ at $\theta = 44^o$ is caused by choosing RVEs prone to strain localization under shear. This hypothesis is based on the observation that shear bands due to uniaxial stress at $\theta = 45^o$ tend to respect periodicity of displacements. Fig. 6.10 schematizes this behavior.

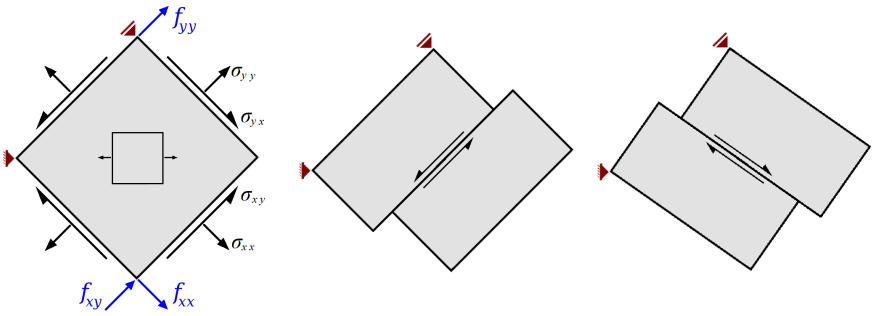

Figure 6.10: Preferred localization modes at $\theta = 45^o$

Here, preferred localization modes refers to those respecting periodicity. Clearly, the shear bands in Fig. 6.10 may shift sideways facilitating the formation of these preferred modes. Fig. 6.11 furnishes a few examples of periodic deformations (rve13 and rve50) as well as non-periodic deformations: a vertical shear band combined with multiple horizontal bands (rve35) and viceversa (rve44).

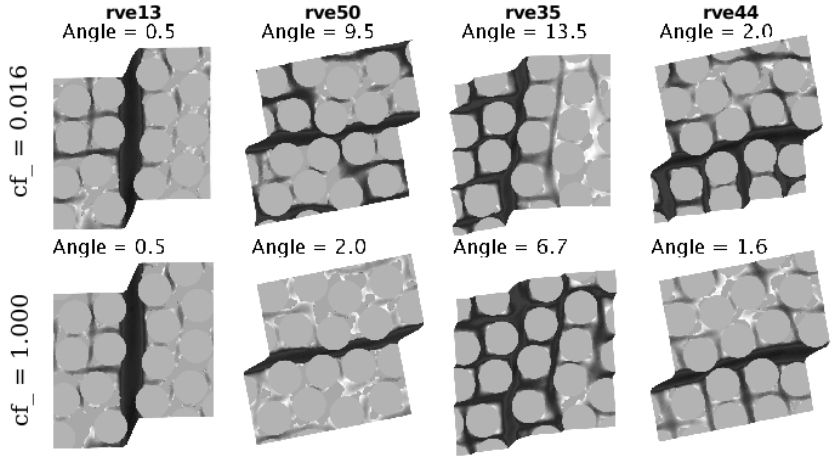

Figure 6.11: Examples of localization modes at $\theta = 44^o$

The non-periodic deformations from rve35 and rve44 may only occur with weak periodic boundary conditions and a coarse traction mesh (`cf_` = 0.016). These deformations vanish when a standard mesh is used instead (`cf_` = 1.000).

Likewise, Fig. 6.12 shows the preferred localization modes at $\theta = 0^o$. While these shear bands may also shift sideways, the probability that the fibers are favorably aligned is lower because two shear bands are required instead of one.

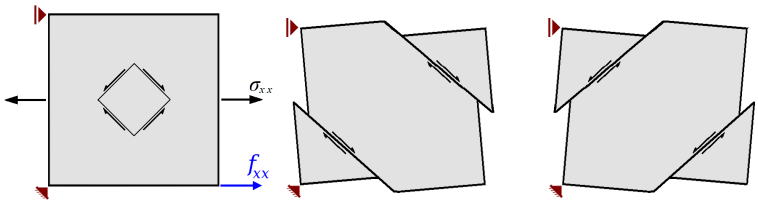

Figure 6.12: Preferred localization modes at $\theta = 0^o$

Fig. 6.13 presents the RVEs whose deformations most closely resemble Fig. 6.12: rve50 and rve28. In fact, non-periodic localization is more common. For instance, rve42 displays an anti-periodic deformation that is an amalgam of both localization modes from Fig. 6.12 and rve33 culminates with a single shear band.

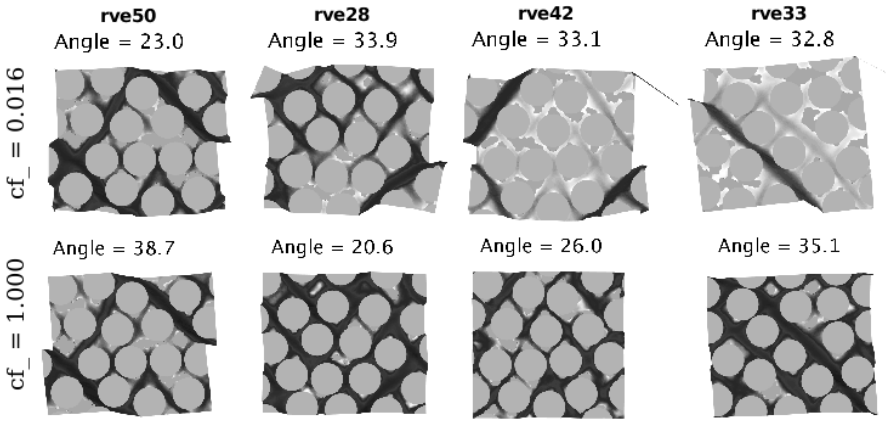

Figure 6.13: Examples of localization modes at $\theta = 0^o$

At higher coarsening factors, the non-periodic deformations mutate into axial deformations while periodic deformations are sometimes exacerbated (rve50). Appendix D and E provide more deformation examples for all coarsening factors. Based on these figures, the following inferences are made about the values of ϕ:

- Angles near 0^o indicate well-formed vertical or horizontal shear bands.
- Angles higher than 30^o tend to indicate well-formed diagonal shear bands.
- Angles around 20^o are usually associated with pure uniaxial tension.

From these inferences, it becomes clear that the hypothesis can be tested merely by comparing σ_1 to ϕ at $\theta = 0^o$ and $\theta = 44^o$. The goal is to confirm whether

values of ϕ close to 0^o do indeed yield lower values of σ_1. This is achieved by means of scatter plots and MATLAB's `corr` function – whose output subsumes the Pearson's correlation coefficient (ρ) and its corresponding p-value.[3] Fig. 6.14 and Fig. 6.15 present the results for $\texttt{cf\_} = 0.016$ and $\texttt{cf\_} = 0.063$, respectively.

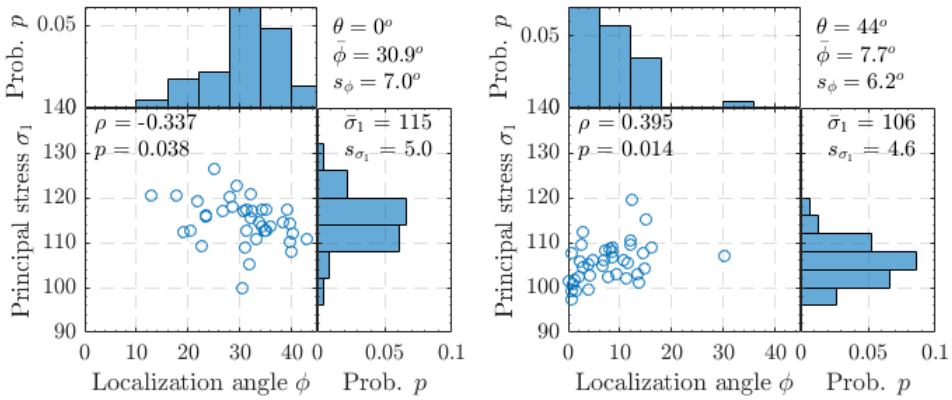

Figure 6.14: Scatter plot of localization angle vs. principal stress ($\texttt{cf\_} = 0.016$)

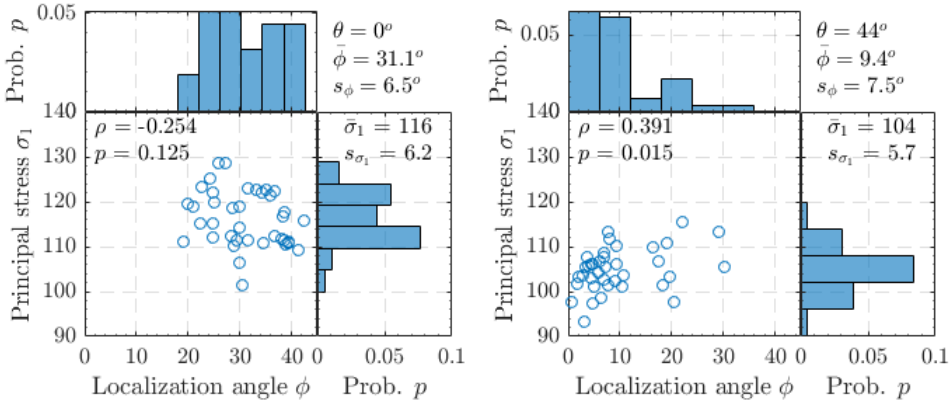

Figure 6.15: Scatter plot of localization angle vs. principal stress ($\texttt{cf\_} = 0.063$)

At $\theta = 44^o$, the null hypothesis ($\rho = 0$) is rejected in favor of the alternate hypothesis ($\rho \neq 0$) with $p \leq 0.05$ in both occasions. That is, there is ample evidence to ascertain that the preferred localization modes ($\phi \approx 0^o$) yield lower values of σ_1. Au contraire, the scatter plots at $\theta = 0^o$ are more haphazard with less significant correlations, evidenced by lower values of ρ and higher p-values. This means the preferred localization modes ($\phi \approx 45^o$) occur less frequently and may not yield lower values of σ_1. The same trends are observed in Fig. 6.16 and Fig. 6.17, which present the results for $\texttt{cf\_} = 0.016$ and $\texttt{cf\_} = 0.063$, respectively.

[3] $p < \alpha = 0.05$ disproves $\mathbf{H}_0 : \rho = 0$. That is, the correlation is statistically significant.

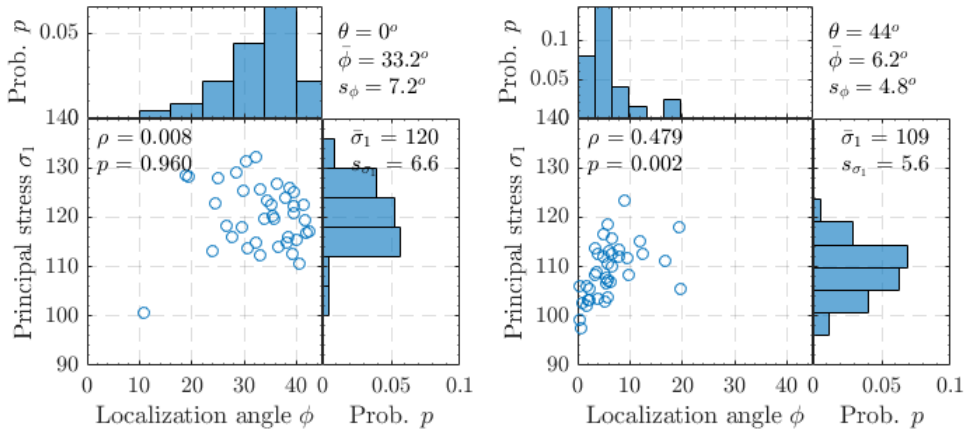

Figure 6.16: Scatter plot of localization angle vs. principal stress (`cf_` = 0.250)

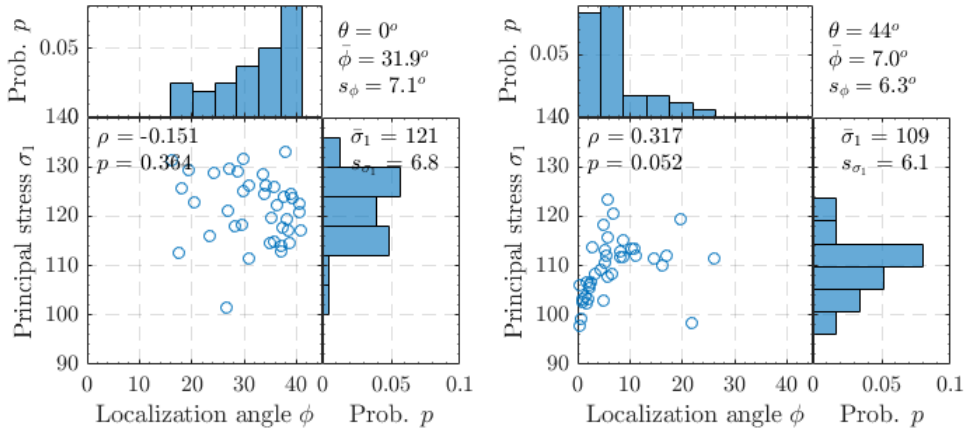

Figure 6.17: Scatter plot of localization angle vs. principal stress (`cf_` = 1.000)

Appendix F presents plots for all 10 coarsening factors: $\mathbf{H}_0$ was rejected 8 times at $\theta = 44^o$, validating the correlation. The following conclusions are gathered:

- The positive correlation between ϕ and σ at $\theta = 44^o$ is highly significant, meaning that the preferred localization modes lead to lower values of σ_1.
- The correlation between ϕ and σ at $\theta = 0^o$ is not significant, meaning the preferred localization modes do not necessarily lead to lower values of σ_1.
- Overall, the lower values of $\bar{\sigma}_1$ around $\theta = 45^o$ can be attributed to the formation of localization bands under shear which respect periodicity.

6.3 Localization Angle vs. Orientation Angle

As a final step, it is hypothesized that lowering `cf_` widens the range of θ around 45^o over which localization with a single shear band is permissible (Fig. 6.18). Au contraire, increasing `cf_` demands multiple shear bands to maintain periodicity of displacements at θ other than 45^o due to stricter periodicity requirements.

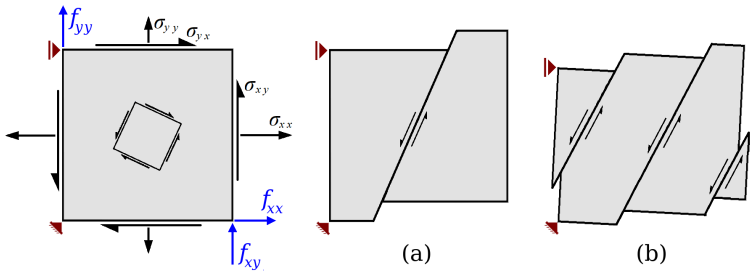

Figure 6.18: Localization modes: (a) weak periodicity; (b) strong periodicity

Fig. 6.18 suggests that ϕ is not likely to change regardless of coarsening factors. In fact, the scatter plots in Appendix F contain measurements at additional orientation angles near $\theta = 45^o$ which reveal that $\bar{\phi}$ does not change much (Fig. 6.19). Rather, lower values of `cf_` increase the scatter and decrease $\bar{\sigma}_1$.

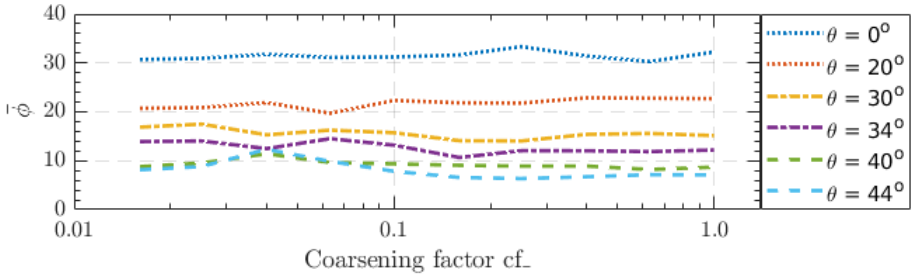

Figure 6.19: Localization angle vs. coarsening factor

Careful observation of the localization patterns of RVEs across all orientation angles sheds some light: new shear bands only begin to form when there is a gap between the fibers that is favorably aligned with respect to the orientation angle – the difference of θ and ϕ is near 45^o. The transition from old to new shear bands is not gradual. Once the fibers are favorably aligned, the change is swift. Otherwise, the current shear bands remain until new ones can form. Particularly towards $\theta = 0^o$ and $\theta = 90^o$, RVEs may exhibit complete plastification while switching from one localization mode to the next. As a result of all this, changes in ϕ over a small range of θ may either be very abrupt or insignificant.

Fig. 6.20 epitomizes this behavior. The load near $\theta = 0^o$ triggers shear bands which yield a low value of σ_1. Increasing `cf_` raises σ_1 significantly due to stricter periodicity conditions which deter anti-periodic localization in favor of pure axial deformation. Towards $\theta = 45^o$, the vertical shear bands respect periodicity, leading to very low values of σ_1 regardless of the coarsening factor.

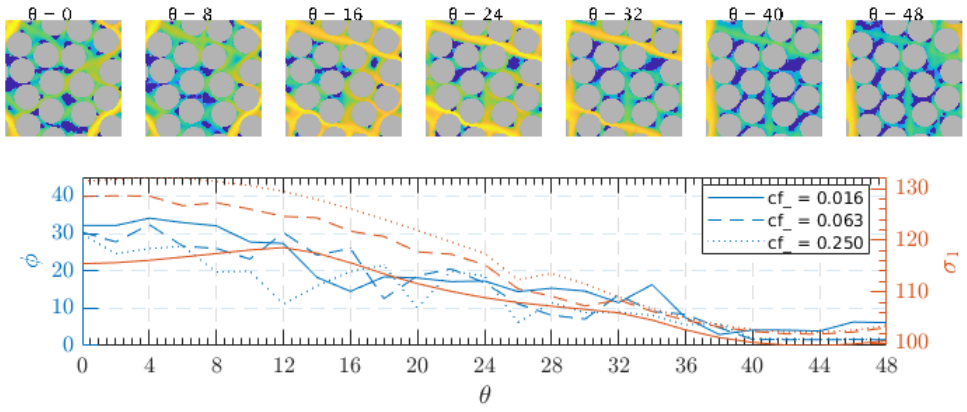

Figure 6.20: Transition between shear bands (rve1)

Rve6 presents a single shear band near $\theta = 0^o$, which resembles a preferred localization mode with a missing shear band. This "semi-periodic" mode yields a very low value of σ_1. Like rve1, increasing `cf_` raises σ_1 due to stricter periodicity conditions which preclude non-periodic localization. Rve22 in Appendix G presents a similar localization mode, albeit with two shear bands (periodic).

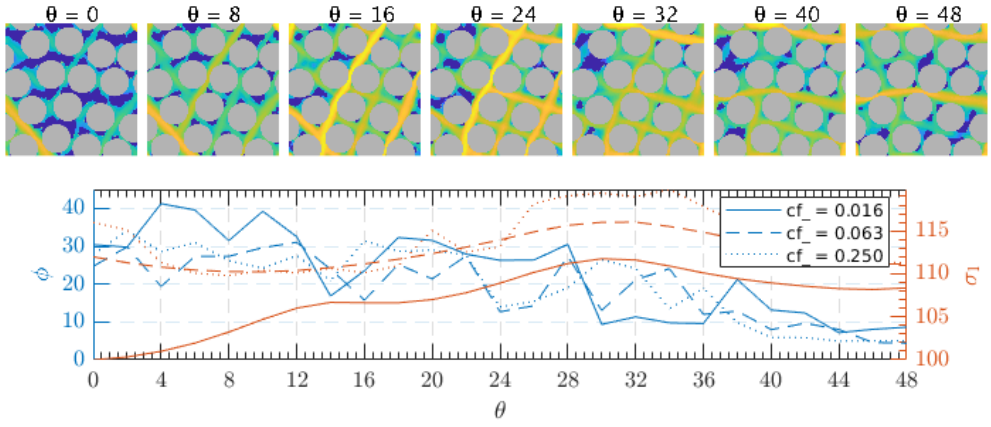

Figure 6.21: Transition between shear bands (rve6)

Rve13 presents diagonal shear bands ($\phi \approx 45^o$) near $\theta = 0^o$ with low σ_1. Soon after, the shear bands turn vertical ($\phi \approx 0^o$) and σ_1 increases. σ_1 diminishes as the fibers regain a favorable alignment, towards $\theta = 45^o$. Just like rve1, increasing `cf_` elevates σ_1 towards $\theta = 0^o$ due to stricter periodicity conditions.

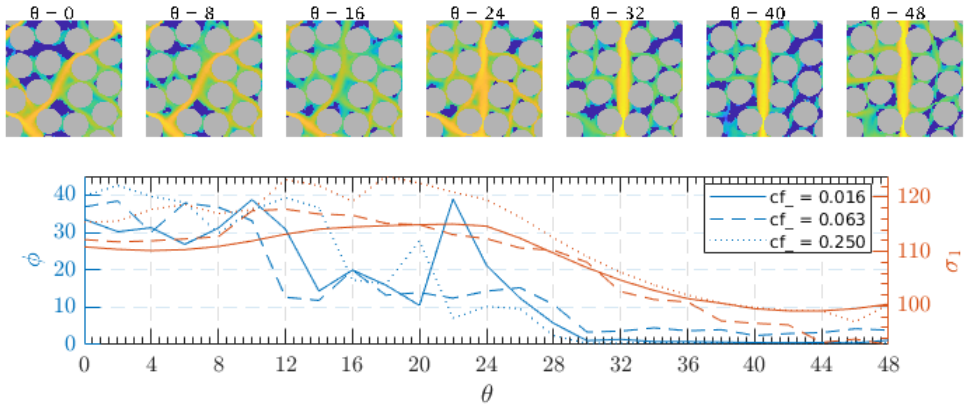

Figure 6.22: Transition between shear bands (rve13)

Rve41 presents a localization mode that best conforms to the hypothesis. The shear band ($\phi \approx 10^o$) around $\theta = 32^o$ is exemplary of Fig. 6.18(a) and yields a very low σ_1. Rve42 in Appendix G presents a similar trend around $\theta = 8^o$.

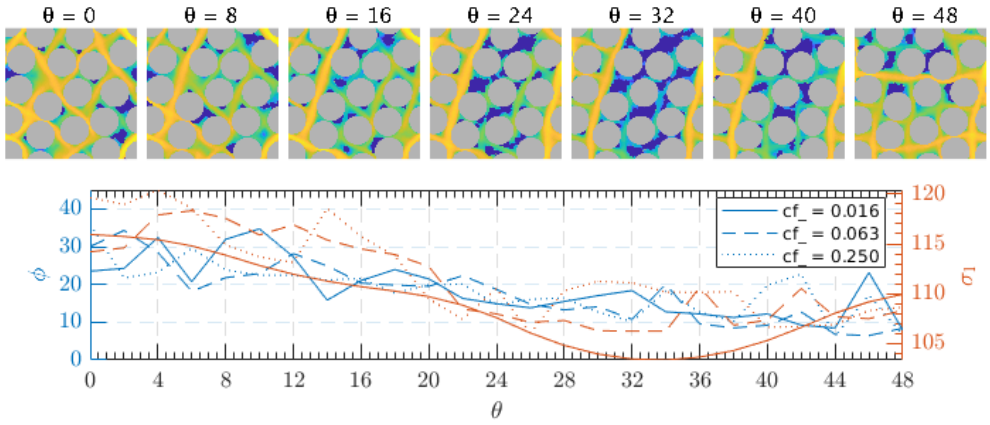

Figure 6.23: Transition between shear bands (rve41)

It was expected to see more RVEs exhibit the hypothesized behavior. The scarcity of RVEs with favorably aligned fibers leading to slightly diagonal shear bands means that not much difference is observed between strong and weak periodicity, except at low coarsening factors, which allow non-periodic localization

with low values of σ_1 throughout θ. The following conclusions are gathered:

- Very low `cf_` allows non-periodic shear bands with low σ_1 throughout θ. However, single shear bands respecting periodicity tend to yield lower σ_1.
- Increasing `cf_` raises σ_1 towards $\theta = 0^o$ due to stricter periodicity, which deters non-periodic localization in favor of pure axial deformation.
- New shear bands form only once the fibers are favorably aligned with respect to the load orientation angle; that is, ϕ is at around 45^o from θ.
- Increasing `cf_` limits the range of ϕ over which localization with a single shear band is permissible. Few RVEs' fibers are aligned such that ϕ falls within this narrower range.

Fig. 6.24 is included herein for the sake of completeness: averaging all values of ϕ presents a bilinear relation between $\bar{\phi}$ and θ.

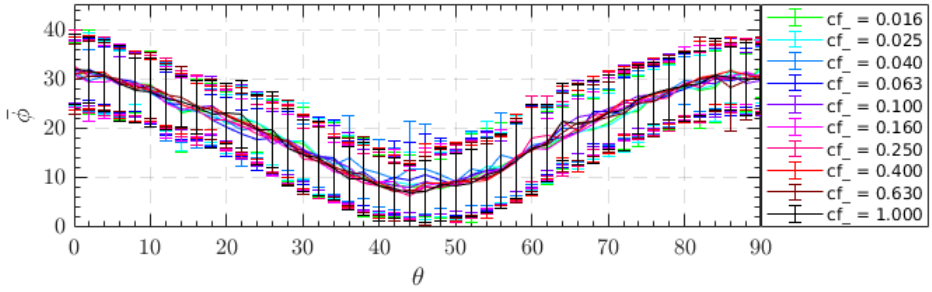

Figure 6.24: Localization angle vs. orientation angle

This figure shows that ϕ remains constant regardless of `cf_`; however, it obfuscates the fact that each individual ϕ does not have a linear relation with respect to θ. Rather, it stays "constant" over a range of θ until a new shear band develops. It is highlighted that ϕ remaining constant indicates that increasing `cf_` simply raises the number of parallel shear bands needed to satisfy periodicity of displacements. This may not be necessarily true towards $\theta = 0^o$ where the angle ϕ does not accurately differentiate between diagonal shear bands and complete plastification due to pure axial deformation.

Chapter 7

CONCLUSIONS

7.1 Summary

The goal of this research work was to evaluate whether applying weak periodic boundary conditions instead of strong periodic boundary conditions alleviates the observed dependency between the average principal stress $\bar{\sigma}_1$ and orientation angle θ of fiber-matrix composite RVEs under uniaxial loading. The goal was achieved by implementing a modified weak periodic boundary conditions model, which grants application of external forces to represent macroscale stresses; and a methodology for the automated analysis of the localization angles. This model was used to test the thesis statement on a batch of 38 RVEs at 46 angles between 0^o and 90^o, using 10 different coarsening factors and 3 load step sizes.

7.2 Conclusions

This treatise answers three main questions with regards to the effects of weak periodic boundary conditions on the average principal stress due to axial load under varying orientations. These questions, and their answers, follow.

7.2.1 Does weak micro-periodicity alleviate the dependency between $\bar{\sigma}_1$ and θ?

The statistical analysis in Section 6.1 clearly shows that weak periodic boundary conditions do not remove the dependency between $\bar{\sigma}_1$ and θ – not even in their weakest form. In fact, the hypothesis that $\bar{\sigma}_1(\theta = 44^o)$ and $\bar{\sigma}_1(\theta = 0^o)$ come from populations with equal means is disproved with a p-value as small as $3.7 \cdot 10^{-10}$. However, low coarsening factors do reduce the difference between $\max(\bar{\sigma}_1)$ and $\min(\bar{\sigma}_1)$. The following trends are worth mentioning:

- Increasing `cf_` elevates $\bar{\sigma}_1$ due to stricter periodicity conditions.
- The increase in $\bar{\sigma}_1$ due to lower $|\mathbf{f}|$ is not as substantial as due to `cf_`.

- The WeakPBCModel is not as robust as the PeriodicBCModel.

7.2.2 Is this dependency the result of RVEs prone to localization under shear?

The fluctuation of $\bar{\sigma}_1$ along θ can be attributed to RVEs which are prone to localization under shear. The statistical study in Section 6.2 provides ample evidence of a high positive correlation between σ_1 and the localization angle ϕ at $\theta = 44^o$, meaning that values of ϕ near 0^o (vertical or horizontal shear bands) lead to lower principal stresses. Likewise, there is little evidence of a weaker negative correlation between σ_1 and ϕ at $\theta = 0^o$, which indicates that diagonal shear bands do occur but may not necessarily yield lower principal stresses. Recapitulating:

- The positive correlation between ϕ and σ at $\theta = 44^o$ is highly significant, meaning that the preferred localization modes lead to lower values of σ_1.
- The correlation between ϕ and σ at $\theta = 0^o$ is not significant, meaning the preferred localization modes do not necessarily lead to lower values of σ_1.
- Overall, the lower values of $\bar{\sigma}_1$ around $\theta = 45^o$ can be attributed to the formation of localization bands under shear which respect periodicity.

7.2.3 Do smaller coarsening factors widen the range of θ over which localization with a single shear band is permissible?

Unfortunately, the current sample did not provide enough evidence to support the claim that lower values of `cf_` widen the range of θ over which localization with a single shear band is permissible. In fact, this behavior was only observed in a couple of RVEs, namely 41 and 42. The following conclusions are gathered:

- Very low `cf_` allows non-periodic shear bands with low σ_1 throughout θ. However, single shear bands respecting periodicity tend to yield lower σ_1.
- Increasing `cf_` raises σ_1 towards $\theta = 0^o$ due to stricter periodicity, which deters non-periodic localization in favor of pure axial deformation.
- New shear bands form only once the fibers are favorably aligned with respect to the load orientation angle; that is, ϕ is at around 45^o from θ.
- Increasing `cf_` limits the range of ϕ over which localization with a single shear band is permissible. Few RVEs' fibers are aligned such that ϕ falls within this narrower range.

Overall, only very low coarsening factors widen the range of θ over which localization with a single shear band is permissible. Small increases in `cf_` vastly reduce the range of ϕ which would result in a single shear band. Additionally, the following remarks are made about the orientation angles:

- ϕ does not seem to change regardless of `cf_`. This may indicate that increasing `cf_` simply raises the number of parallel shear bands needed to satisfy periodicity of displacements.
- Nonetheless, ϕ does not accurately differentiate between diagonal shear bands and complete plastification due to pure axial deformation.

7.3 Recommendations

This treatise studied the effect on $\bar{\sigma}_1$ due to axial load with changing θ. Although weak periodic boundary conditions are used within a deformation-driven procedure, providing a solution to the dependency between $\bar{\sigma}_1$ and θ for the force-driven procedure should also alleviate fluctuations in the conventional context. Further research should aim to suppress them. Here are some suggestions:

- In this study, the preferred localization angles are a good estimate of ϕ. One solution may be to rotate the periodicity constraint such that it is aligned with the localization angle as suggested by (Svenning et al., 2017).
- In the deformation-driven procedure, it may be harder to estimate ϕ. Another study could investigate ways of predicting the preferred localization angles or ϕ based on the given macroscopic strain tensor ($\bar{\mathbf{u}} \otimes \nabla$).
- Finally, it would be ideal to extend these concepts to three dimensions. The major obstacle in the implementation is the traction mesh creation. It might be useful to establish a minimum element area based on a coarsening factor. Additionally, one might use a regular mesh or other mesh generation tools instead of mapping nodes from $\Gamma^-_\square$ and $\Gamma^+_\square$ onto $\Gamma^+_\square$.

The RVE sample in this study is susceptible to shear: the low values of σ_1 due to shear failure may be attributed to the plastic behavior of the matrix. Likewise, most RVEs precluded the formation of slightly diagonal shear bands. Factors that might influence this include: RVE size, mesh size and fiber density. Finally, the angle ϕ failed to clearly distinguish diagonal shear bands from pure axial deformation. Therefore, the following recommendations are presented:

- Use softening to more accurately model the matrix material behavior.
- Perform a similar study with a larger sample of non-periodic RVEs.
- Study the effect of RVE and mesh size on the formation of shear bands.
- Study the effect of fiber density and size on the formation of shear bands.
- Improve ϕ to distinguish diagonal shear bands from uniaxial deformation.

It is hypothesized that softening might reverse the $\bar{\sigma}_1$ fluctuations: crack formation near $\theta = 0^o$ might yield lower σ_1 than non-periodic cracks near $\theta = 45^o$.

Bibliography

Coenen, E., Kouznetsova, V., & Geers, M. (2012). Novel boundary conditions for strain localization analysis in microstructural elements. *International Journal for Numerical Methods in Engineering*, *90*, 1–21.

Dekking, F., Kraaikamp, C., Lopuhaä, H., & Meester, L. (2005). *A modern introduction to probability and statistics: understanding why and how*. Springer.

Dynaflow Research Group. (n.d.). Jem jive c++ library. Retrieved from https://jive.dynaflow.com/

Geers, M., Kouznetsova, V., & Brekelmans, W. (2010). Multi-scale computational homogenization: trends and challenges. *Journal of Computational and Applied Mathematics*, *234*, 2175–2182.

Geuzaine, C. & Remacle, J. (2018). Gmsh (Version 3.0). Retrieved from http://gmsh.info/

Karamnejad, A. (2016). *Multiscale computational modeling of brittle and ductile materials under dynamic loading*. Delft University of Technology.

Kouznetsova, V., Geers, M., & Brekelmans, W. (2010). Computational homogenization for non-linear heterogeneous solids. In U. Galvanetto & M. Aliabadi (Eds.), *Multiscale modeling in solid mechanics* (Chap. 1, pp. 1–42). London, U.K.: Imperial College Press.

Larsson, F., Runesson, K., Saroukhani, S., & Vafadari, R. (2011). Computational homogenization based on a weak format of micro-periodicity for rve-problems. *Computer Methods in Applied Mechanics and Engineering*, *200*, 11–26.

Melro, A., Camanho, P., Andrade Pires, F., & Pinho, S. (2013). Micromechanical analysis of polymer composites reinforced by unidirectional fibres: part ii – micromechanical analyses. *International Journal of Solids and Structures*, *50*, 1906–1915.

Öhman, M., Runesson, K., & Larsson, F. (2015). On the variationally consistent computational homogenization of elasticity in the imcompressible limit. *Advanced Modeling and Simularion in Engineering Sciences*, *2:1*, 1–29.

Runesson, K. & Larsson, F. (2011). Computational homogenization and multiscale modeling [powerpoint siles]. Retrieved from https://www.sintef.no/globalassets/project/evitameeting/2011/runessonlarsson_geilo2011_lect1.pdf

Sandström, C., Larsson, F., & Runesson, K. (2014). Weakly periodic boundary conditions for the homogenization of flow in porous media. *Advanced Modeling and Simulation in Engineering Sciences*, *2:12*, 1–24.

Sluys, B. (2017). Multi-scale modeling of localized failure processes [powerpoint siles].

Svenning, E., Fagerström, M., & Larsson, F. (2016). Computational homogenization of microfractured continua using weakly periodic boundary conditions. *Computer Methods in Applied Mechanics and Engineering*, *299*, 1–21.

Svenning, E., Fagerström, M., & Larsson, F. (2017). Localization aligned weakly periodic boundary conditions. *International Journal for Numerical Methods in Engineering*, *111*, 493–500.

van der Meer, F. (2016). Periodicbcmodel.cpp.

Wells, G. (2009). *The finite element method: an introduction.* University of Cambridge and Delft University of Technology.

Appendices

Appendix A

Study on Periodic Boundary Conditions

As described in section 1.3, uniaxial stress was applied to 48 different fiber-matrix composite RVEs at 46 different angles between 0^o and 90^o to generate the curves of principal stress (σ_1) vs. orientation angle (θ) shown below.

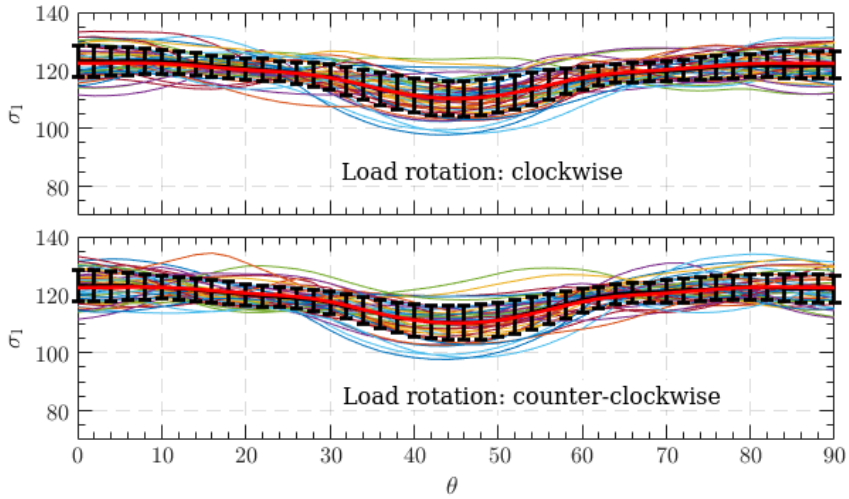

Figure A.1: Principal stress vs. angle, strong periodic boundary conditions

This experiment was performed for both a clockwise and anticlockwise rotation of the RVEs, resulting in different individual σ_1–θ curves but the same curve of average principal stress ($\bar{\sigma}_1$) vs. θ (Fig. A.1).

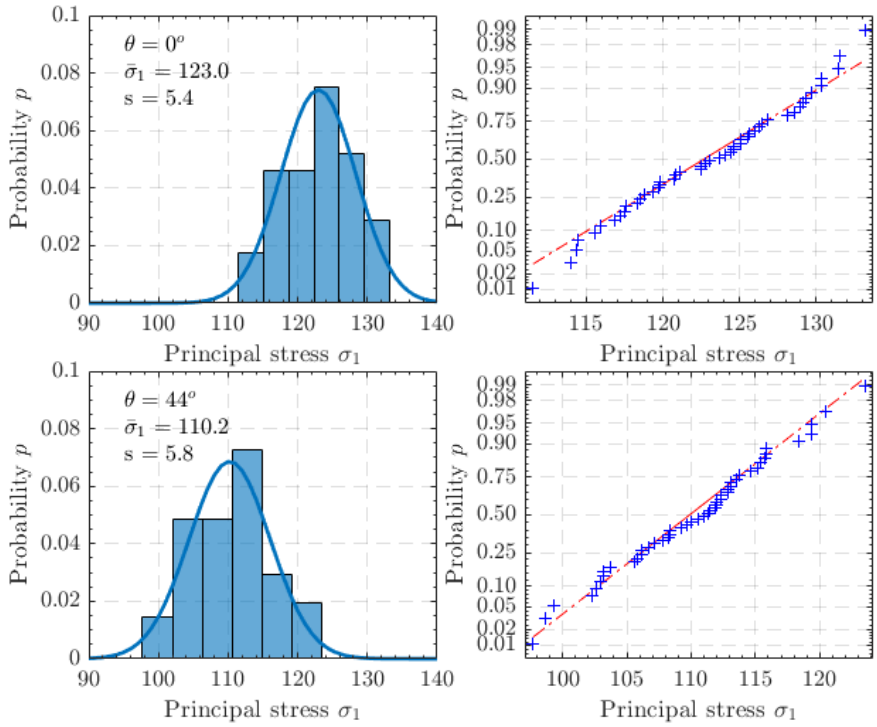

Figure A.2: Histograms and normal probability plots at $\theta = 0$ and $\theta = 44^o$

Null hypothesis significance testing is used to verify whether or not the RVEs tend to yield – on average – a lower principal stress when oriented at 44^o. Normality of the samples was tested via histograms and normal probability plots. The histograms were built per the procedure in (Dekking et al., 2005, pp. 189-190). The number of bins is given by (Dekking et al., 2005, p. 211):

$$m = 1 + 3.3 \log_{10}(n),$$

where n is the sample size. Despite showing good agreement, histograms may spur undesired artifacts by discretizing the data into bins. Thus, normal probability plots were used in tandem. Let $\bar{Y}_1$ and $\bar{Y}_2$ be random variables representing $\bar{\sigma}_1$ at $\theta = 0^o$ and $\theta = 44^o$, respectively. Fig. 1.2 and the central limit theorem show that $\bar{Y}_1$ and $\bar{Y}_2$ are well approximated by normal distributions:

$$\bar{Y}_1 \sim \mathrm{N}(\mu_1, \sigma_1^2/n_1),$$
$$\bar{Y}_2 \sim \mathrm{N}(\mu_2, \sigma_2^2/n_2).$$

Here, μ_i and σ_i are unknown population means and standard deviations and n_i are the sample sizes. The goal is to test whether $\bar{Y}_1$ and $\bar{Y}_2$ stem from the same

population despite changing θ. In terms of the null and alternate hypothesis:

$$\mathbf{H_0} : \mu_1 = \mu_2.$$
$$\mathbf{H_1} : \mu_1 \neq \mu_2.$$

The assumption of normality of $\bar{Y}_1$ and $\bar{Y}_2$ sanctions the use of Welch's t-test to verify $\mathbf{H}_0$ (Dekking et al., 2005, p. 400). Welch's t-test is a modification of the Student's t-test to see if two sample means are significantly different. t-tests typically test whether a sample mean deviates from some previously specified value. Instead, Welch's t-test introduces a Studentized difference of means:

$$T = \frac{\bar{Y}_1 - \bar{Y}_2}{\sqrt{\frac{s_1^2}{n_1} + \frac{s_2^2}{n_2}}},$$

where s_i and n_i are the samples' standard deviations and sizes. T follows a Student t-distribution with $\mu = 0$[1]. and number of degrees of freedom given by

$$\text{d.f.} = \frac{(\bar{s}_1 + \bar{s}_2)^2}{\frac{\bar{s}_1^2}{n_1 - 1} + \frac{\bar{s}_2^2}{n_2 - 1}},$$

where $\bar{s}_1 = s_1^2/n_1$ and $\bar{s}_2 = s_2^2/n_2$. The value of T realized from the current sample is called the t-statistic and is used to decide whether to reject $\mathbf{H}_0$. It is

$$t = \frac{\bar{y}_1 - \bar{y}_2}{\sqrt{\frac{s_1^2}{n_1} + \frac{s_2^2}{n_2}}},$$

where $\bar{y}_1 = \bar{\sigma}_1(\theta = 0^o)$ and $\bar{y}_2 = \bar{\sigma}_1(\theta = 44^o)$. If $\mathbf{H_0}$ is true, then the probability of getting a value at least as extreme[2] as the t-statistic is given by the p-value:

$$p = \mathrm{P}(T < |t|) + \mathrm{P}(T > |t|) = 2\mathrm{P}(T < |t|),$$

which is tantamount to the probability of falling outside of the $100 \cdot (1 - p)\%$ confidence interval for the mean of T. Setting the so-called significance level at a conservative value of $\alpha = 0.05$, the aforementioned calculations are performed:

$$t = \frac{123.0 - 110.2}{\sqrt{\frac{5.4^2}{48} + \frac{5.8^2}{48}}} = 11.14,$$
$$\text{d.f.} = \frac{(0.60 + 0.71)^2}{\frac{0.60^2}{48 - 1} + \frac{0.71^2}{48 - 1}} = 93.4,$$
$$p = 2\mathrm{P}(T < |t|) = 7.9 \cdot 10^{-17}.$$

The p-value is much lower than the significance level: $p \ll \alpha$. Therefore, $\mathbf{H}_0$ is rejected in favor of $\mathbf{H}_1$ at the $\alpha = 0.05$ significance level with $p = 7.9 \cdot 10^{-19}$.

[1] The random variable T assumes that $\mathbf{H}_0$ is true, thus $\mu = 0$.

[2] Extreme means far from what would be expected if $\mathbf{H_0}$ is true.

Appendix B

Proof: Prescribed Force

As stated in subsection 3.1.2, the derivations required to prove (3.21) are present here. Consider forces $\mathbf{f}_2$ and $\mathbf{f}_4$ on nodes 2 and 4 in Fig. 3.1. Equation (3.21) is

$$\int_{\Gamma_{\mathrm{R}}} \mathbf{t}\,\mathrm{d}\,\Gamma = \mathbf{f}_2 \text{ and } \int_{\Gamma_{\mathrm{T}}} \mathbf{t}\,\mathrm{d}\,\Gamma = \mathbf{f}_4. \tag{B.1}$$

Per (Kouznetsova et al., 2010, p. 13), the macroscopic stress tensor is given by

$$\bar{\boldsymbol{\Sigma}} = \frac{1}{|\Omega_\square|}\int_{\Gamma_\square} \mathbf{t} \otimes (\mathbf{x} - \bar{\mathbf{x}})\,\mathrm{d}\,\Gamma \tag{B.2}$$

(B.2) is rewritten per the criterion of anti-periodicity of tractions in (2.21) as

$$\begin{aligned}\bar{\boldsymbol{\Sigma}} &= \frac{1}{|\Omega_\square|}\left(\int_{\Gamma_\square^+} \mathbf{t} \otimes (\mathbf{x} - \bar{\mathbf{x}})\,\mathrm{d}\,\Gamma + \int_{\Gamma_\square^+} \mathbf{t}(\varphi_{\mathrm{per}}(\mathbf{x})) \otimes (\varphi_{\mathrm{per}}(\mathbf{x}) - \bar{\mathbf{x}})\,\mathrm{d}\,\Gamma\right)\\ &= \frac{1}{|\Omega_\square|}\int_{\Gamma_\square^+} \mathbf{t} \otimes (\mathbf{x} - \varphi_{\mathrm{per}}(\mathbf{x}))\,\mathrm{d}\,\Gamma.\end{aligned}$$

Substituting the dimensions shown in Fig. 3.1 into the aforementioned yields

$$\begin{aligned}\bar{\boldsymbol{\Sigma}} &= \frac{1}{|\Omega_\square|}\left(\int_{\Gamma_{\mathrm{R}}} \begin{Bmatrix} t_{\mathrm{x}} \\ t_{\mathrm{y}} \end{Bmatrix} \otimes \begin{Bmatrix} \Delta x \\ 0 \end{Bmatrix} \mathrm{d}\,y + \int_{\Gamma_{\mathrm{T}}} \begin{Bmatrix} t_{\mathrm{x}} \\ t_{\mathrm{y}} \end{Bmatrix} \otimes \begin{Bmatrix} 0 \\ \Delta y \end{Bmatrix} \mathrm{d}\,x\right)\\ &= \frac{1}{|\Omega_\square|}\begin{bmatrix} \Delta x \int_{\Gamma_{\mathrm{R}}} t_{\mathrm{x}}\,\mathrm{d}\,y & \Delta y \int_{\Gamma_{\mathrm{T}}} t_{\mathrm{x}}\,\mathrm{d}\,x \\ \Delta x \int_{\Gamma_{\mathrm{R}}} t_{\mathrm{y}}\,\mathrm{d}\,y & \Delta y \int_{\Gamma_{\mathrm{T}}} t_{\mathrm{y}}\,\mathrm{d}\,x \end{bmatrix}\end{aligned} \tag{B.3}$$

The macroscopic stress tensor also equals to (Kouznetsova et al., 2010, p. 21):

$$\bar{\boldsymbol{\Sigma}} = \frac{1}{|\Omega_\square|}\sum_{i=1,2,4} \mathbf{f}_i \otimes (\mathbf{x}_i - \bar{\mathbf{x}}). \tag{B.4}$$

Again, substituting the dimensions from Fig. 3.1 into (B.4) results in

$$\begin{aligned}\bar{\boldsymbol{\Sigma}} &= \frac{1}{|\Omega_\square|}\left(\begin{Bmatrix} f_{\mathrm{x}1} \\ f_{\mathrm{y}1} \end{Bmatrix} \otimes \begin{Bmatrix} -a \\ -b \end{Bmatrix} + \begin{Bmatrix} f_{\mathrm{x}2} \\ f_{2\mathrm{y}} \end{Bmatrix} \otimes \begin{Bmatrix} \Delta x - a \\ -b \end{Bmatrix} + \begin{Bmatrix} f_{\mathrm{x}4} \\ f_{\mathrm{y}4} \end{Bmatrix} \otimes \begin{Bmatrix} -a \\ \Delta y - b \end{Bmatrix}\right) \\ &= \frac{1}{|\Omega_\square|}\begin{bmatrix} -a(f_{\mathrm{x}1} + f_{\mathrm{x}2} + f_{\mathrm{x}4}) + \Delta x f_{\mathrm{x}2} & -b(f_{\mathrm{x}1} + f_{\mathrm{x}2} + f_{\mathrm{x}4}) + \Delta y f_{\mathrm{x}4} \\ -a(f_{\mathrm{y}1} + f_{\mathrm{y}2} + f_{\mathrm{y}4}) + \Delta x f_{\mathrm{y}2} & -b(f_{\mathrm{y}1} + f_{\mathrm{y}2} + f_{\mathrm{y}4}) + \Delta y f_{\mathrm{y}4} \end{bmatrix}\end{aligned}$$

Equilibrium shows that $f_{\mathrm{x}1} + f_{\mathrm{x}2} + f_{\mathrm{x}4} = 0$ and $f_{\mathrm{y}1} + f_{\mathrm{y}2} + f_{\mathrm{y}4} = 0$. Thus

$$\bar{\boldsymbol{\Sigma}} = \frac{1}{|\Omega_\square|}\begin{bmatrix} \Delta x f_{\mathrm{x}2} & \Delta y f_{\mathrm{x}4} \\ \Delta x f_{\mathrm{y}2} & \Delta y f_{\mathrm{y}4} \end{bmatrix} \tag{B.5}$$

Noting that $\Delta x \neq 0$ and $\Delta y \neq 0$ and equating (B.3) to (B.5) results in

$$\begin{aligned} \int_{\Gamma_{\mathrm{R}}} t_{\mathrm{x}}\,\mathrm{d}\,\Gamma = f_{\mathrm{x}2}, \qquad \int_{\Gamma_{\mathrm{R}}} t_{\mathrm{y}}\,\mathrm{d}\,\Gamma = f_{\mathrm{y}2}, \\ \int_{\Gamma_{\mathrm{T}}} t_{\mathrm{x}}\,\mathrm{d}\,\Gamma = f_{\mathrm{x}4}, \qquad \int_{\Gamma_{\mathrm{T}}} t_{\mathrm{y}}\,\mathrm{d}\,\Gamma = f_{\mathrm{y}4}. \end{aligned} \tag{B.6}$$

(B.6) is simplified to (3.21), thereby completing the proof. For brevity, $\mathbf{f}_2$ and $\mathbf{f}_4$ are now denoted $\mathbf{f}^+_{\mathrm{cor}}$ (which represents the sum of all corner forces on Γ^+):

$$\int_{\Gamma^+_\square} \mathbf{t}\,\mathrm{d}\,\Gamma = \mathbf{f}^+_{\mathrm{cor}} \tag{B.7}$$

Appendix C

Results: Principal Stresses

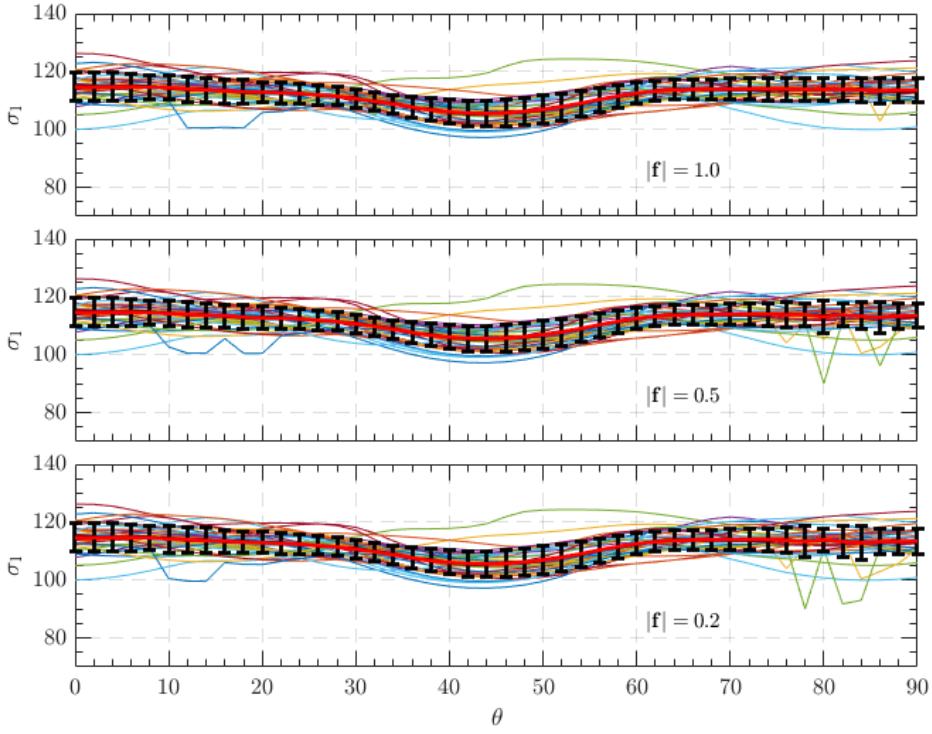

Figure C.1: Principal stress vs. orientation angle ($\texttt{cf\_} = 0.016$)

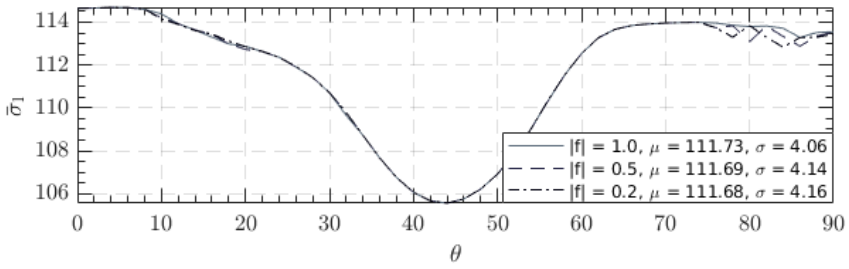

Figure C.2: Average principal stress vs. orientation angle ($\texttt{cf\_} = 0.016$)

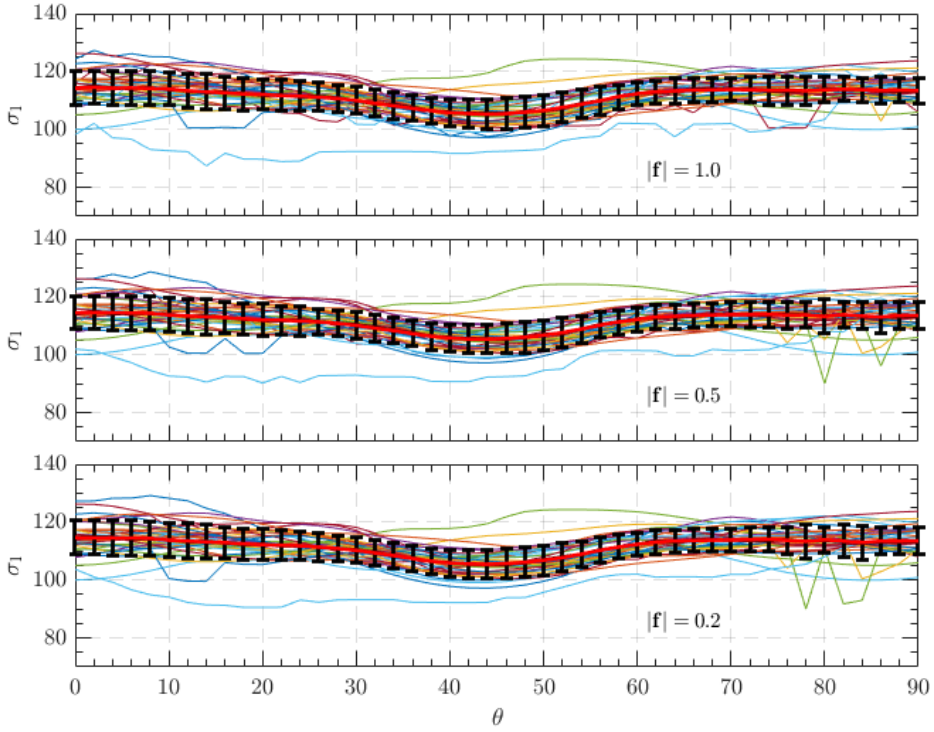

Figure C.3: Principal stress vs. orientation angle ($\texttt{cf\_} = 0.025$)

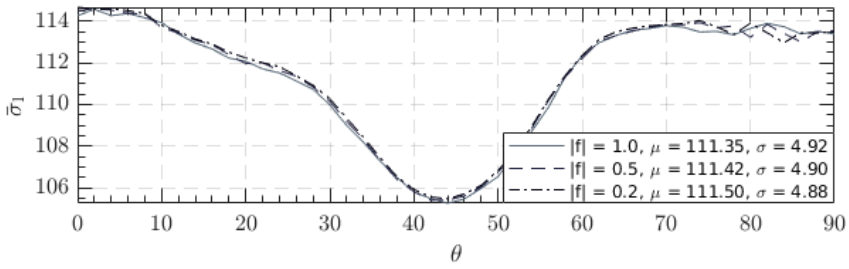

Figure C.4: Average principal stress vs. orientation angle ($\texttt{cf\_} = 0.025$)

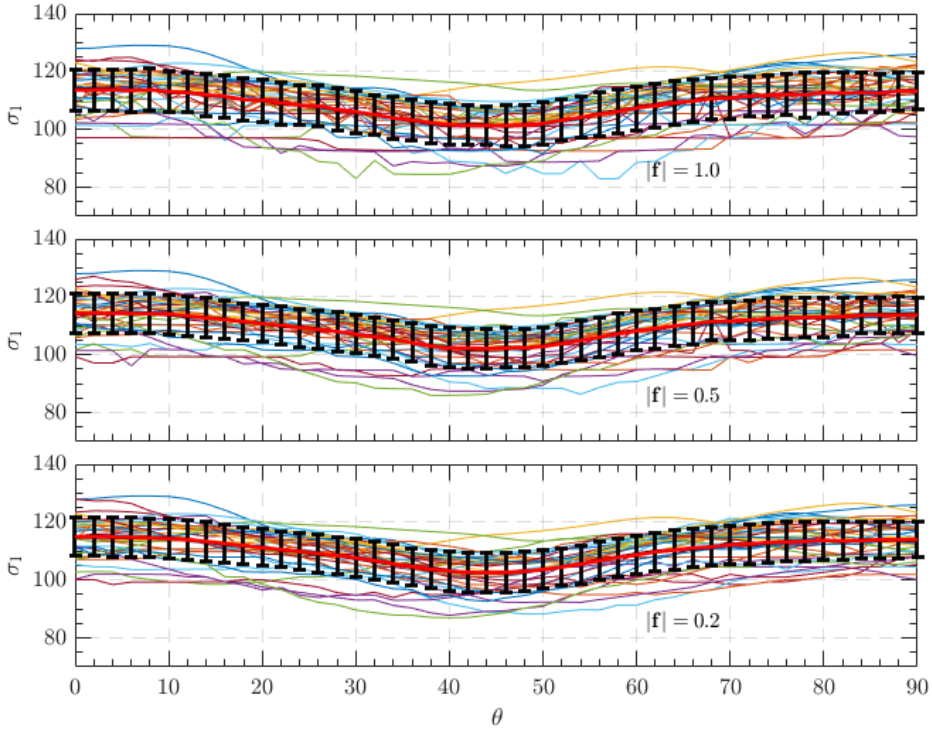

Figure C.5: Principal stress vs. orientation angle ($\texttt{cf\_} = 0.040$)

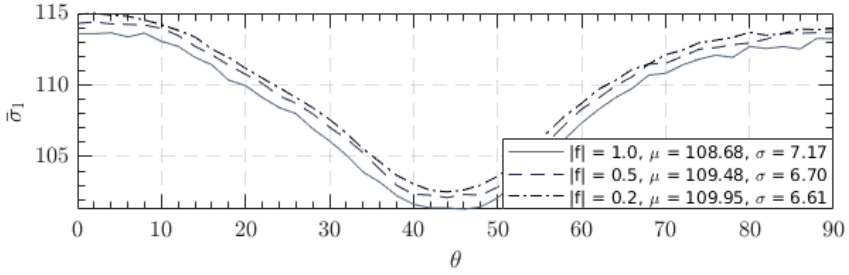

Figure C.6: Average principal stress vs. orientation angle ($\texttt{cf\_} = 0.040$)

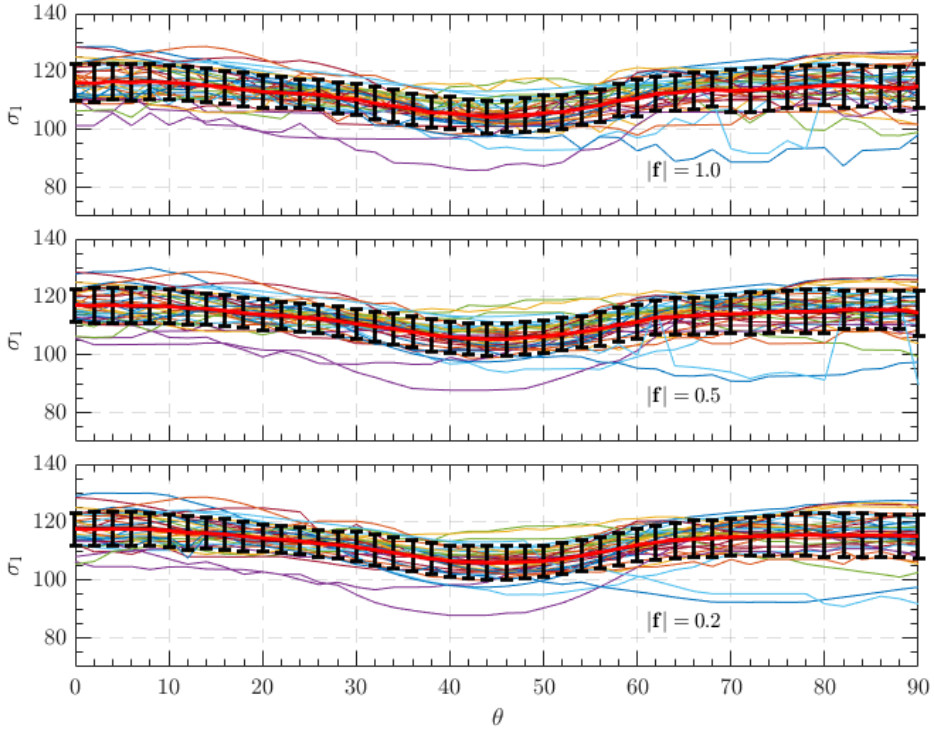

Figure C.7: Principal stress vs. orientation angle ($\texttt{cf\_} = 0.063$)

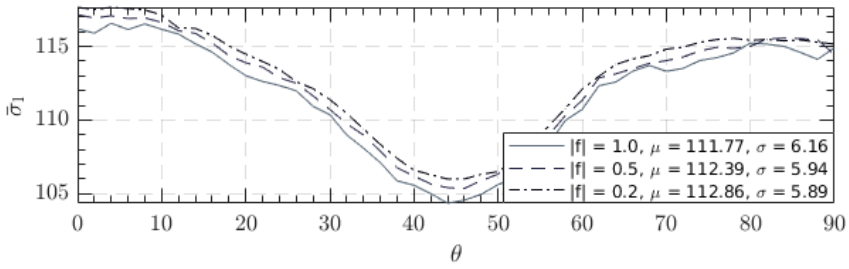

Figure C.8: Average principal stress vs. orientation angle ($\texttt{cf\_} = 0.063$)

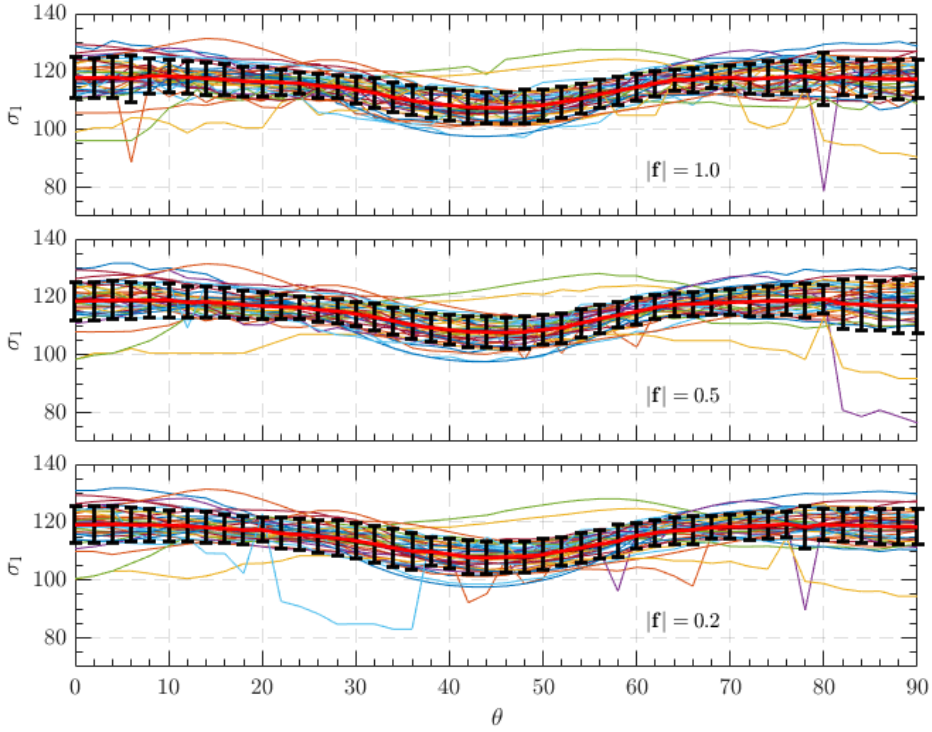

Figure C.9: Principal stress vs. orientation angle ($\texttt{cf\_} = 0.100$)

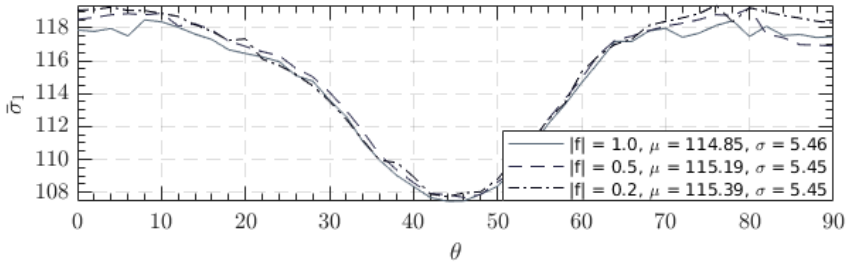

Figure C.10: Average principal stress vs. orientation angle ($\texttt{cf\_} = 0.100$)

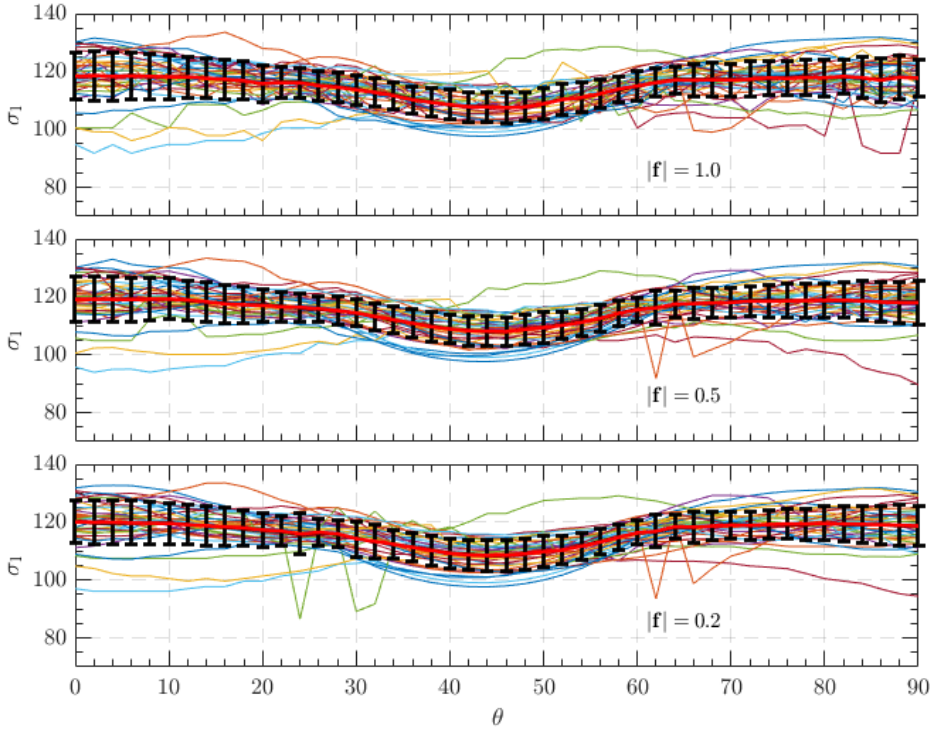

Figure C.11: Principal stress vs. orientation angle (`cf_` = 0.160)

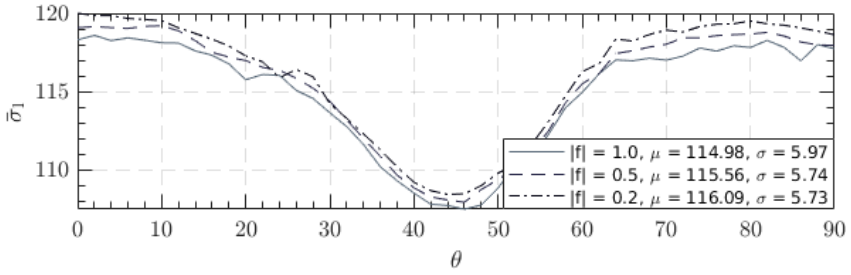

Figure C.12: Average principal stress vs. orientation angle (`cf_` = 0.160)

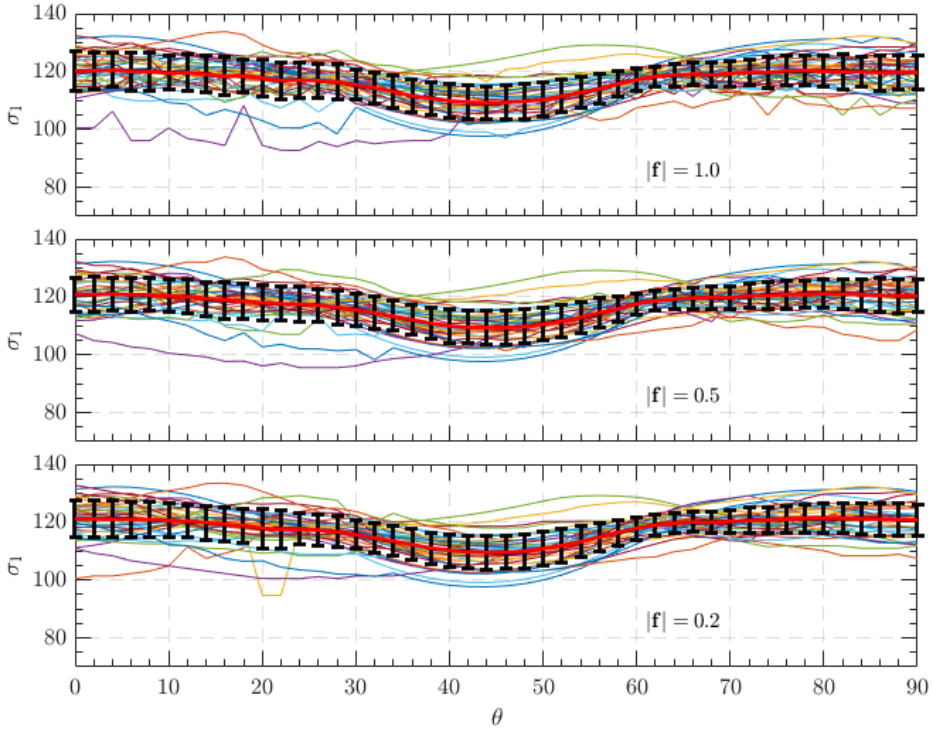

Figure C.13: Principal stress vs. orientation angle ($\texttt{cf\_} = 0.250$)

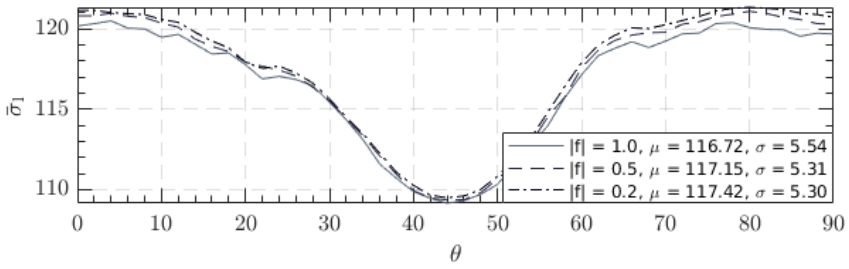

Figure C.14: Average principal stress vs. orientation angle ($\texttt{cf\_} = 0.250$)

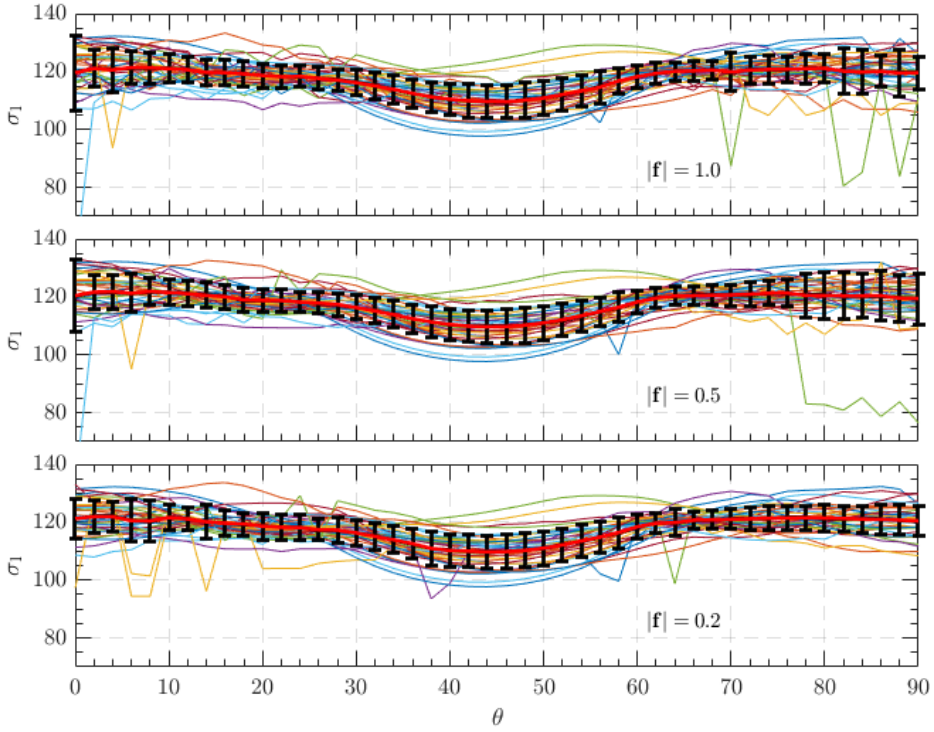

Figure C.15: Principal stress vs. orientation angle (`cf_` = 0.400)

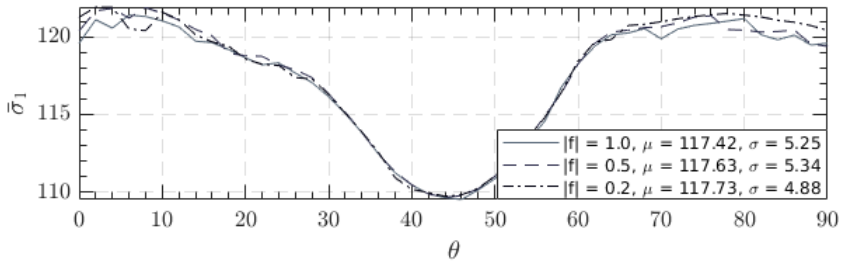

Figure C.16: Average principal stress vs. orientation angle (`cf_` = 0.400)

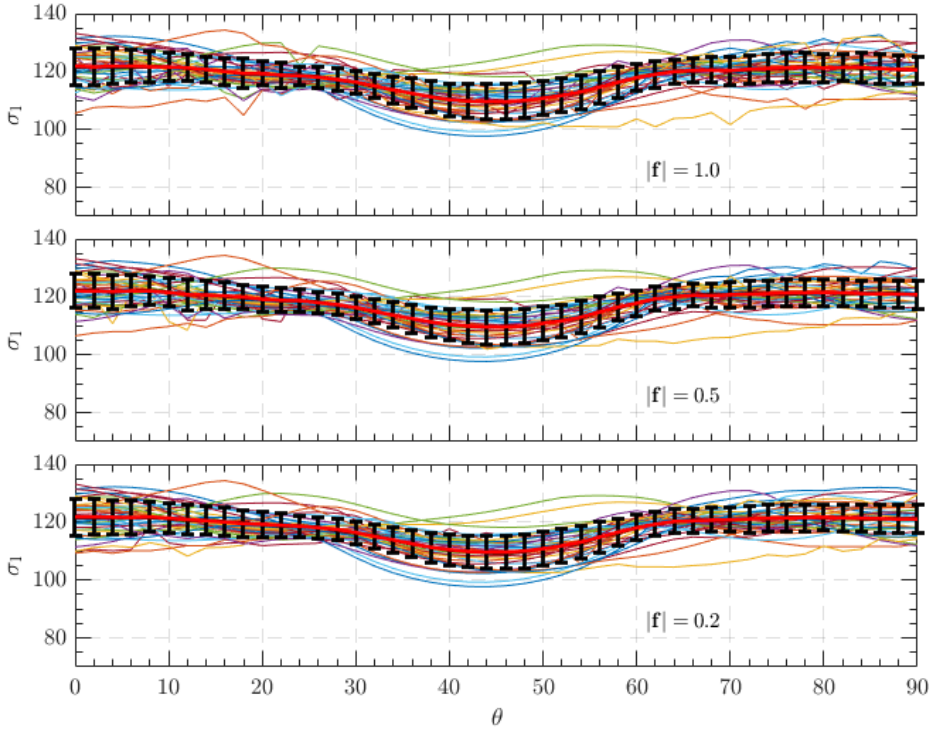

Figure C.17: Principal stress vs. orientation angle (`cf_` = 0.630)

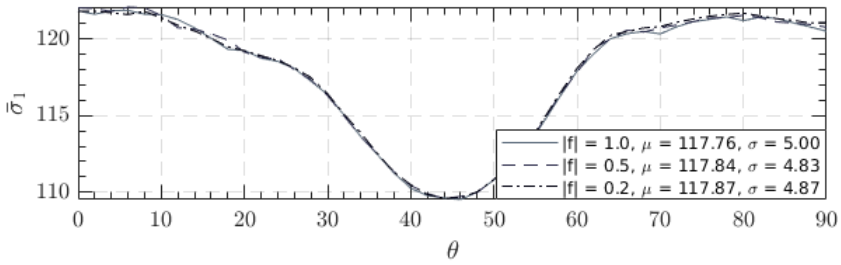

Figure C.18: Average principal stress vs. orientation angle (`cf_` = 0.630)

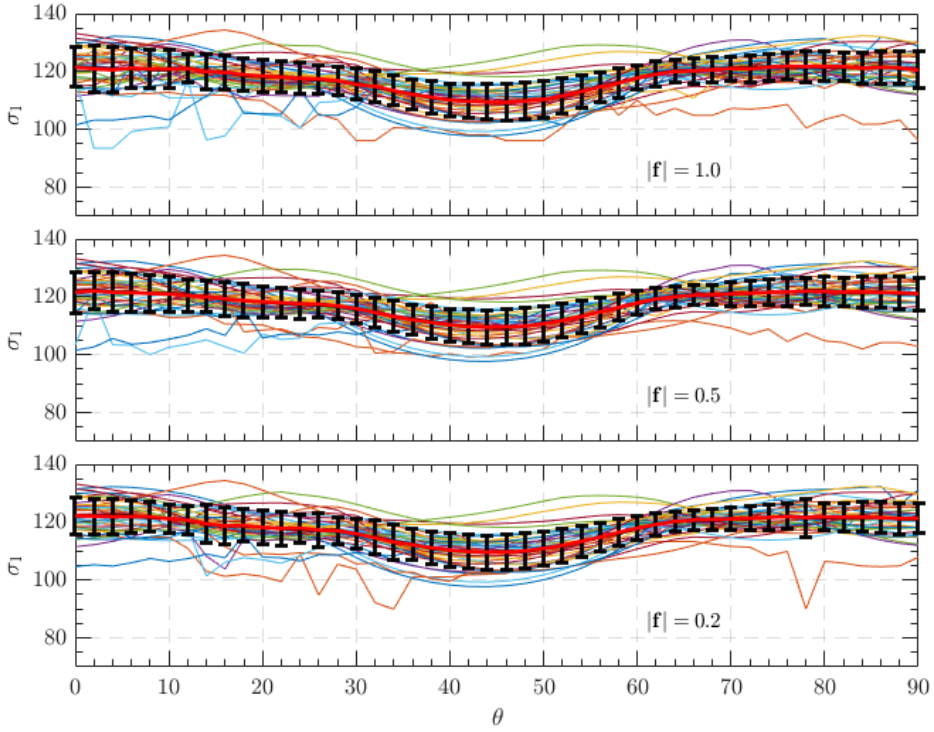

Figure C.19: Principal stress vs. orientation angle (`cf_` = 1.000)

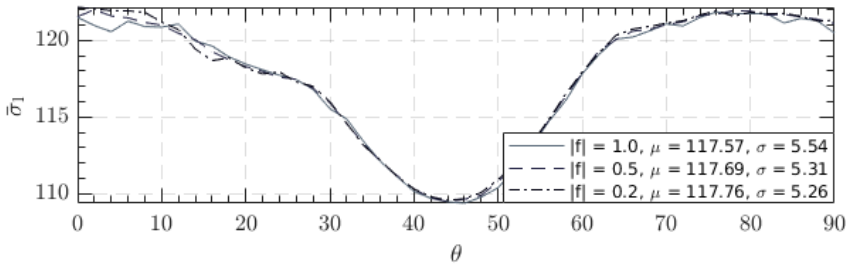

Figure C.20: Average principal stress vs. orientation angle (`cf_` = 1.000)

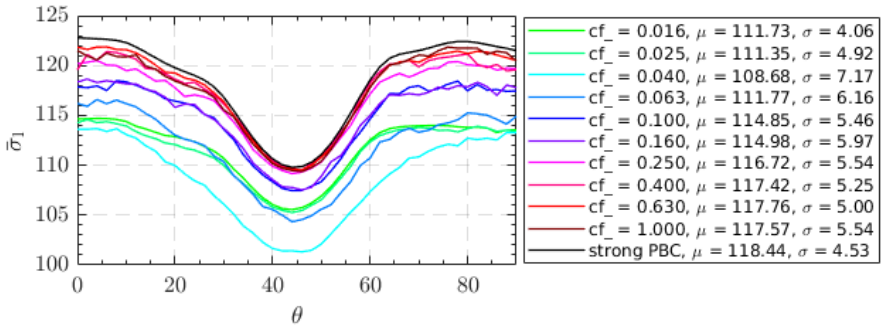

Figure C.21: Average principal stress vs. orientation angle ($|\mathbf{f}| = 1.0$)

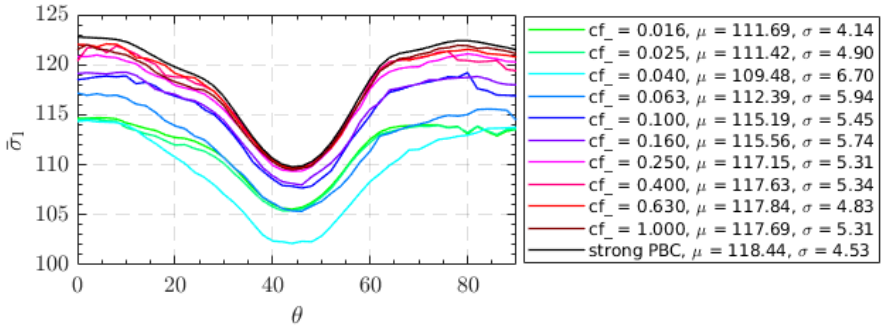

Figure C.22: Average principal stress vs. orientation angle ($|\mathbf{f}| = 0.5$)

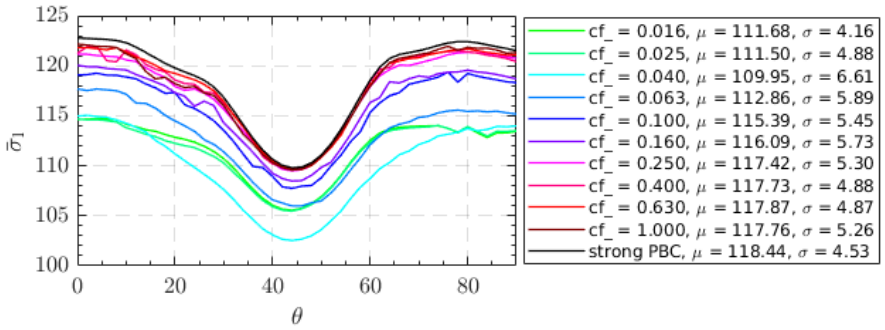

Figure C.23: Average principal stress vs. orientation angle ($|\mathbf{f}| = 0.2$)

Table C.1: Average principal stress and standard deviation per coarsening factor

Coarsening factor (cf_)	**Elements per $\mathcal{T}^{\mathbf{h}}$ face**	**Load size $\|\mathbf{f}\|$**	**Average stress μ**	**Average std. dev. σ**	$\max(\bar{\sigma}_1) - \min(\bar{\sigma}_1)$
0.016	1.0	1.0	111.73	4.06	9.14
		0.5	111.69	4.14	9.14
		0.2	111.68	4.16	9.14
0.025	1.1	1.0	111.35	4.92	9.32
		0.5	111.42	4.90	9.20
		0.2	111.50	4.88	9.21
0.040	2.2	1.0	108.68	7.17	12.36
		0.5	109.48	6.70	12.30
		0.2	109.95	6.61	12.51
0.063	3.8	1.0	111.77	6.16	12.25
		0.5	112.39	5.94	11.82
		0.2	112.86	5.89	11.69
0.100	6.0	1.0	114.85	5.46	11.03
		0.5	115.19	5.45	11.51
		0.2	115.39	5.45	11.63
0.160	9.3	1.0	114.98	5.97	11.11
		0.5	115.56	5.74	11.28
		0.2	116.09	5.73	11.57
0.250	13.9	1.0	116.72	5.54	11.34
		0.5	117.15	5.31	11.73
		0.2	117.42	5.30	11.85
0.400	20.3	1.0	117.42	5.25	11.87
		0.5	117.63	5.34	12.19
		0.2	117.73	4.88	12.18
0.630	28.0	1.0	117.76	5.00	12.34
		0.5	117.84	4.83	12.50
		0.2	117.87	4.87	12.20
1.000	38.1	1.0	117.57	5.54	12.47
		0.5	117.69	5.31	12.51
		0.2	117.76	5.26	12.59
PeriodicBC	N/A	1.0	118.44	4.53	12.99

Appendix D

Localization Modes at $\theta = 0^o$

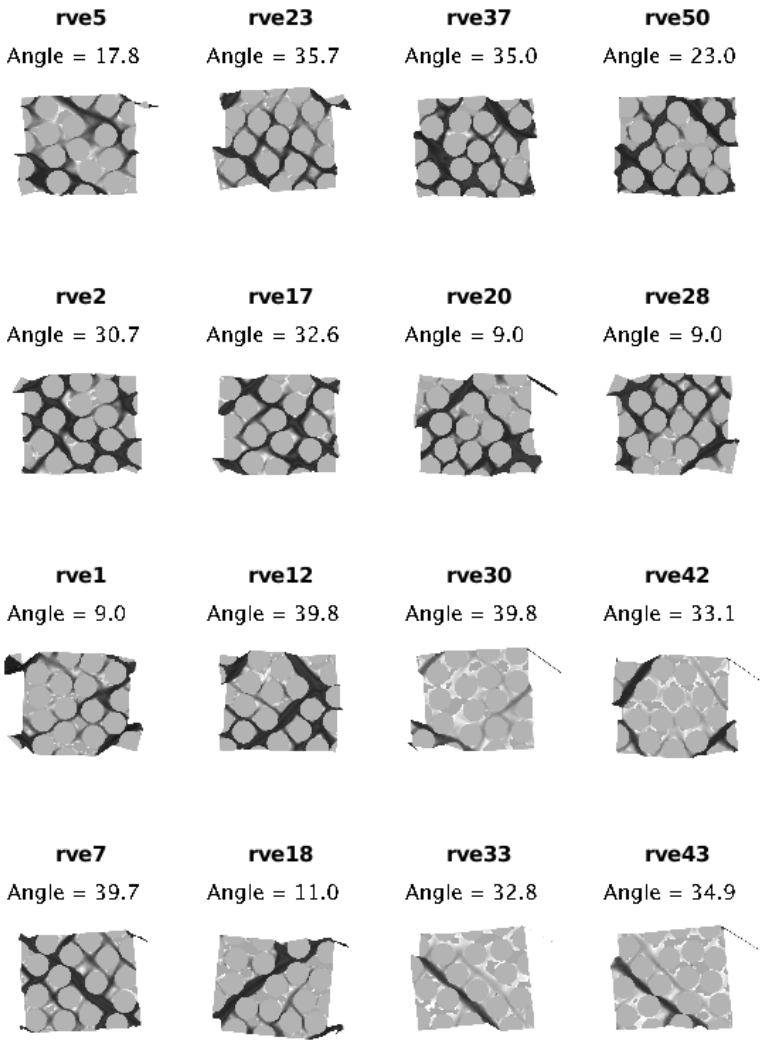

Figure D.1: Examples of localization modes at $\theta = 0^o$ ($\texttt{cf\_} = 0.016$)

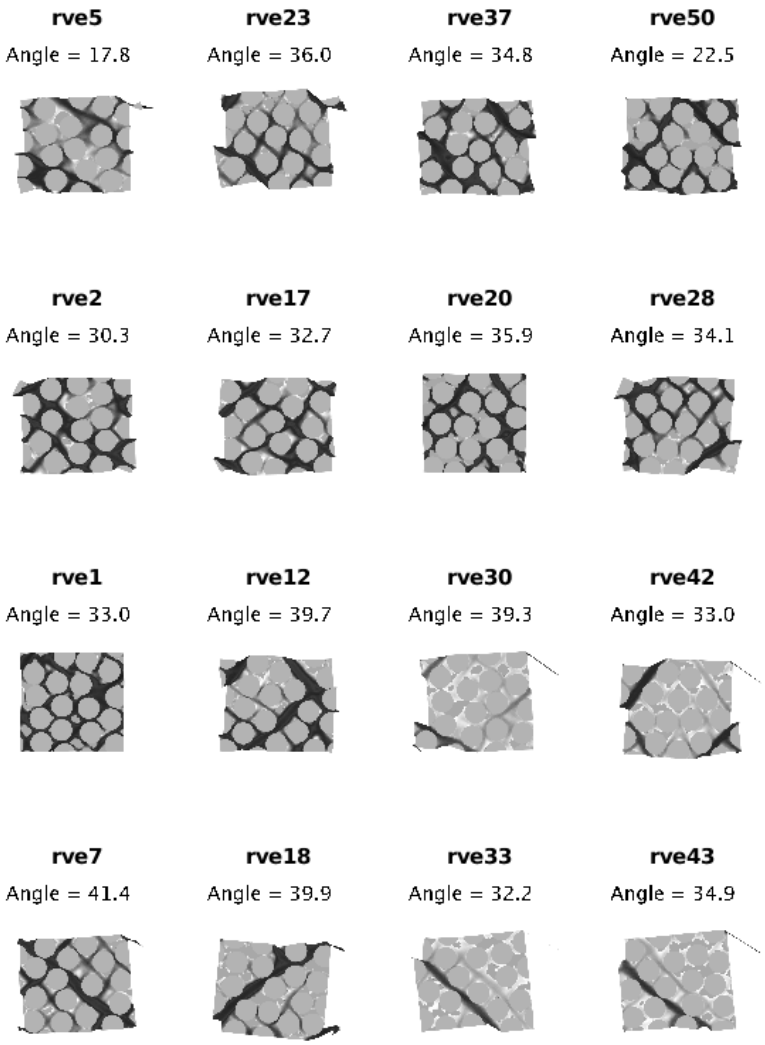

Figure D.2: Examples of localization modes at $\theta = 0^o$ ($\texttt{cf\_} = 0.025$)

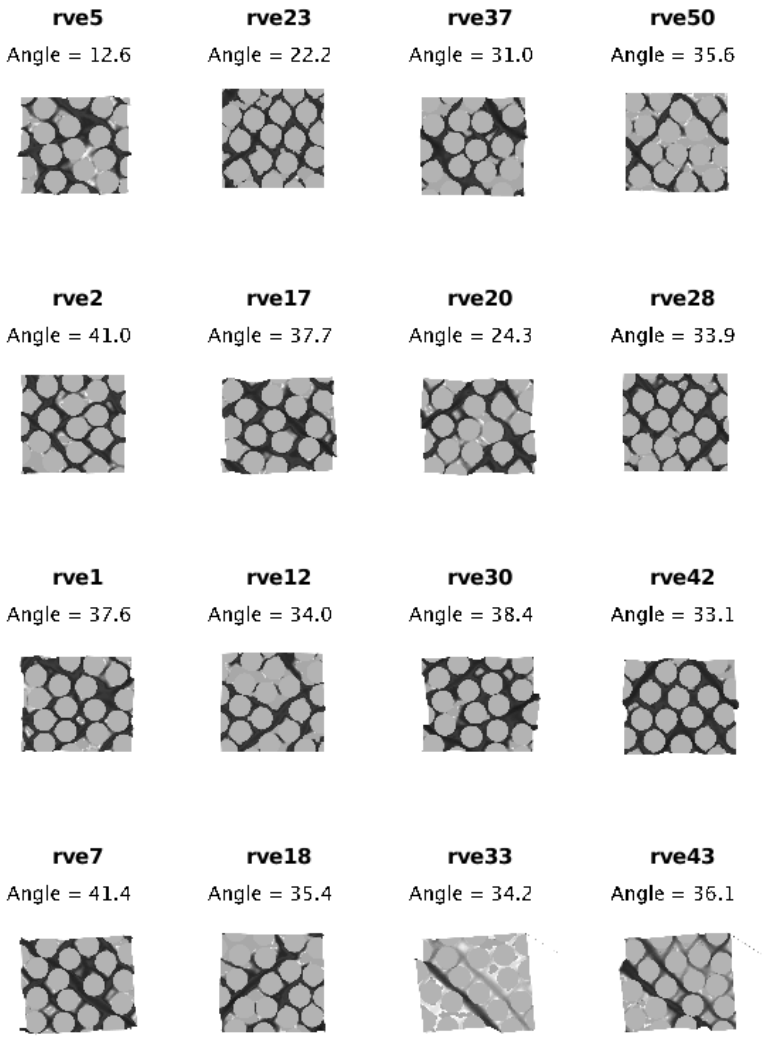

Figure D.3: Examples of localization modes at $\theta = 0^o$ ($\texttt{cf\_} = 0.040$)

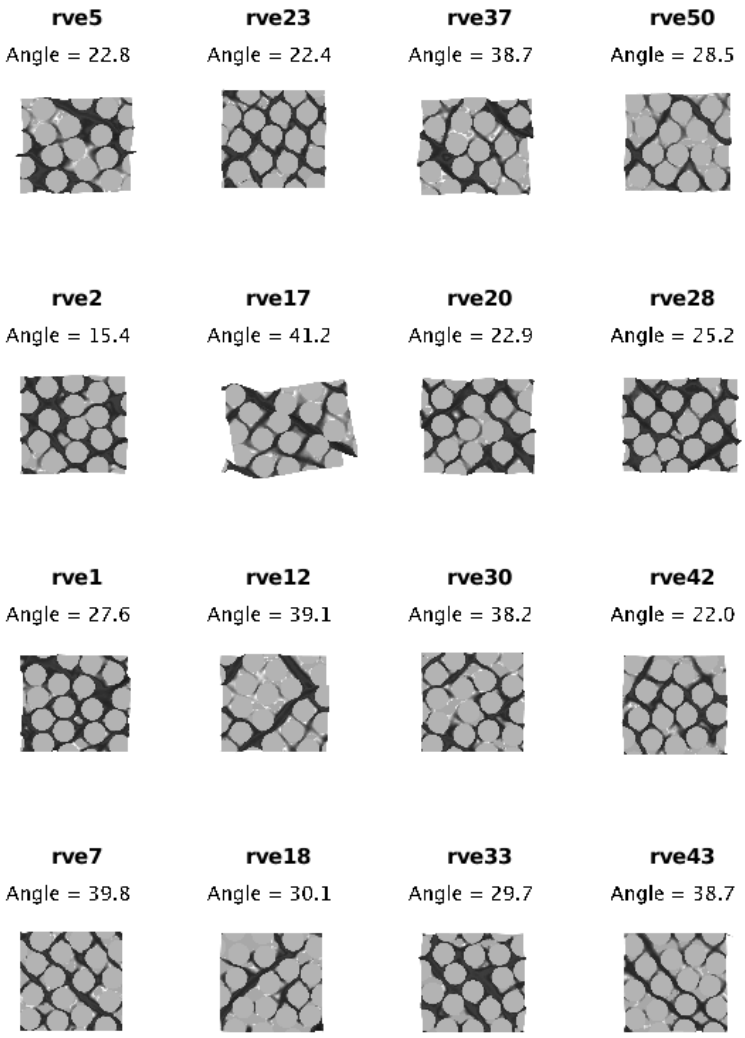

Figure D.4: Examples of localization modes at $\theta = 0^o$ ($\texttt{cf\_} = 0.063$)

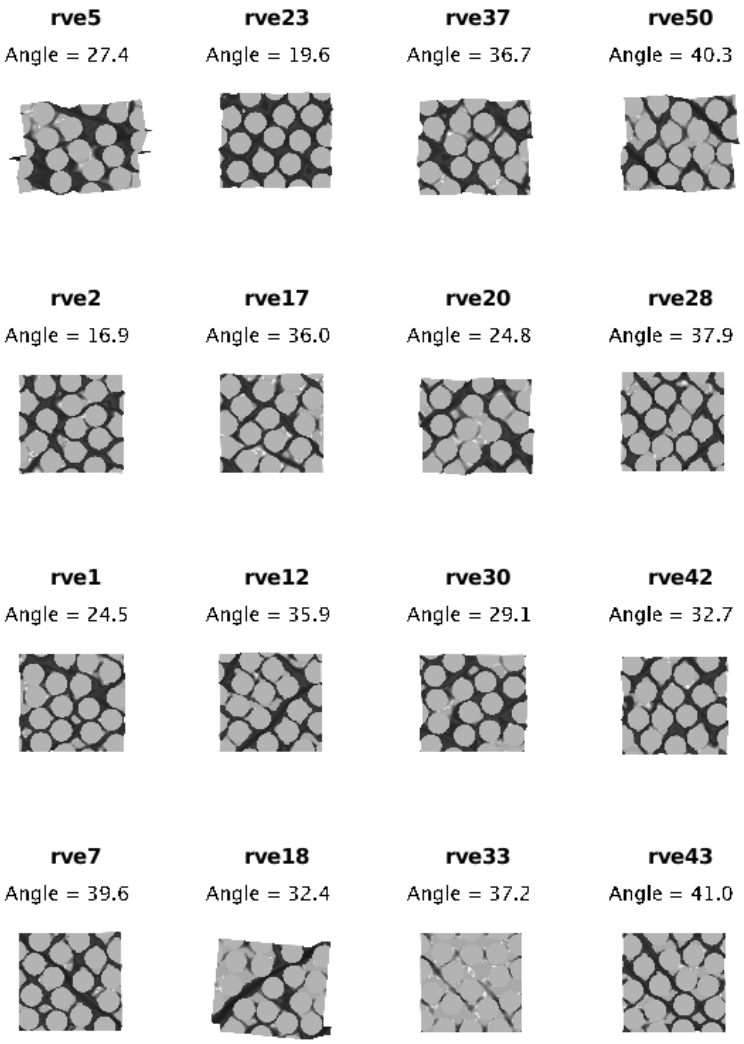

Figure D.5: Examples of localization modes at $\theta = 0^o$ ($\texttt{cf\_} = 0.100$)

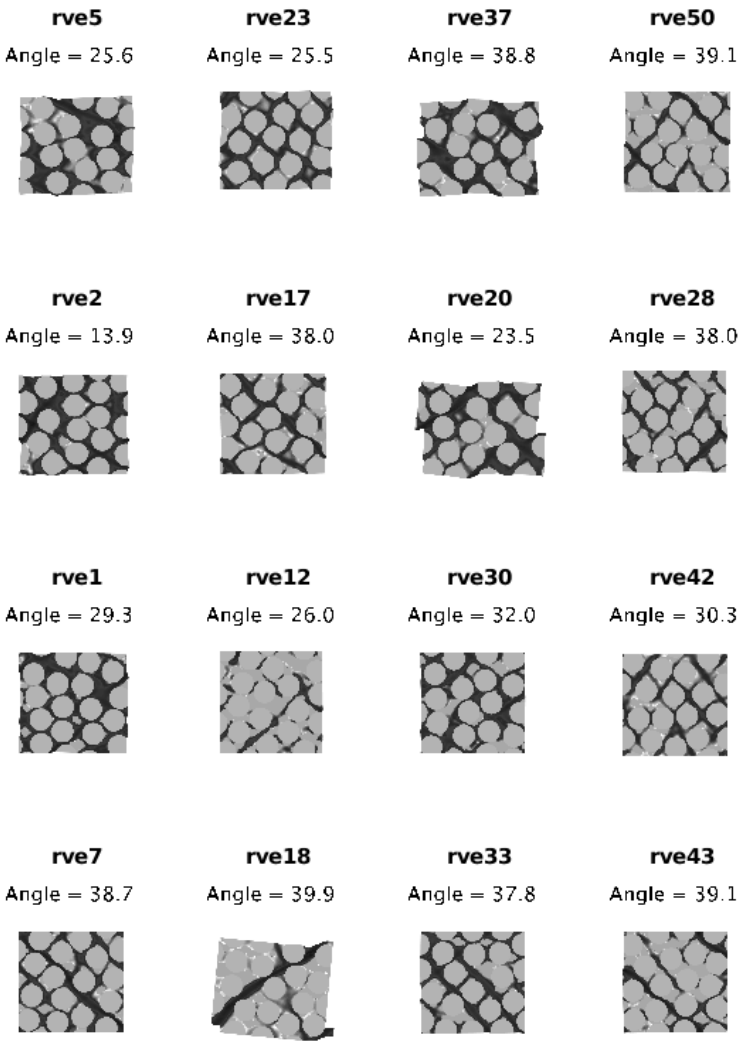

Figure D.6: Examples of localization modes at $\theta = 0^o$ ($\texttt{cf\_} = 0.160$)

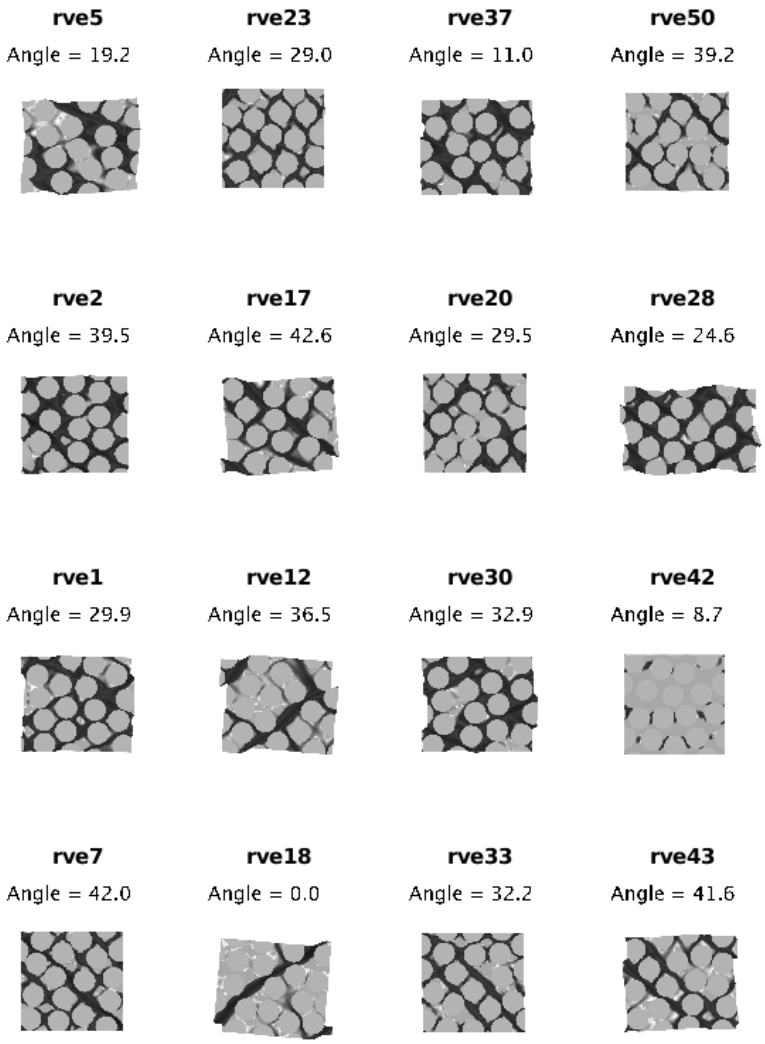

Figure D.7: Examples of localization modes at $\theta = 0^o$ ($\texttt{cf\_} = 0.250$)

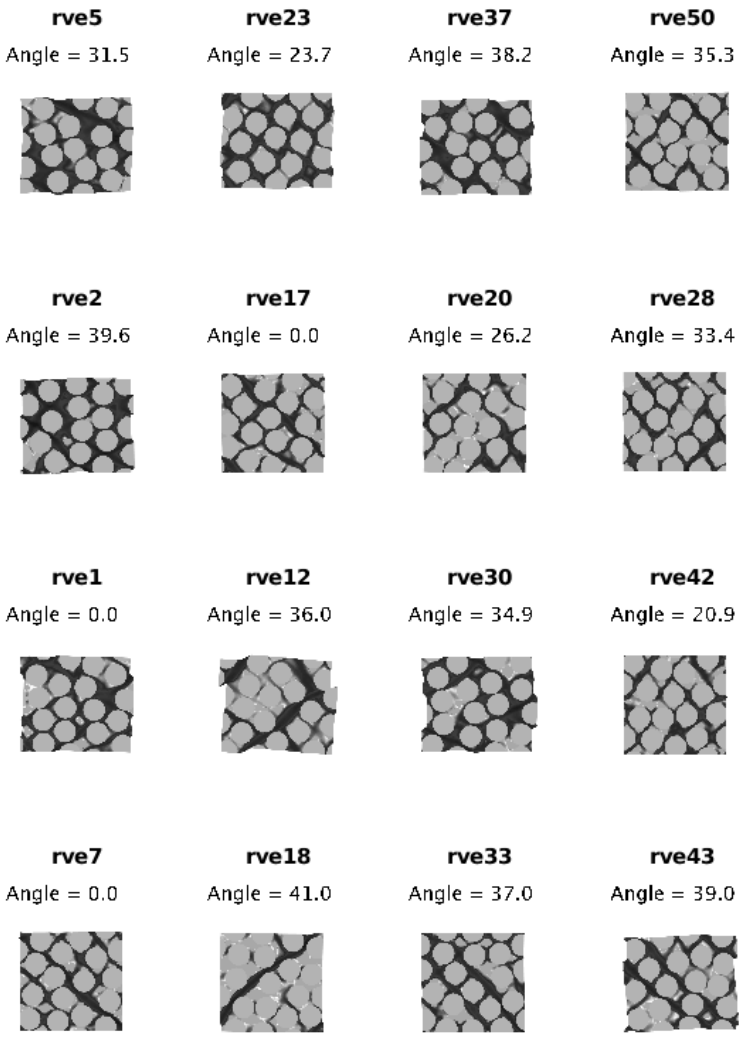

Figure D.8: Examples of localization modes at $\theta = 0^o$ ($\texttt{cf\_} = 0.400$)

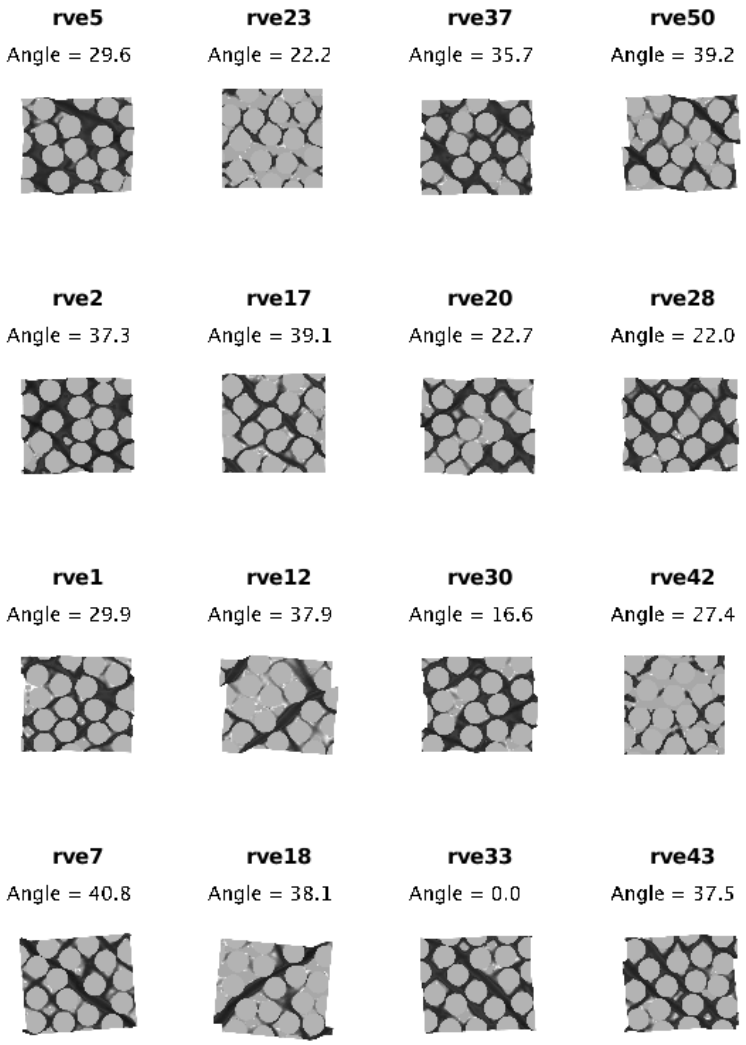

Figure D.9: Examples of localization modes at $\theta = 0^o$ ($\texttt{cf\_} = 0.630$)

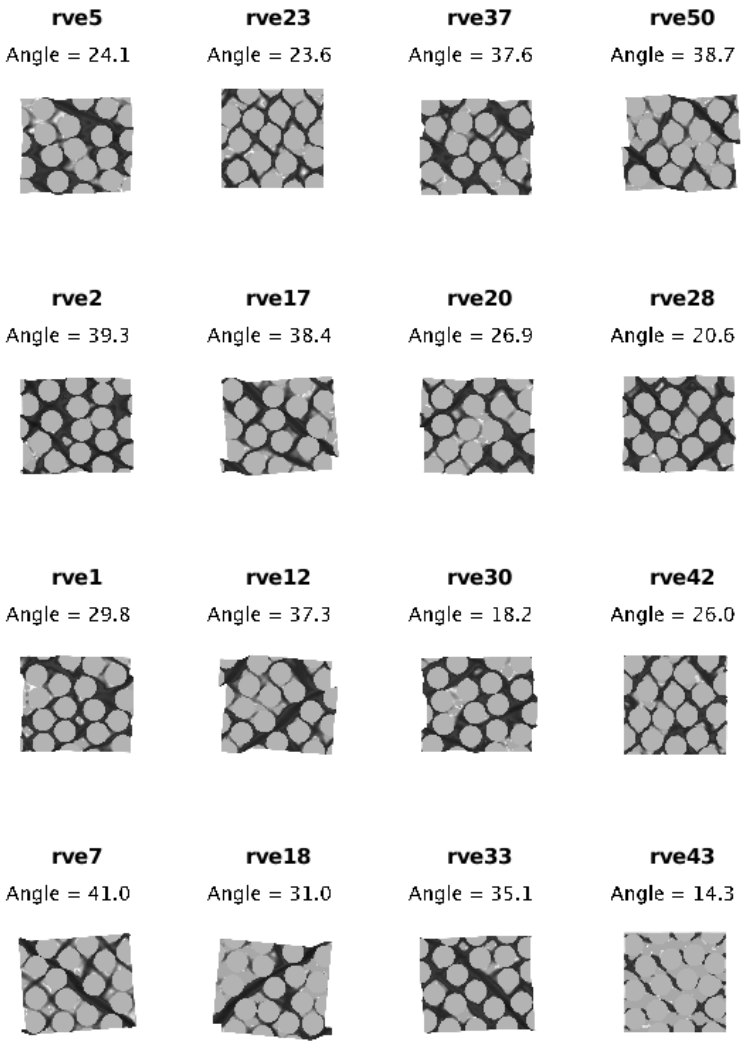

Figure D.10: Examples of localization modes at $\theta = 0^o$ ($\texttt{cf\_} = 1.000$)

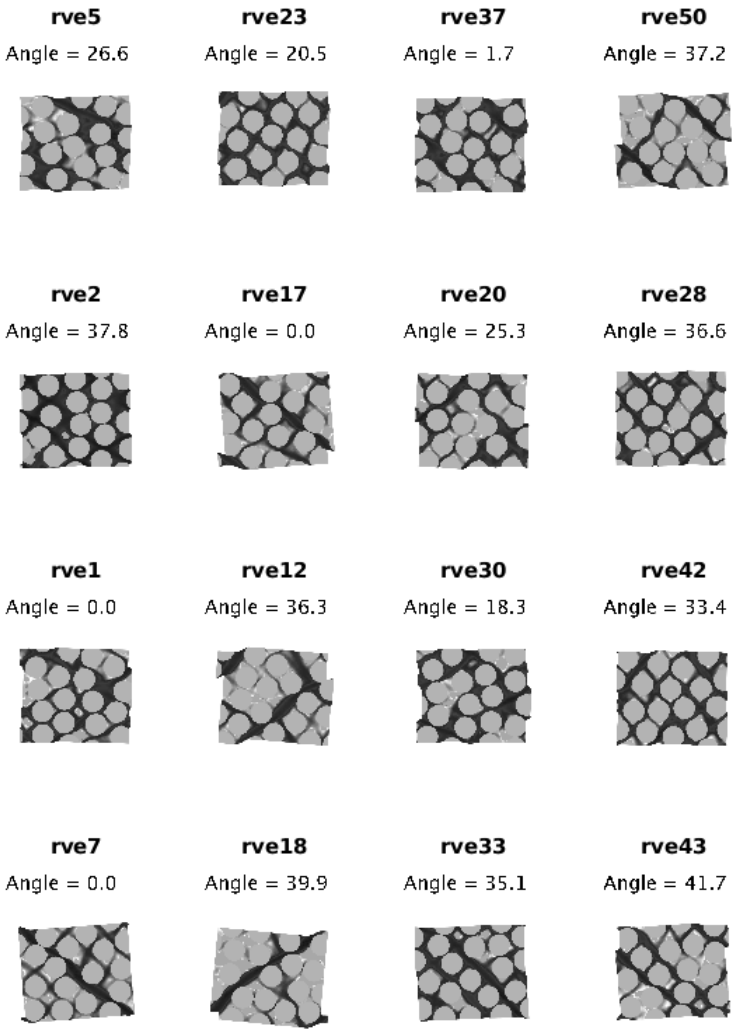

Figure D.11: Examples of localization modes at $\theta = 0^o$ (strong PBC)

Appendix E

Localization Modes at $\theta = 44^o$

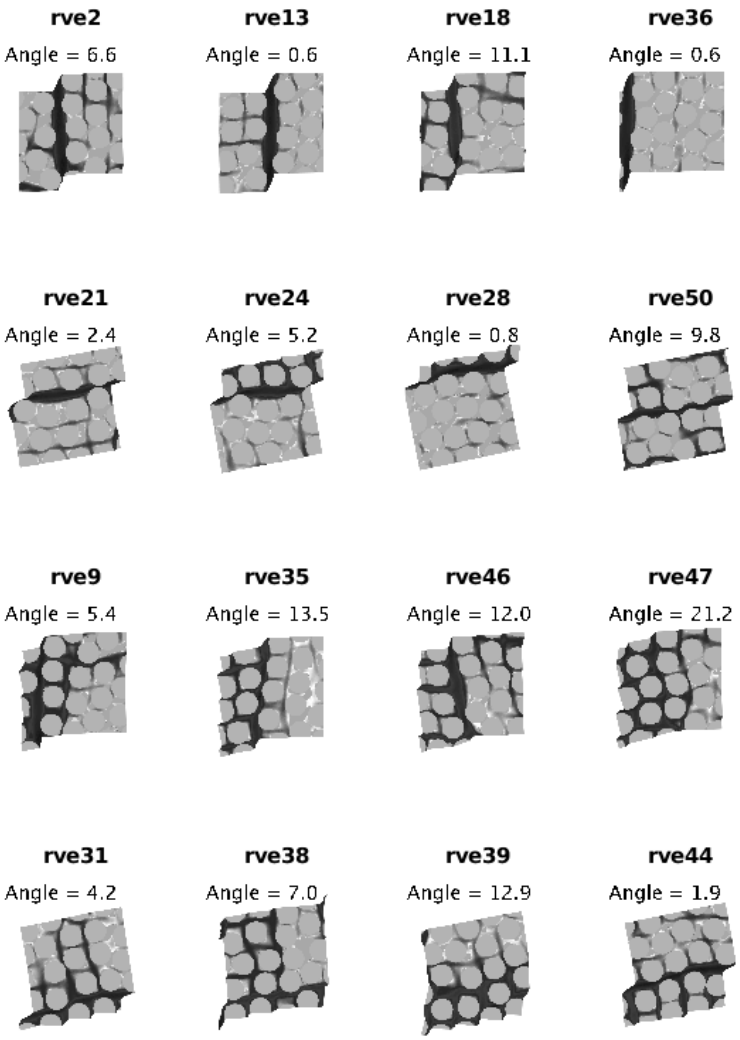

Figure E.1: Examples of localization modes at $\theta = 44^o$ ($\texttt{cf\_} = 0.016$)

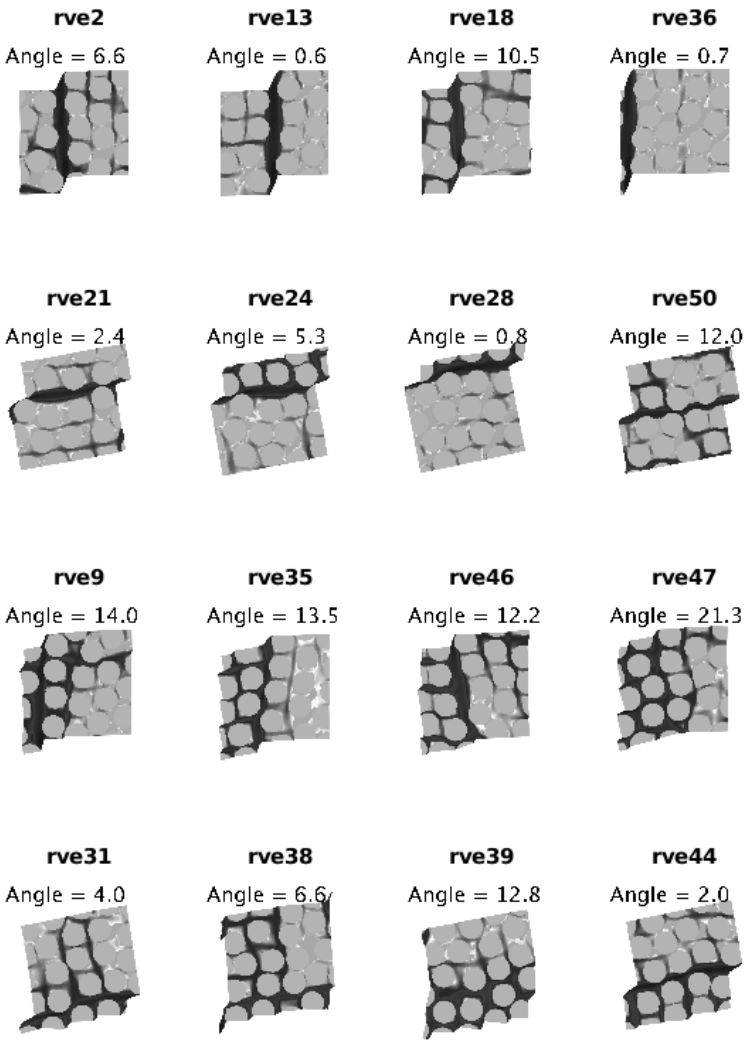

Figure E.2: Examples of localization modes at $\theta = 44^o$ ($\texttt{cf\_} = 0.025$)

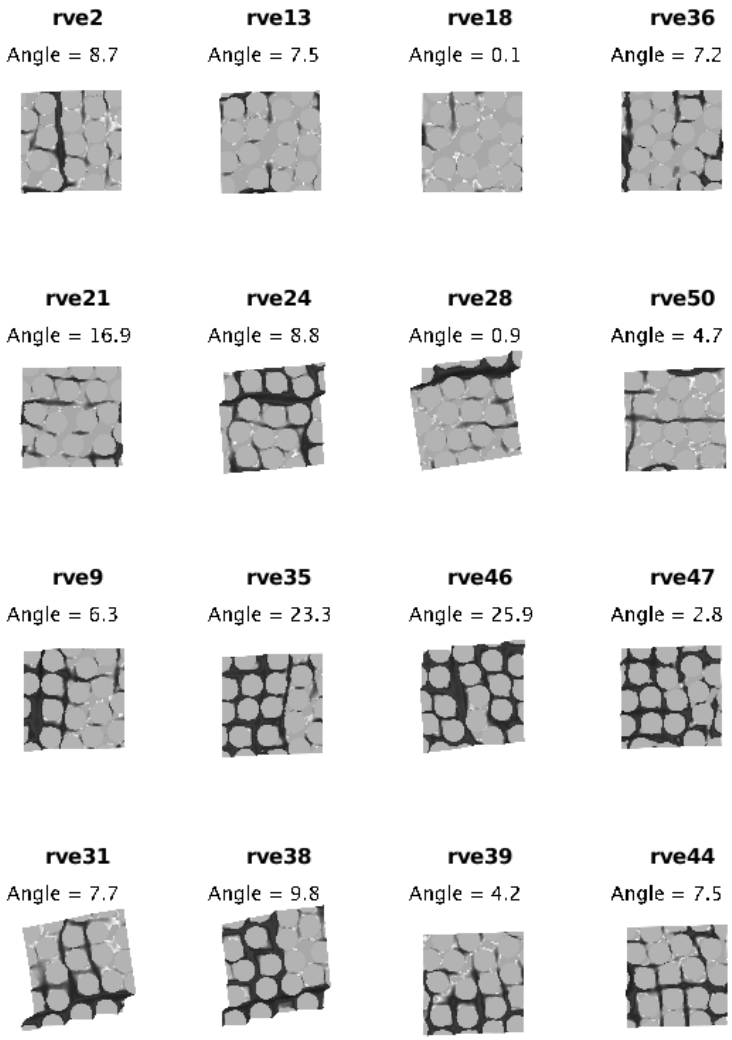

Figure E.3: Examples of localization modes at $\theta = 44^o$ ($\texttt{cf\_} = 0.040$)

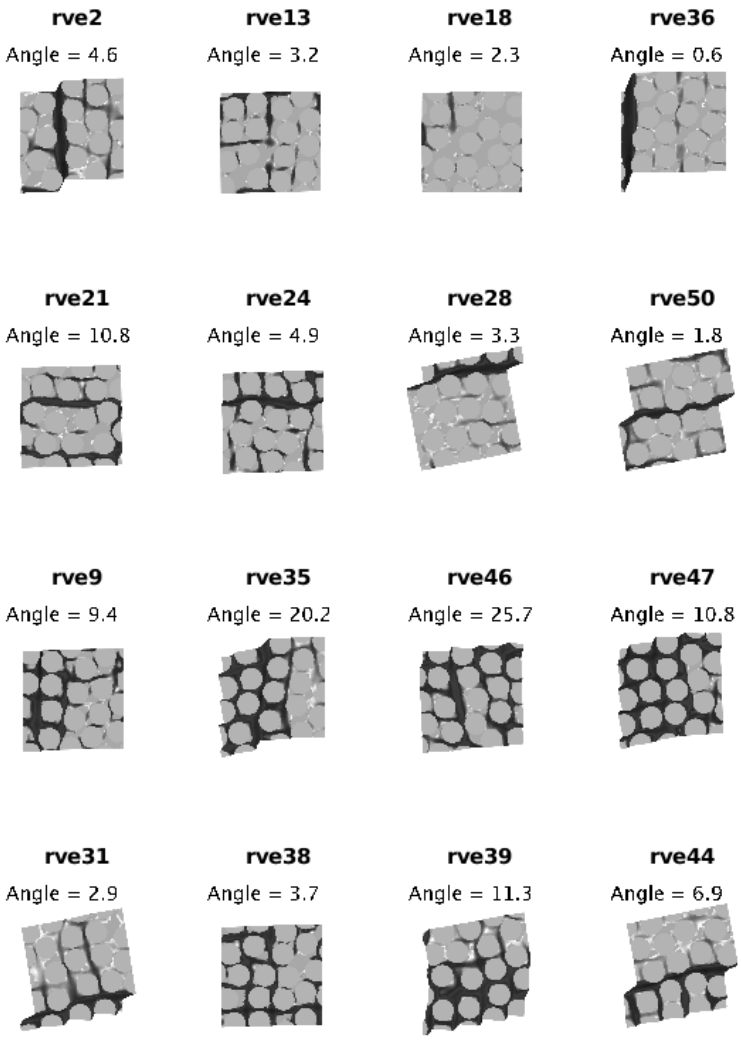

Figure E.4: Examples of localization modes at $\theta = 44^o$ ($\texttt{cf\_} = 0.063$)

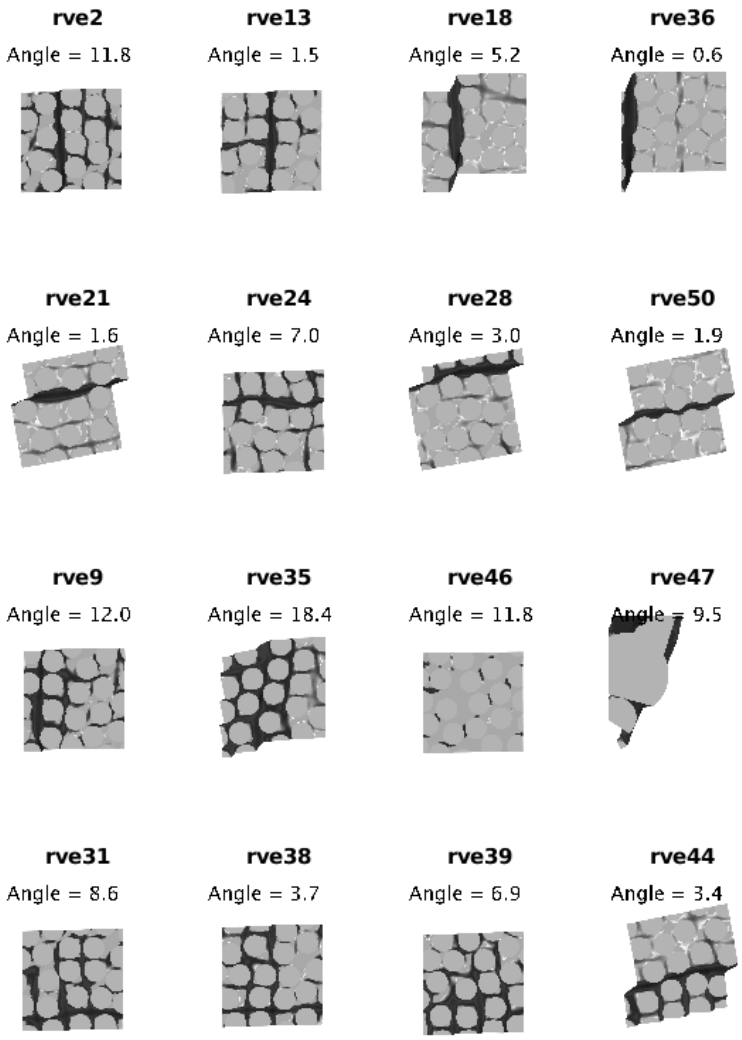

Figure E.5: Examples of localization modes at $\theta = 44^o$ (`cf_` = 0.100)

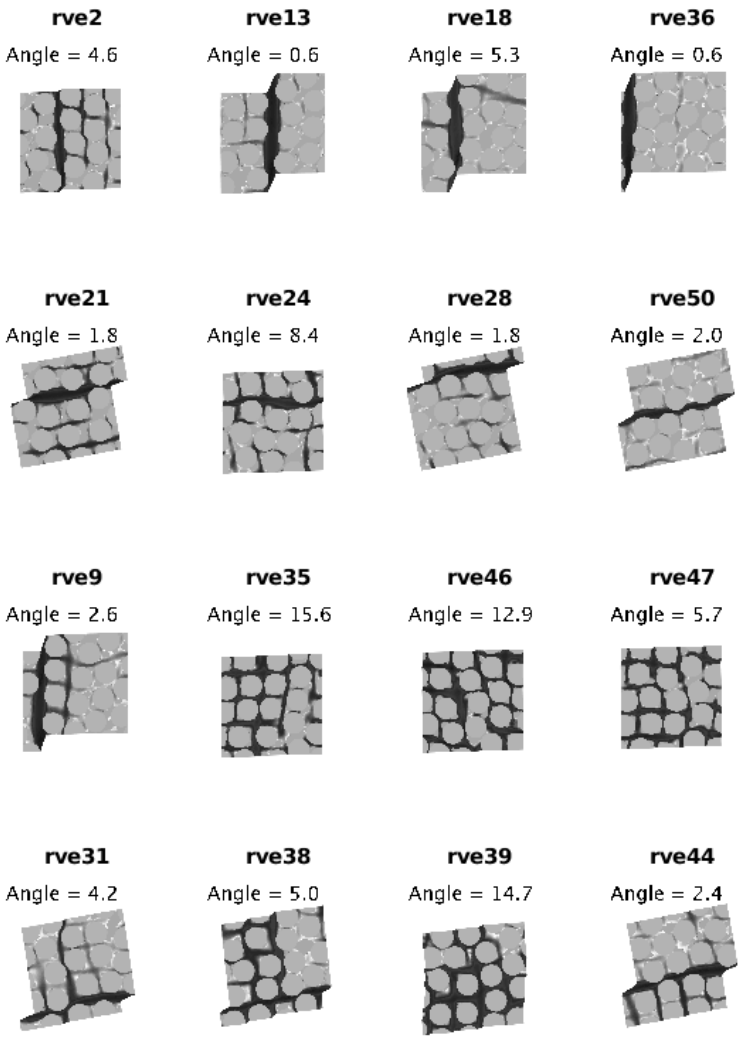

Figure E.6: Examples of localization modes at $\theta = 44^o$ ($\texttt{cf\_} = 0.160$)

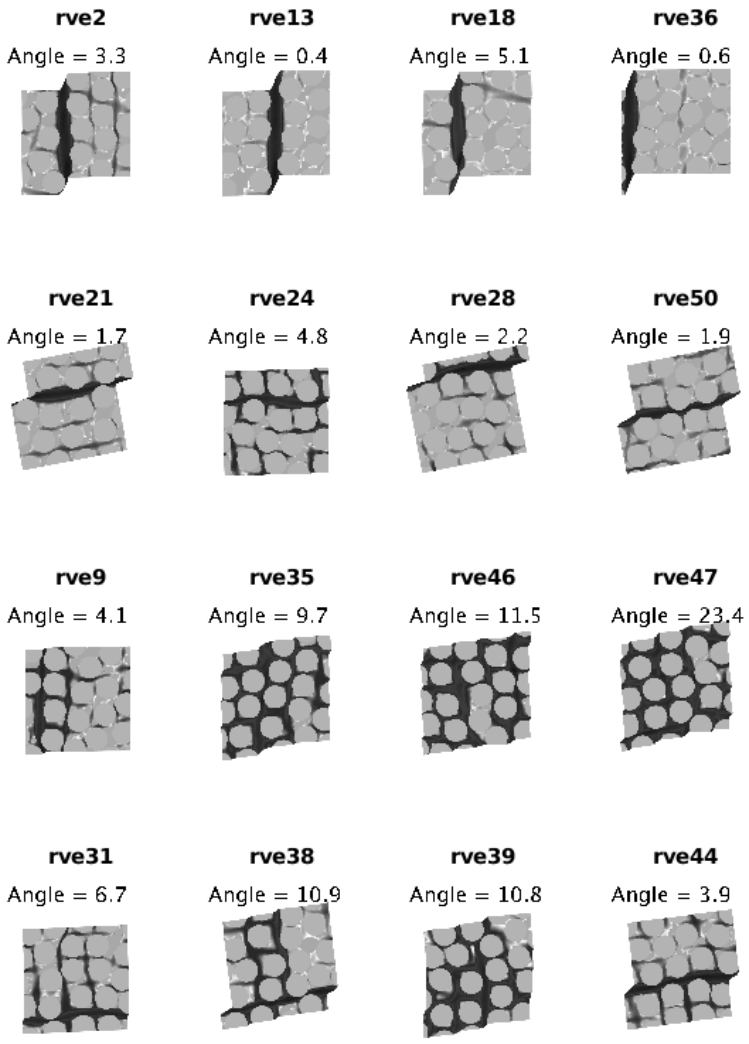

Figure E.7: Examples of localization modes at $\theta = 44^o$ (`cf_` = 0.250)

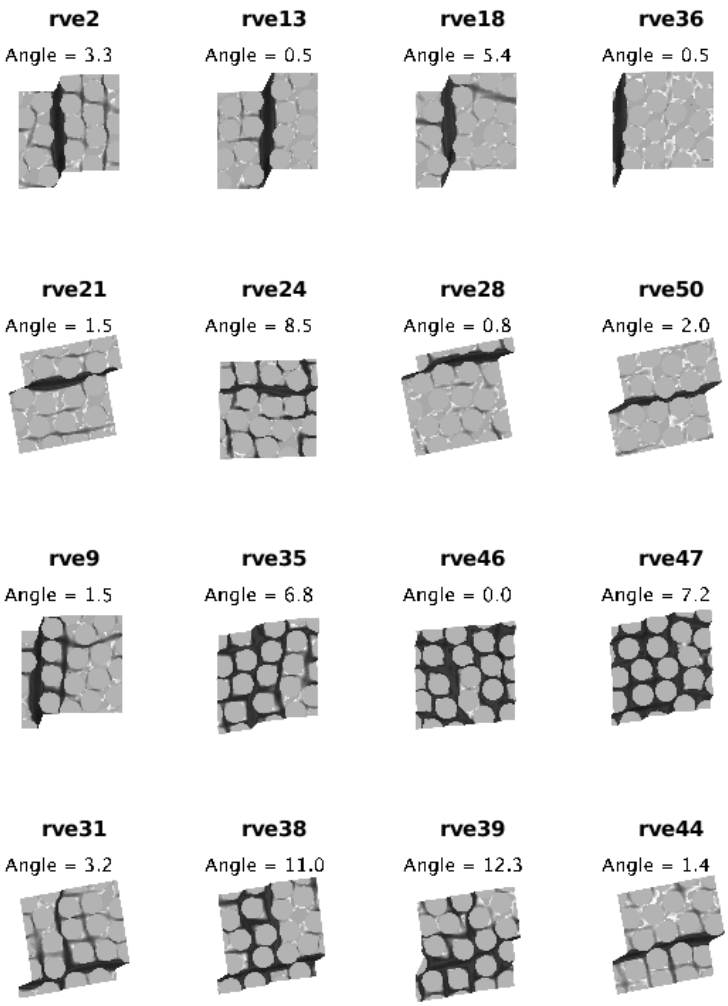

Figure E.8: Examples of localization modes at $\theta = 44^o$ ($\texttt{cf\_} = 0.400$)

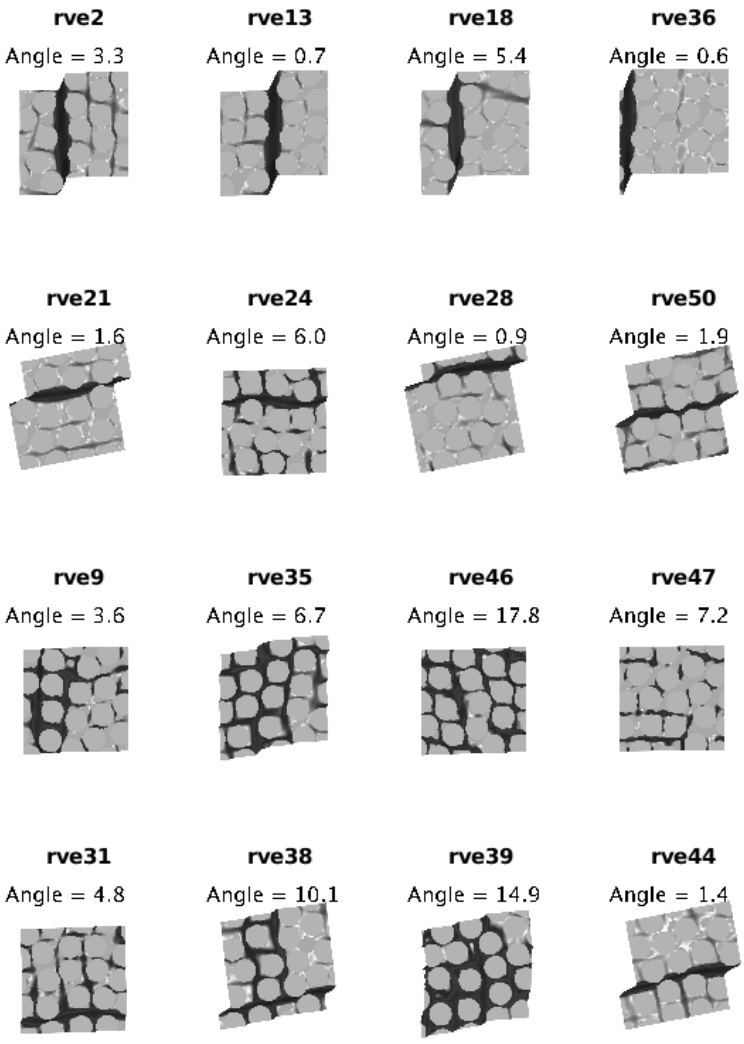

Figure E.9: Examples of localization modes at $\theta = 44^o$ (`cf_` = 0.630)

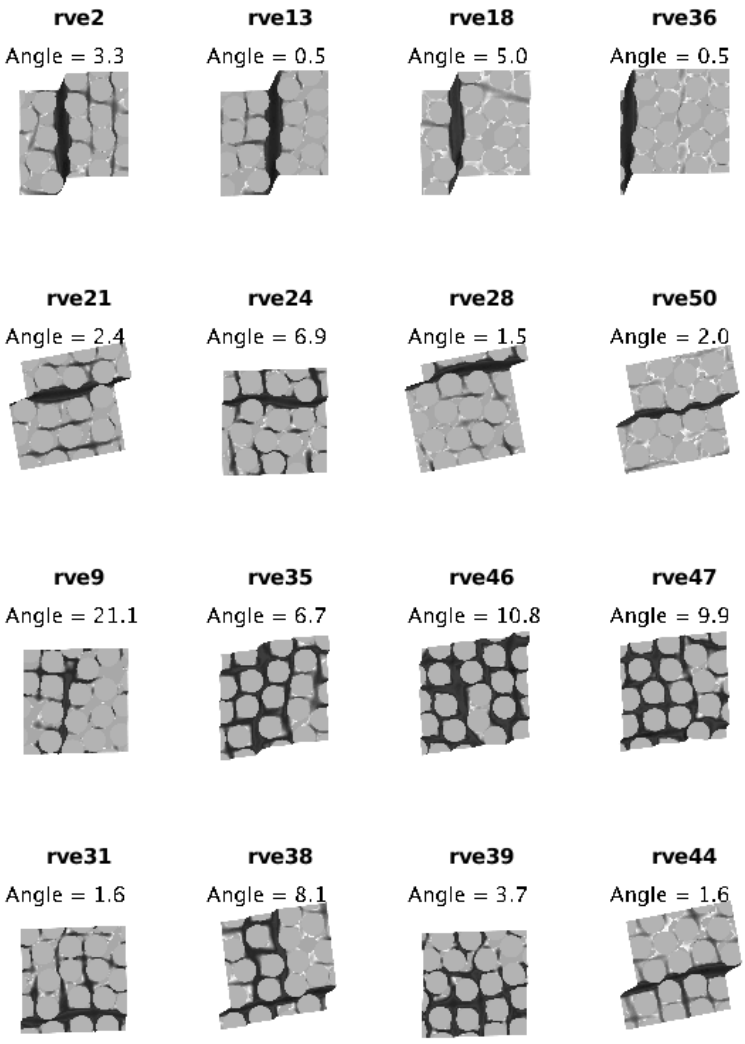

Figure E.10: Examples of localization modes at $\theta = 44^o$ ($\texttt{cf\_} = 1.000$)

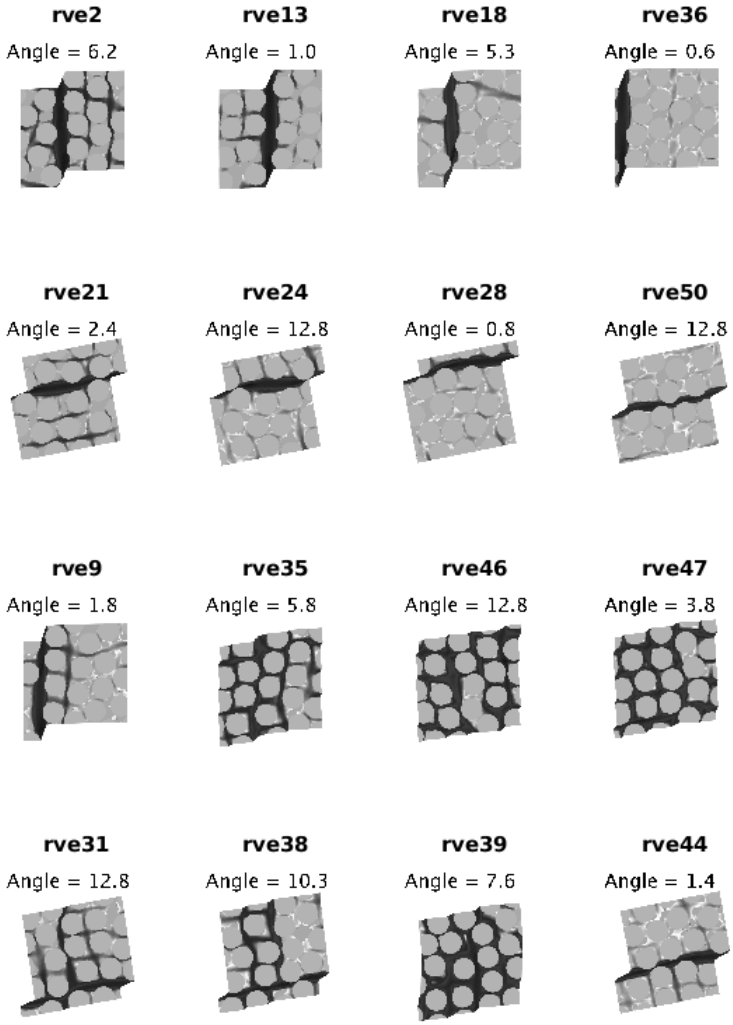

Figure E.11: Examples of localization modes at $\theta = 44^o$ (strong PBC)

Appendix F

Results: Scatter Plots

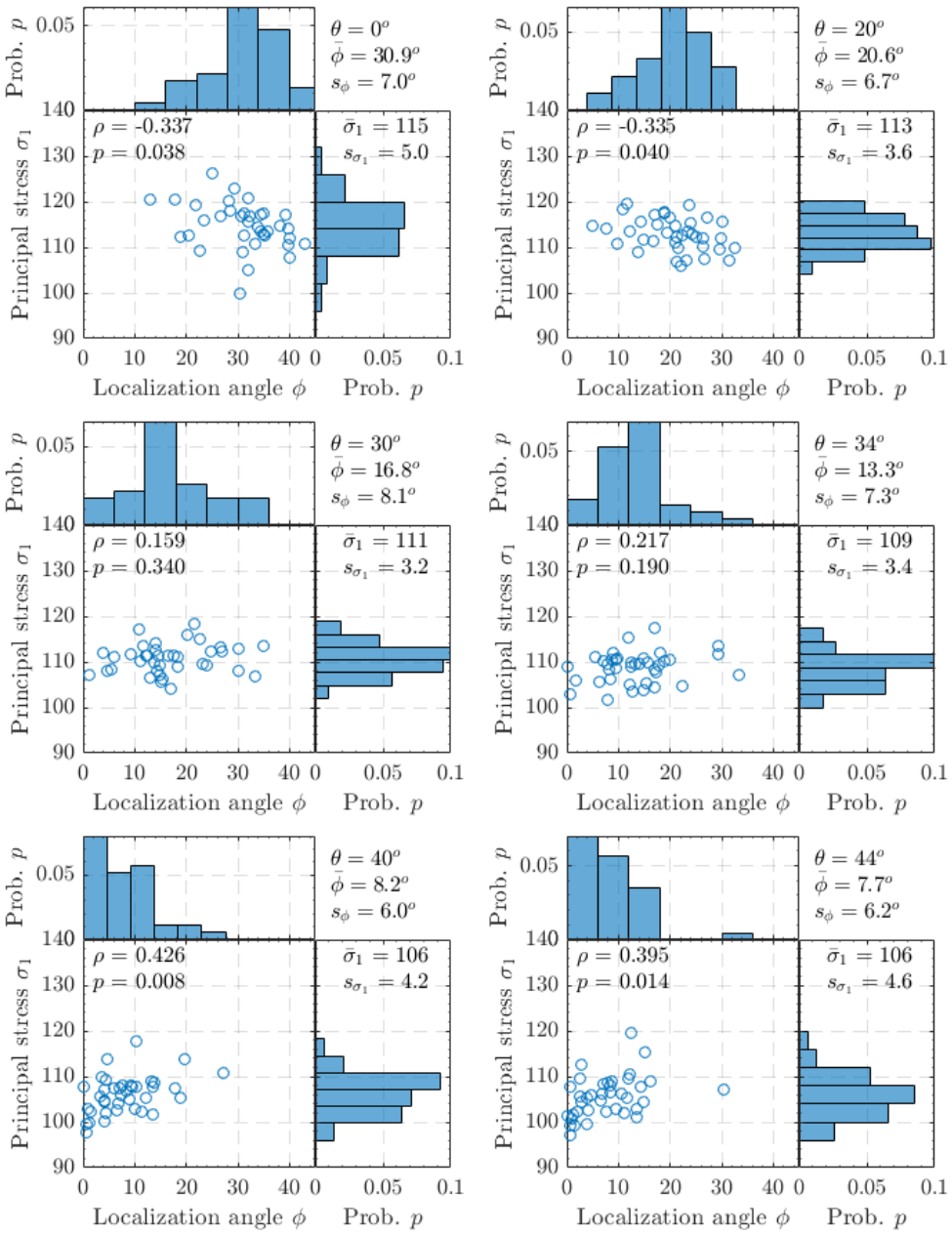

Figure F.1: Scatterplot of localization angle vs. principal stress (`cf_` = 0.016)

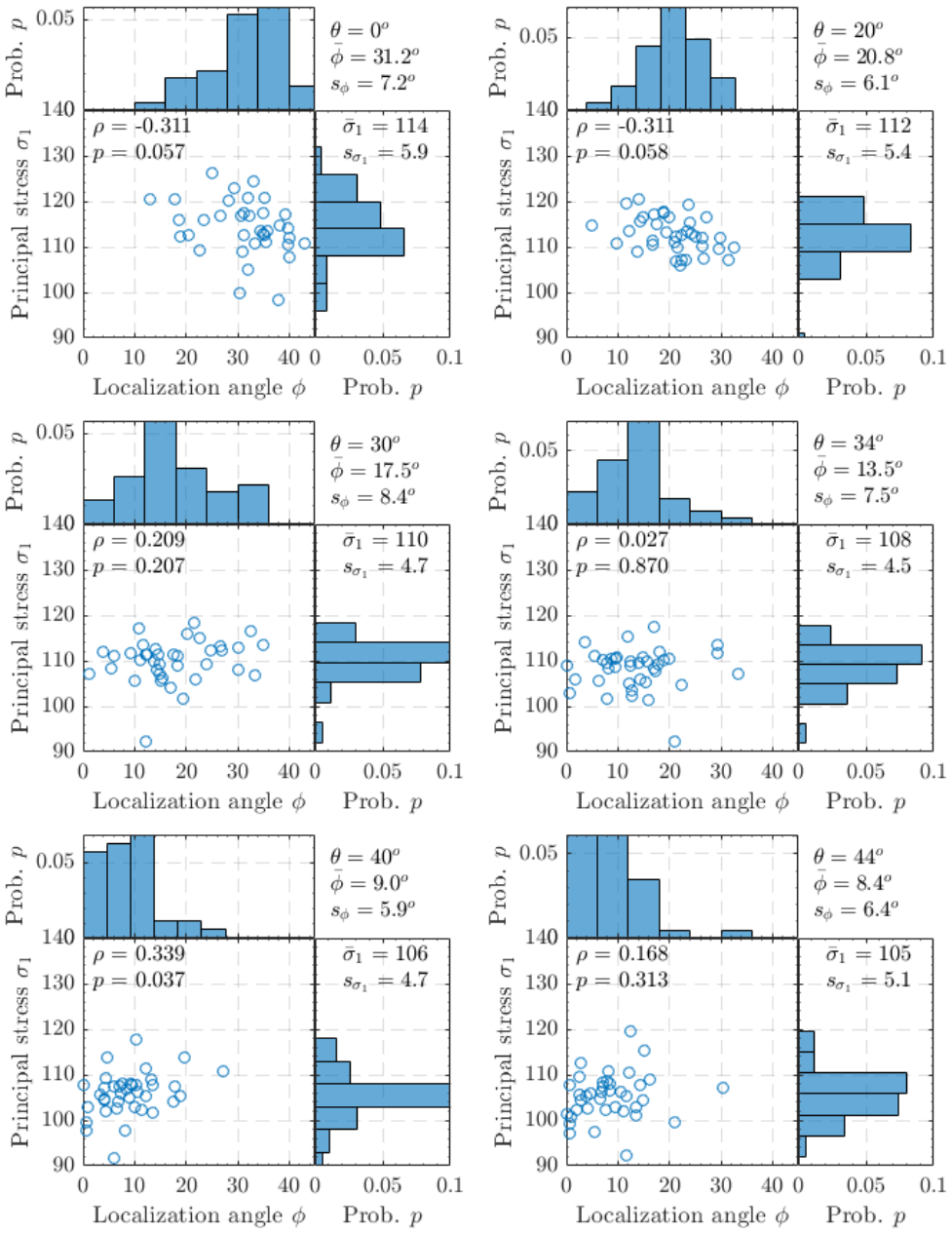

Figure F.2: Scatterplot of localization angle vs. principal stress (`cf_` = 0.025)

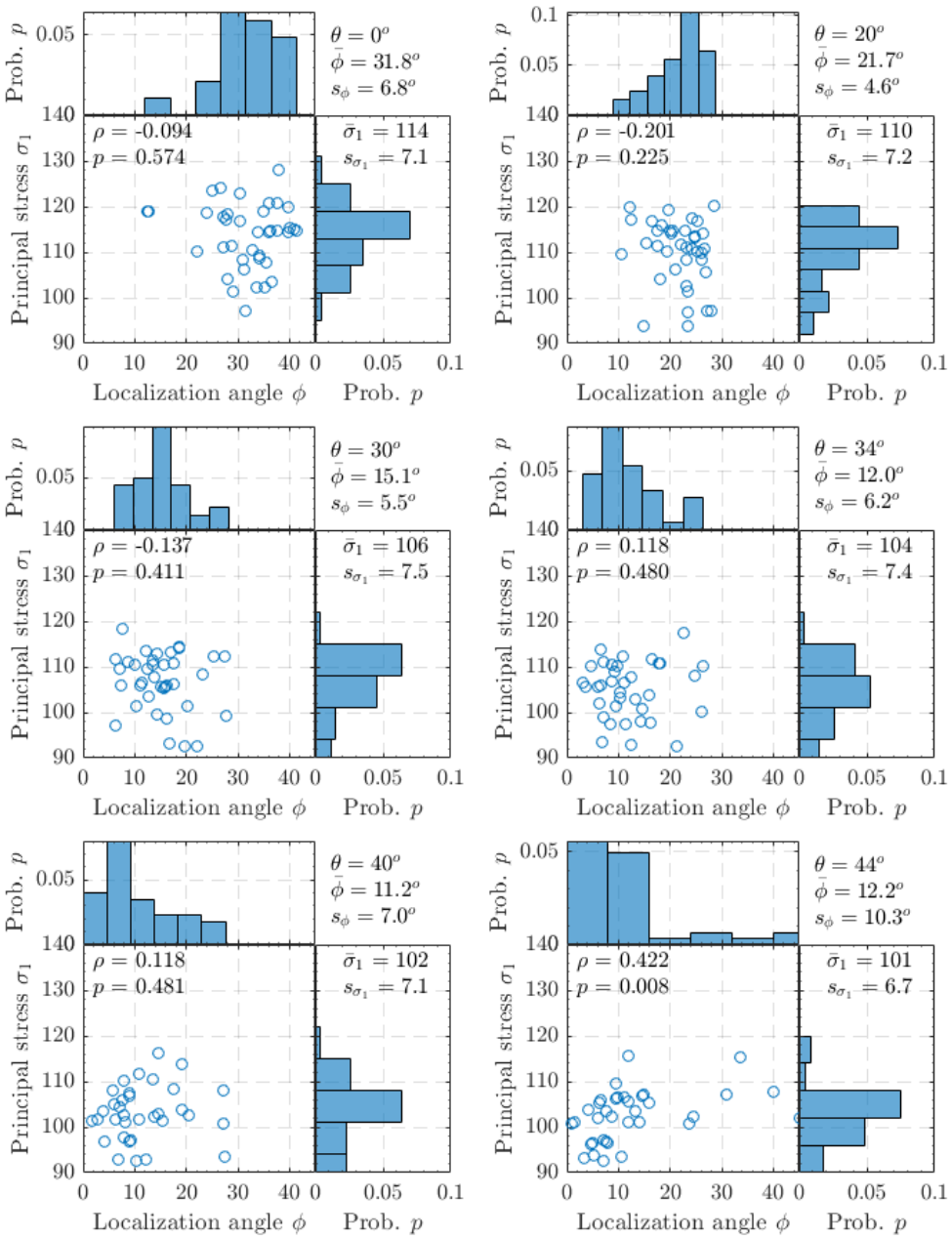

Figure F.3: Scatterplot of localization angle vs. principal stress (`cf_` = 0.040)

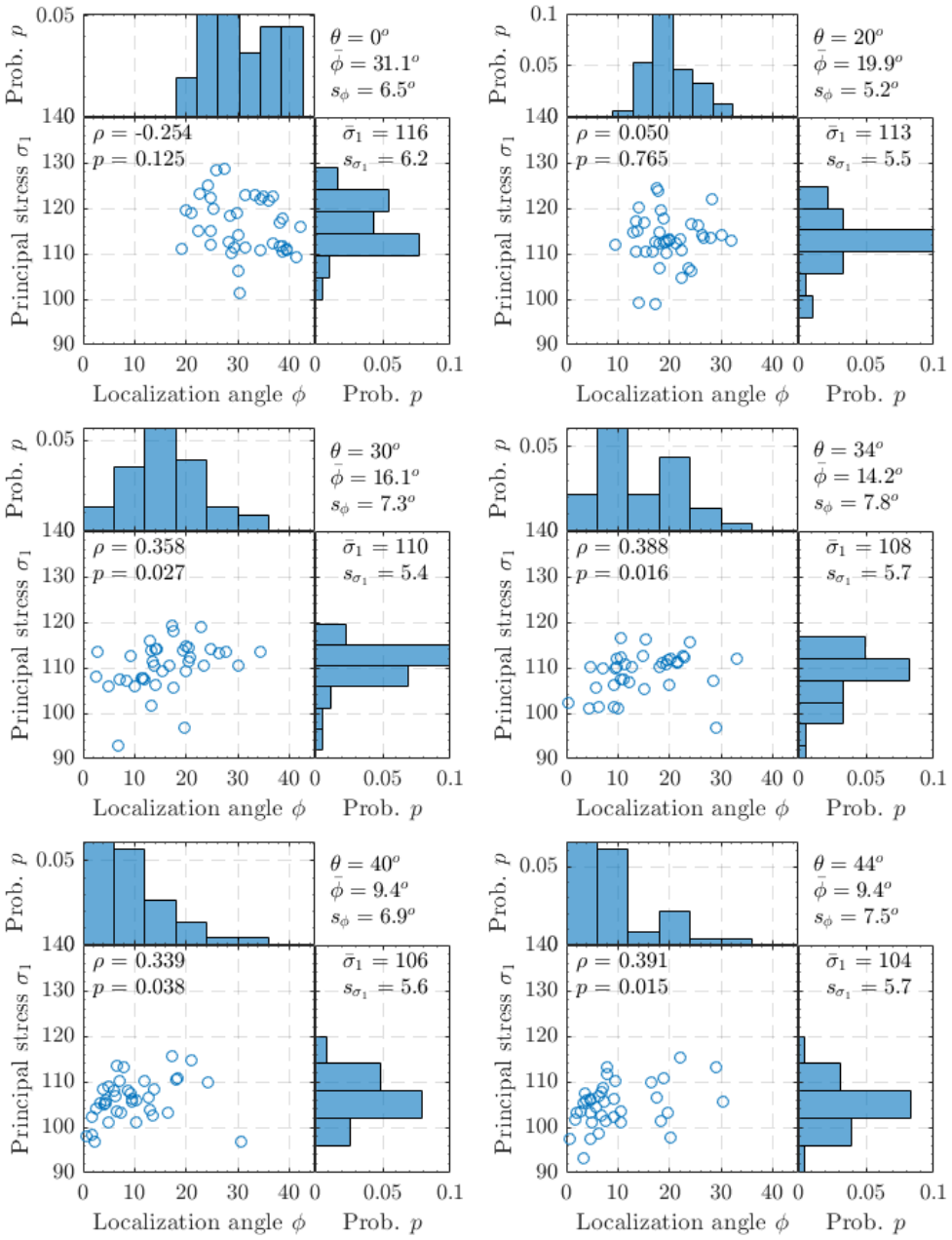

Figure F.4: Scatterplot of localization angle vs. principal stress (`cf_` = 0.063)

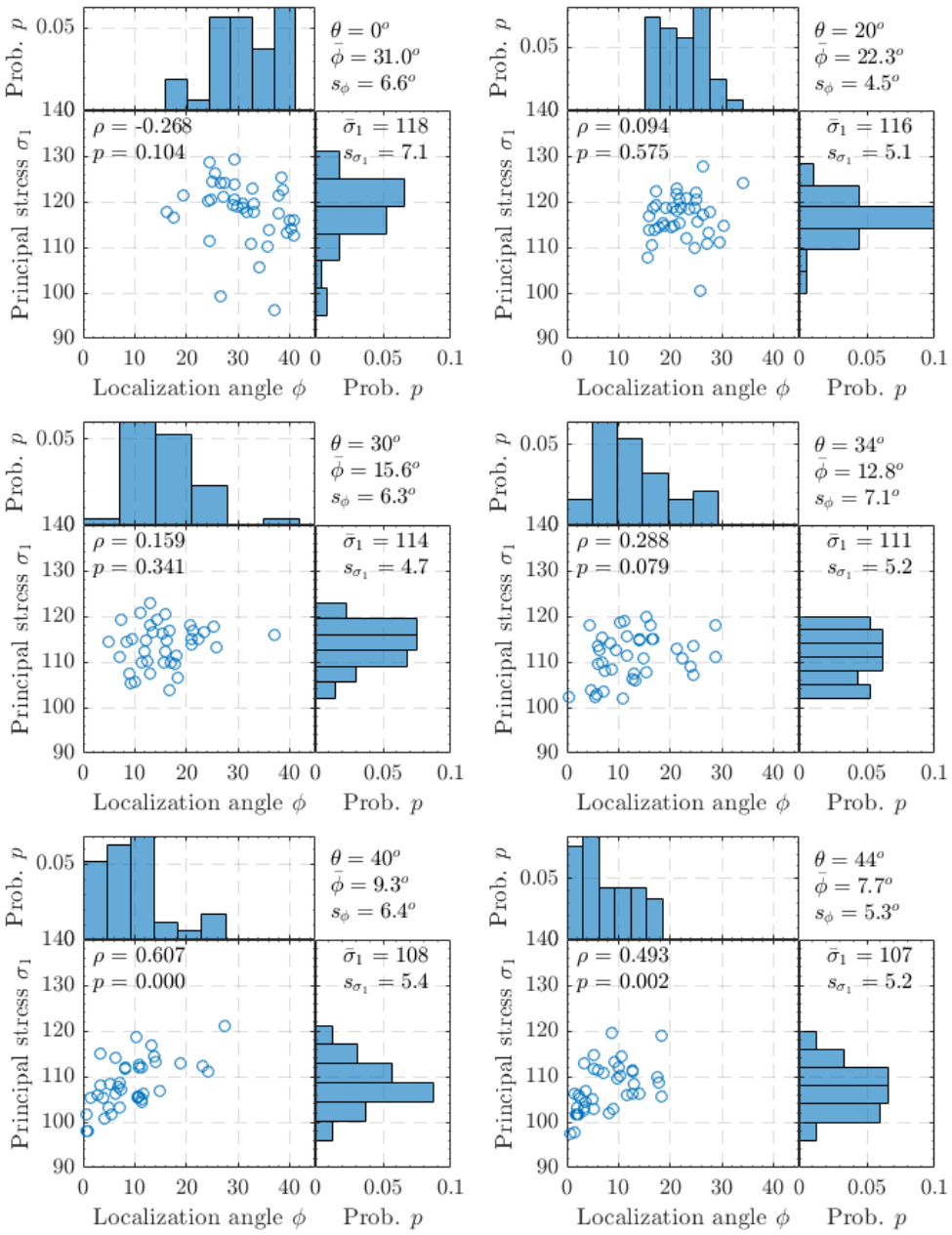

Figure F.5: Scatterplot of localization angle vs. principal stress (`cf_` = 0.100)

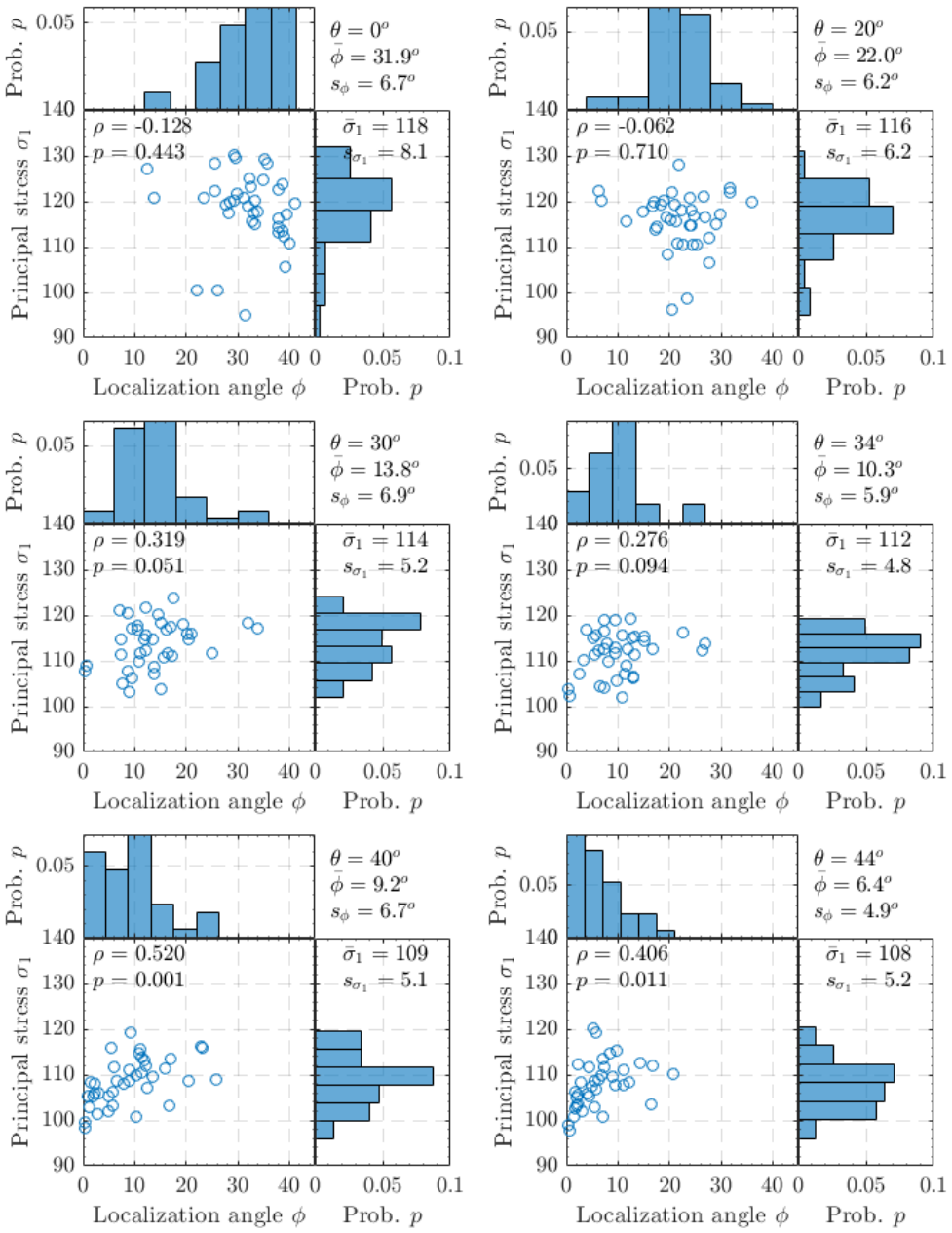

Figure F.6: Scatterplot of localization angle vs. principal stress (`cf_` = 0.160)

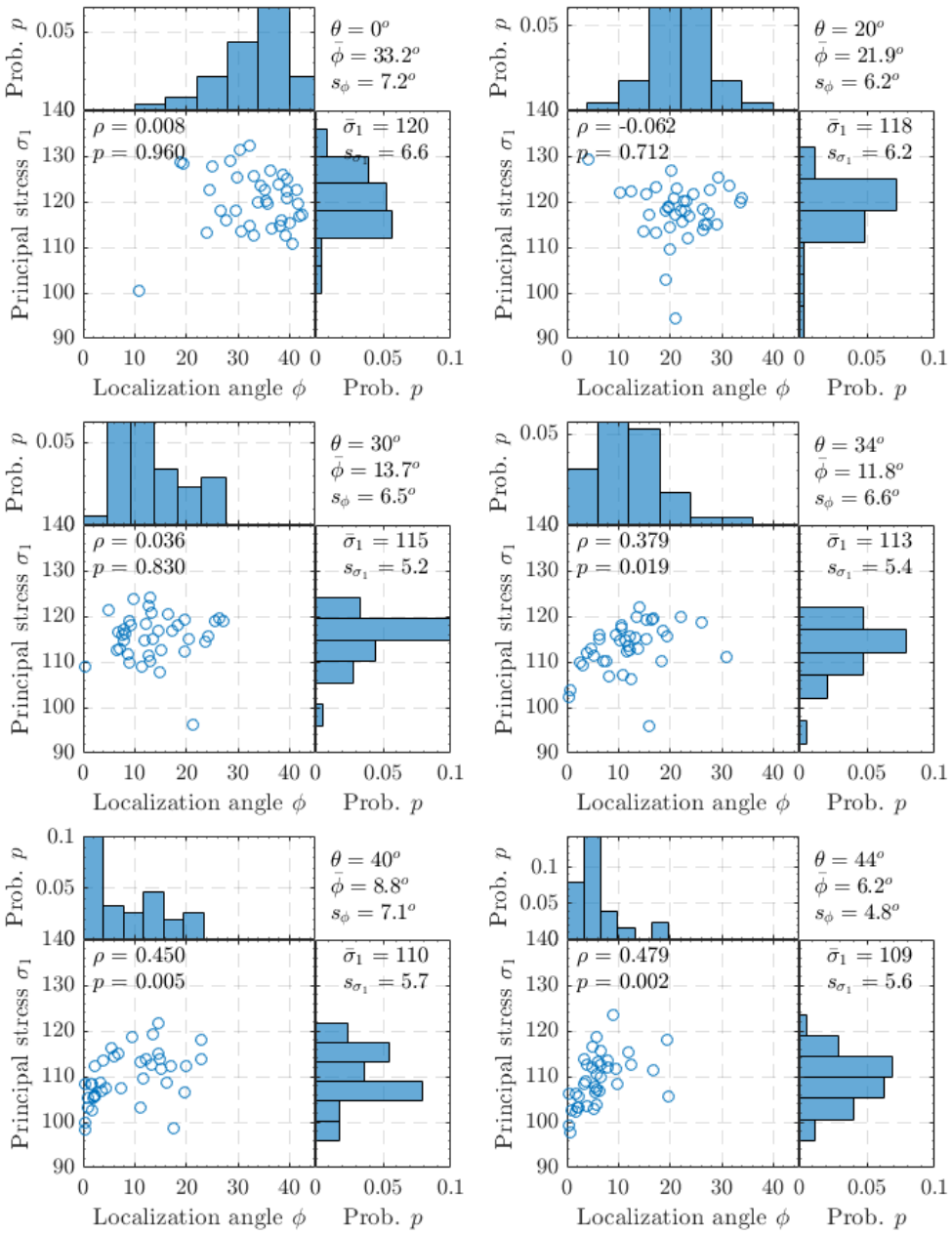

Figure F.7: Scatterplot of localization angle vs. principal stress (`cf_` = 0.250)

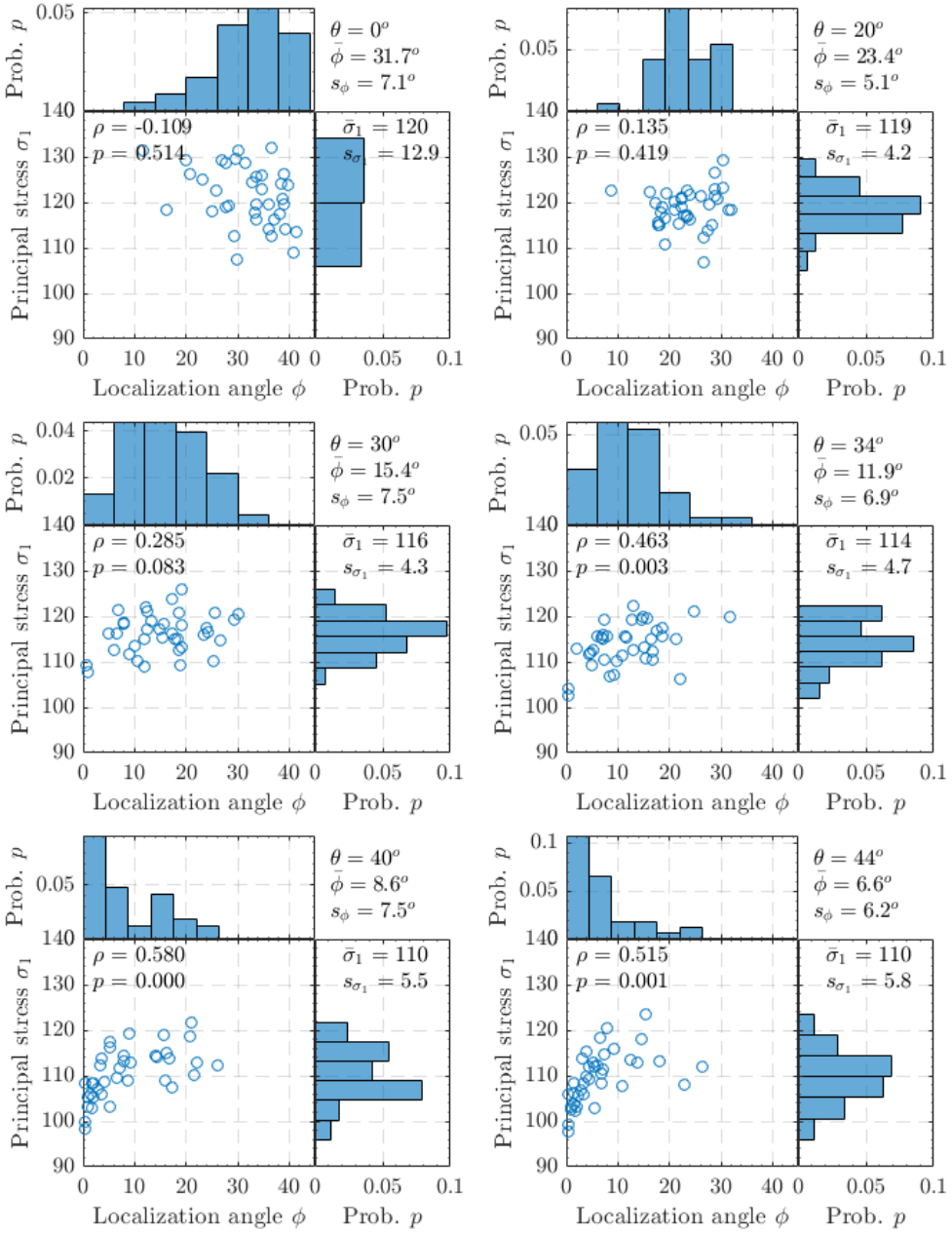

Figure F.8: Scatterplot of localization angle vs. principal stress (`cf_` = 0.400)

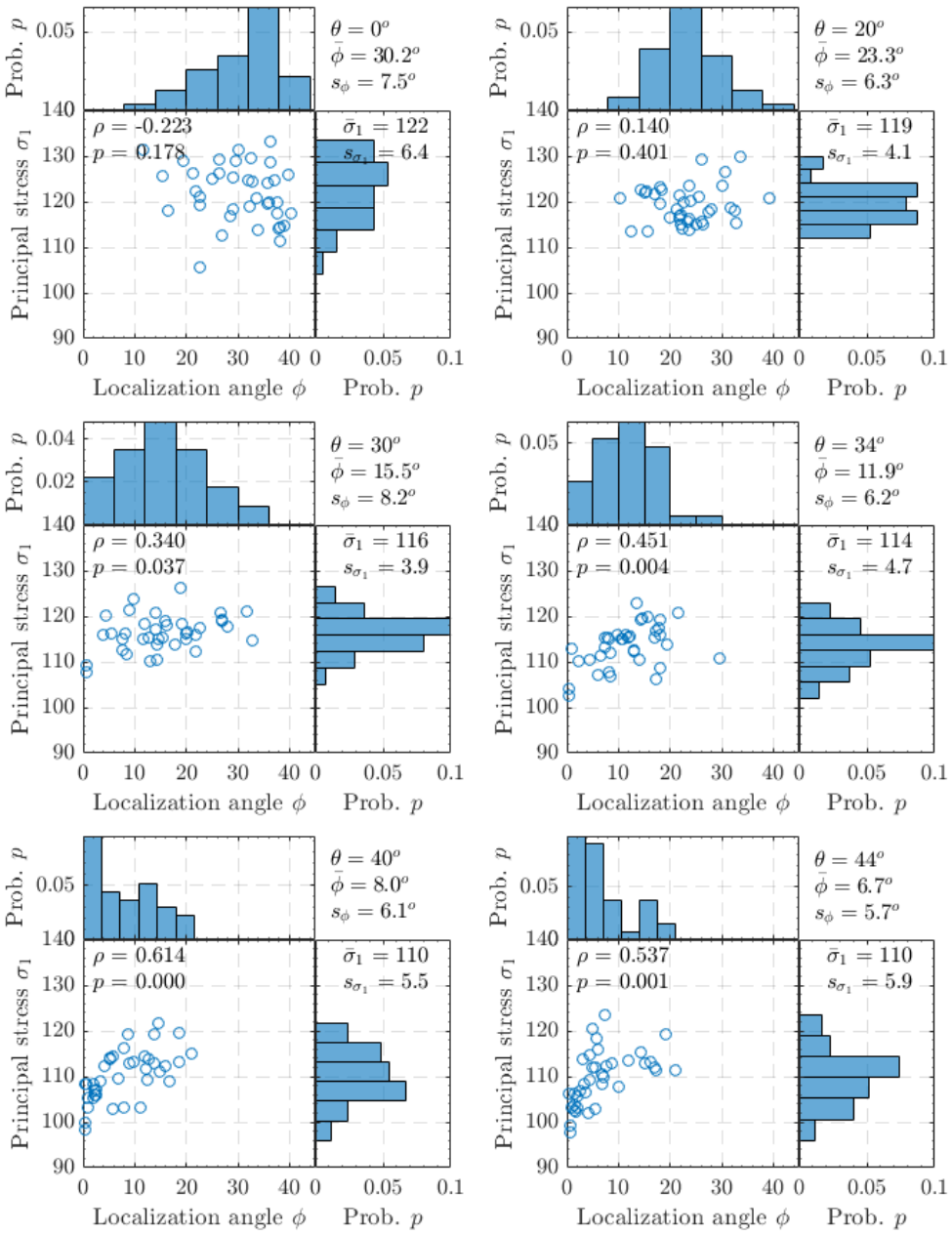

Figure F.9: Scatterplot of localization angle vs. principal stress (cf_ = 0.630)

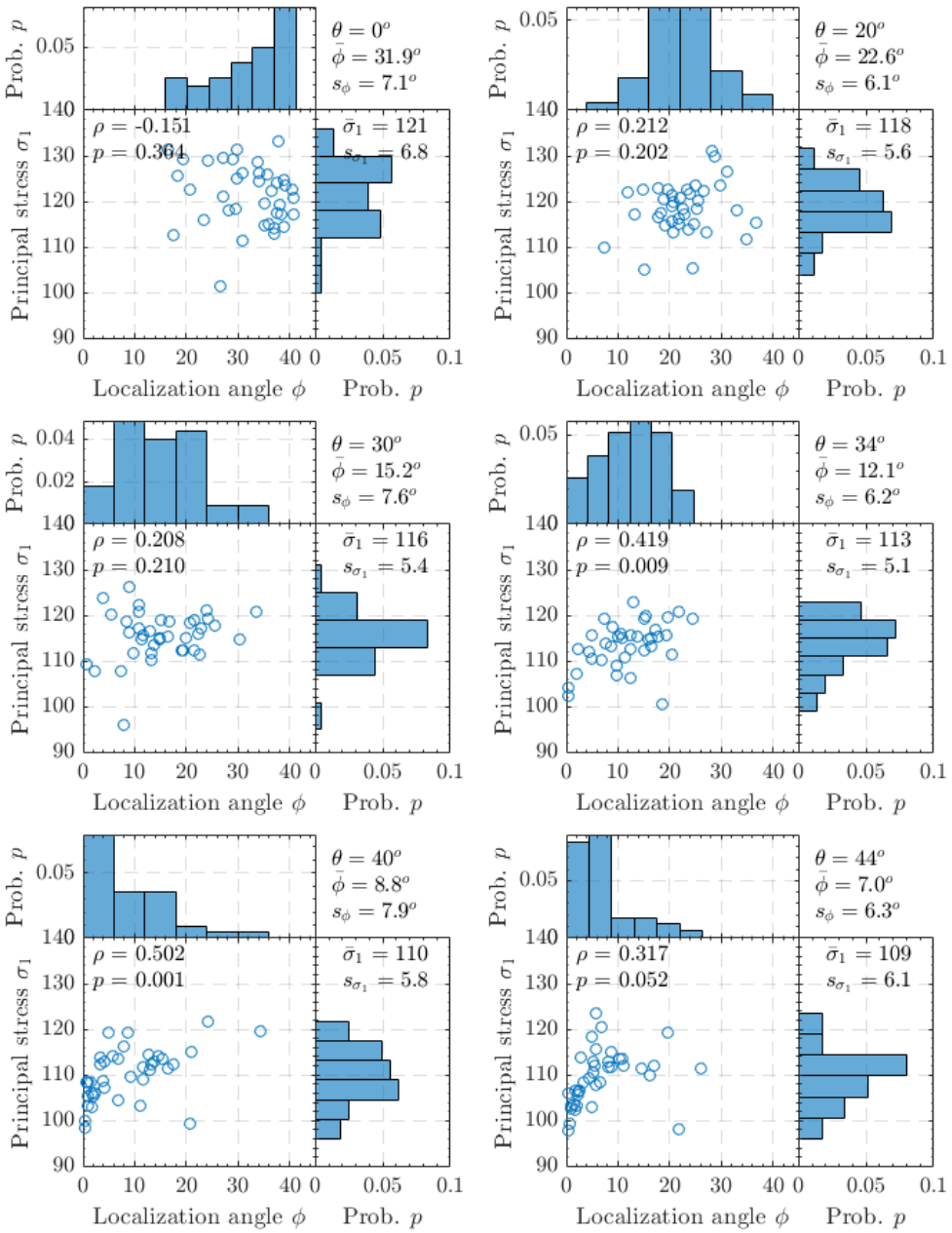

Figure F.10: Scatterplot of localization angle vs. principal stress (`cf_` = 0.1000)

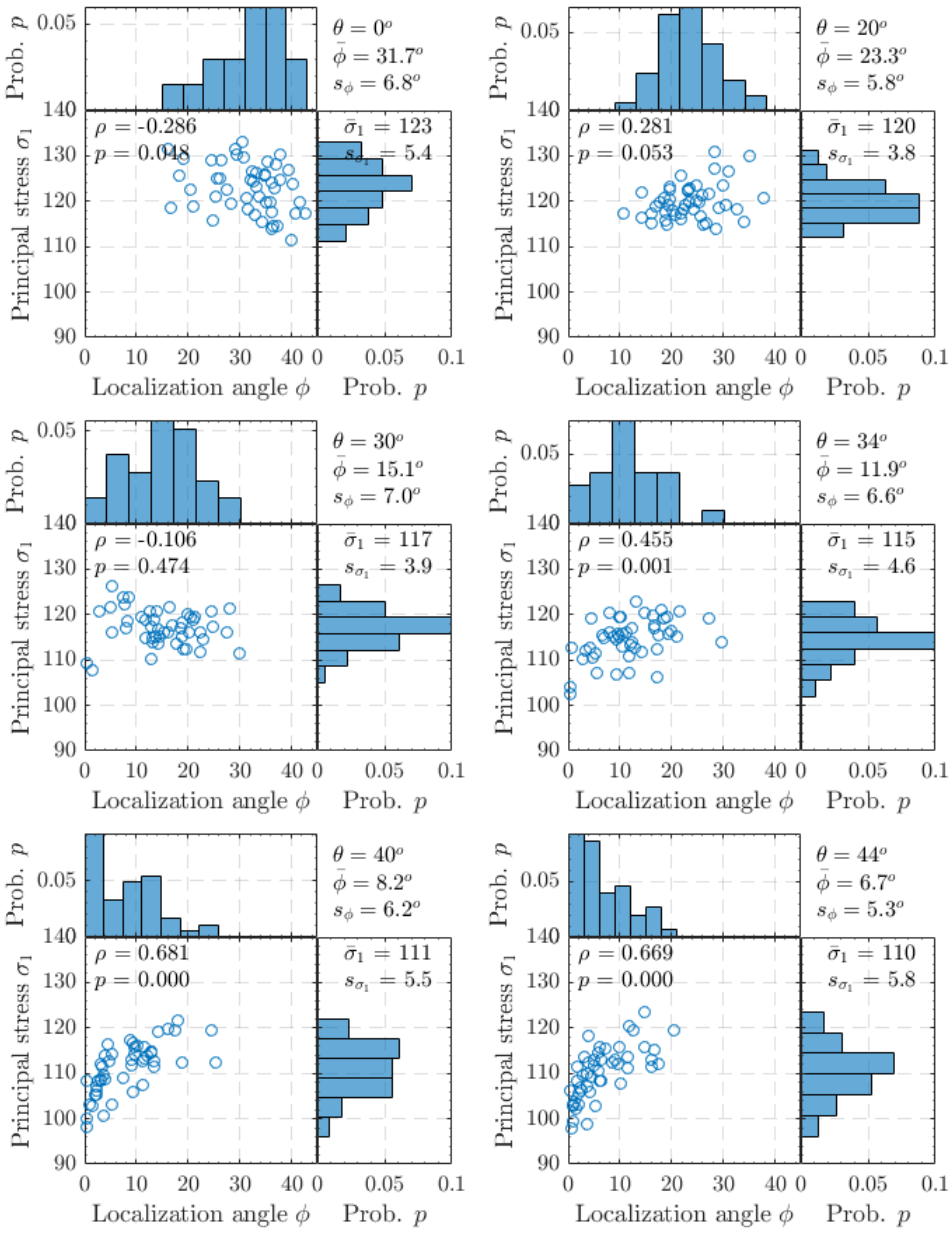

Figure F.11: Scatterplot of localization angle vs. principal stress (strong PBC)

Appendix G

Results: Transitions of Shear Bands

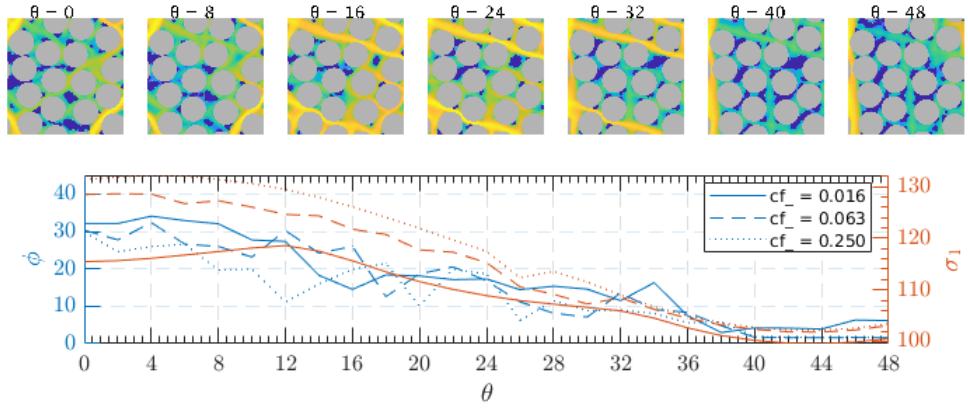

Figure G.1: Transition between shear bands (rve1)

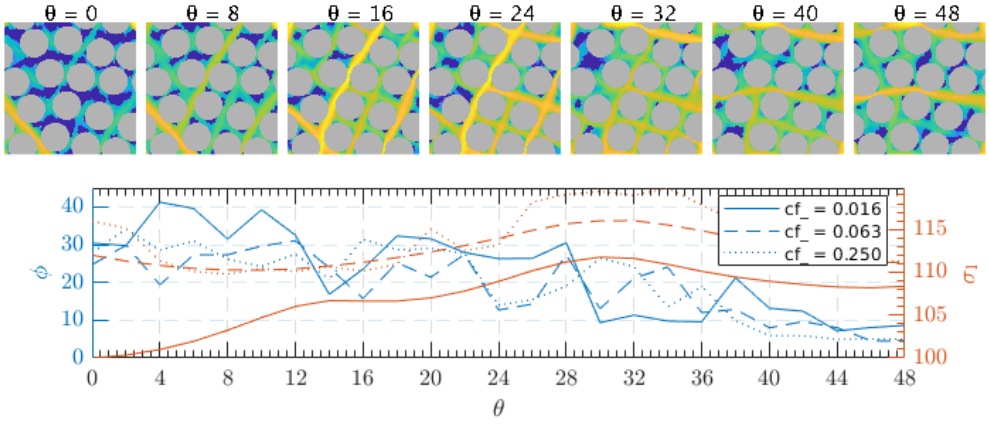

Figure G.2: Transition between shear bands (rve6)

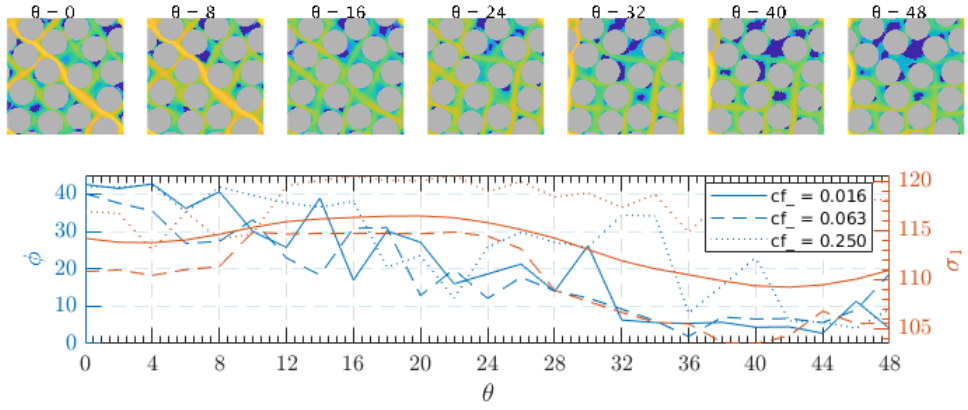

Figure G.3: Transition between shear bands (rve7)

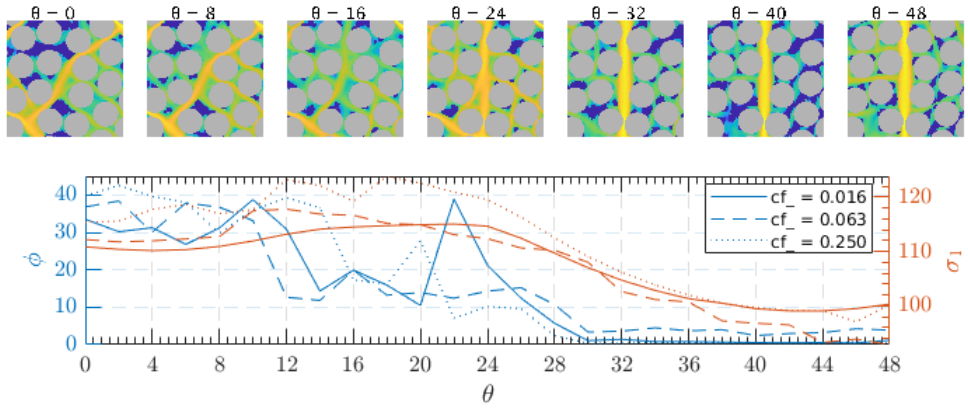

Figure G.4: Transition between shear bands (rve13)

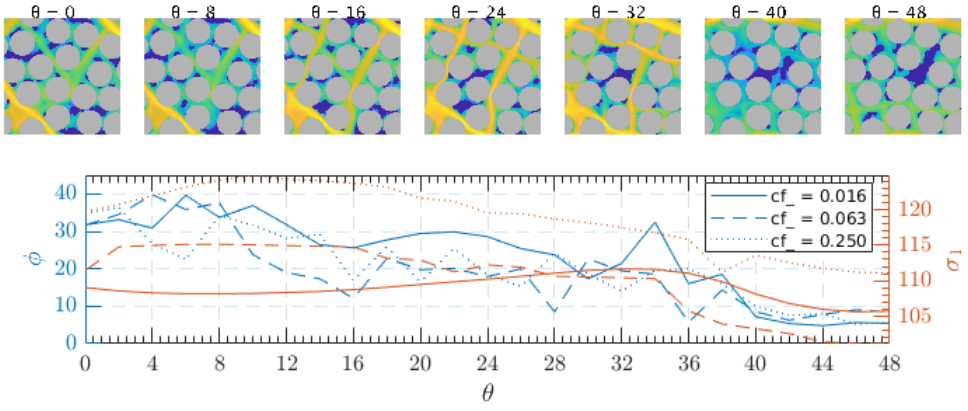

Figure G.5: Transition between shear bands (rve22)

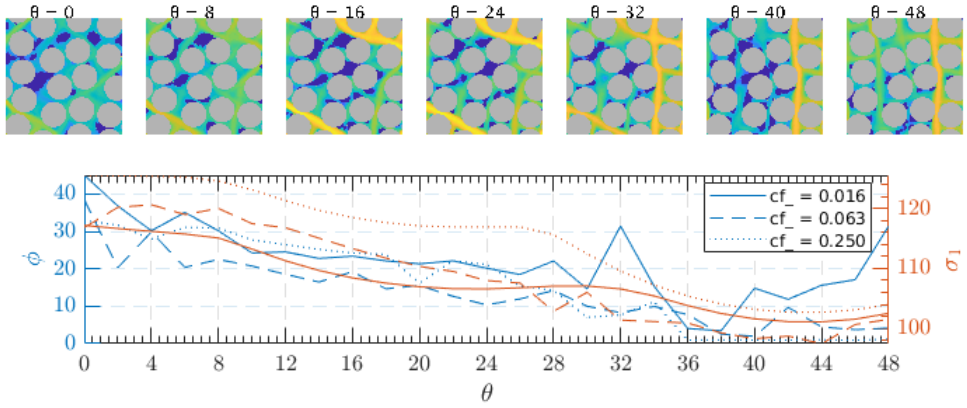

Figure G.6: Transition between shear bands (rve30)

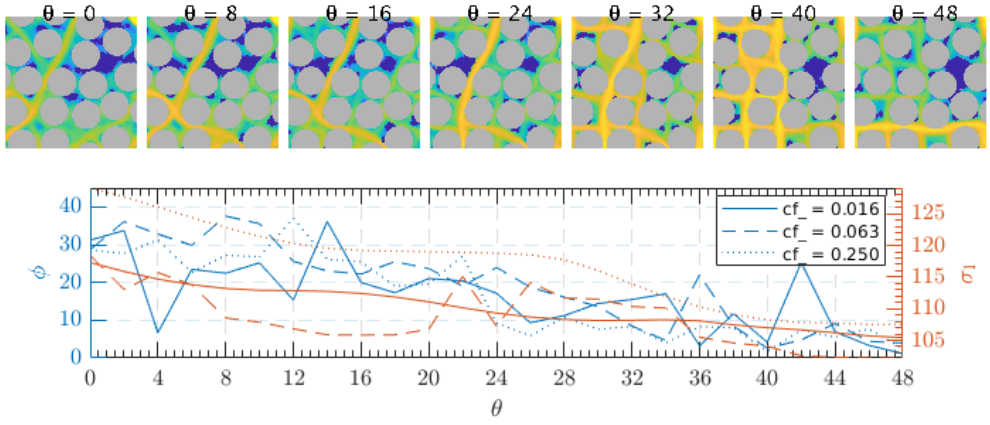

Figure G.7: Transition between shear bands (rve38)

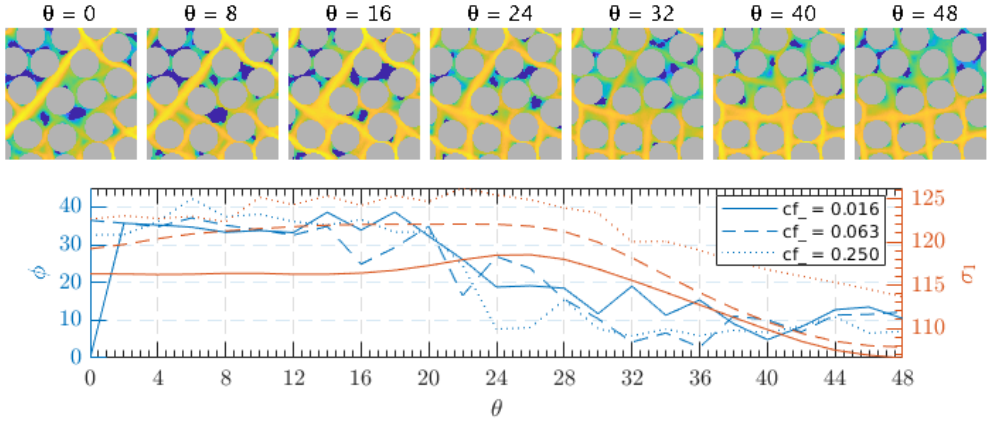

Figure G.8: Transition between shear bands (rve39)

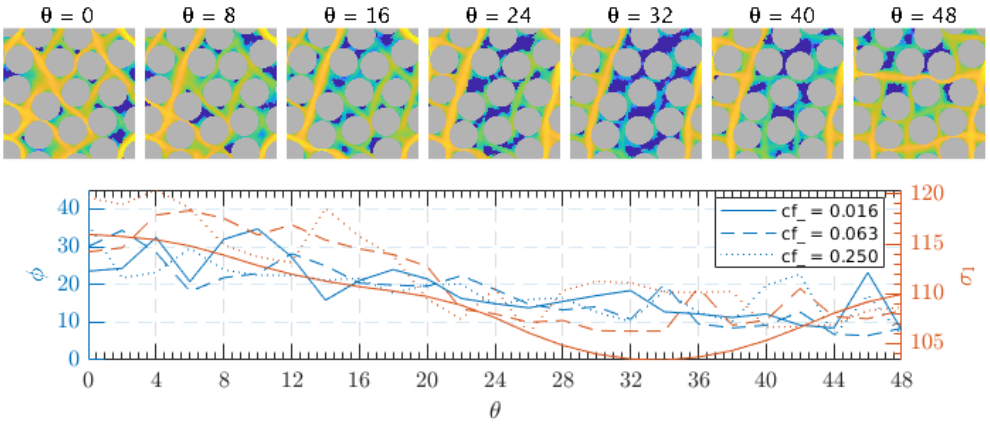

Figure G.9: Transition between shear bands (rve41)

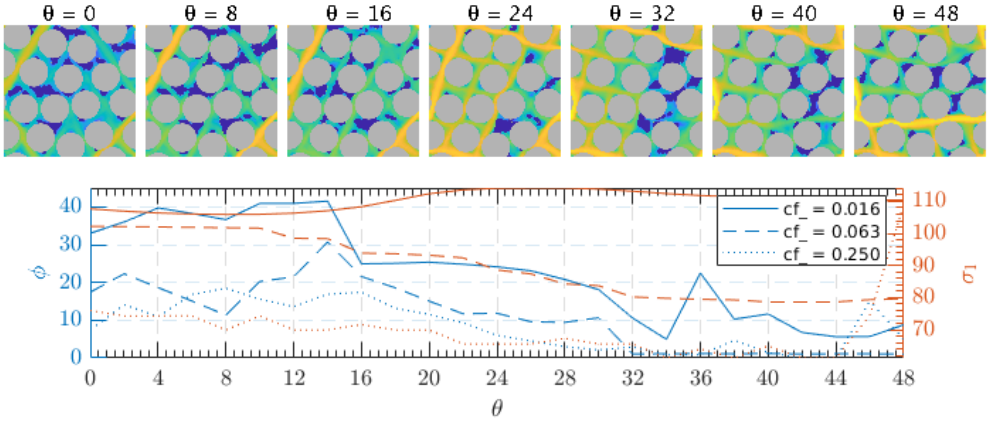

Figure G.10: Transition between shear bands (rve42)

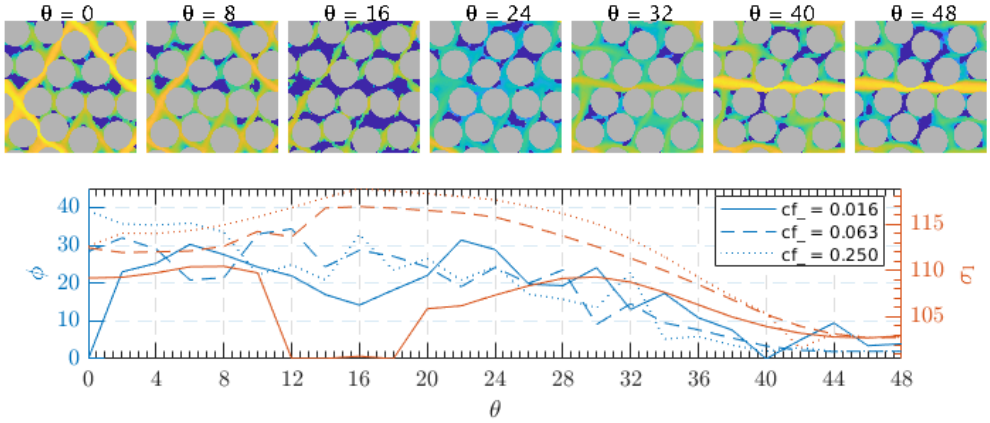

Figure G.11: Transition between shear bands (rve50)